

ABSTRACT

PADBURY, RICHARD PAUL. Bulk Property Modification of Fiber Forming Polymers using Vapor Phase Techniques. (Under the direction of Dr. Jesse S. Jur).

Atomic layer deposition provides the opportunity to introduce nanoscale inorganic coatings to organic polymers creating coatings with varied compositions of finish and distinctive interfaces. Prior research has shown that ALD materials nucleation on polymers varies in composition and structure based on how the precursor interacts with the polymer chemistry and the process conditions. To study this in more detail, in-situ quartz crystal microgravimetry is employed to understand the infiltration and saturation behavior of trimethyl aluminum in polymer thin films. Emphasis is placed on understanding reactive vapor diffusion into polymers as the exposure temperature is varied. Potential growth mechanisms based on the temperature dependent observations in this work are proposed which leads to the understanding of hybrid organic-inorganic formation in polymers.

Furthermore, polymers which have subtle variations in microstructure are explored to elucidate the nucleation behavior of inorganic coatings on polymers in more detail. Specifically, in-situ quartz crystal microgravimetry is employed to understand the nucleation behavior of alumina ALD in a series of poly-n-methacrylate and polyester thin films. The work indicates the effect that a subtle change in polymer microstructure has on the properties of the polymer film and the resultant absorption/desorption characteristics during TMA/water exposures.

The effect of % crystallinity on the infiltration mechanism is also investigated in polymer films with varied crystallinities. Finally, the effect of the hybrid modification on the mechanical behavior of fibrous materials is also explored. In particular this dissertation

highlights the process-property relationships between modified and unmodified fibers infiltrated with TMA. The results indicate that the peak load and elongation of the fibers increase with exposure to TMA. Therefore, this work has important implications on high impact applications as well as the introduction of inorganic material properties to flexible polymer systems.

© Copyright 2013 Richard Paul Padbury

All Rights Reserved

Bulk Property Modification of Fiber Forming Polymers using Vapor Phase Techniques

by
Richard Paul Padbury

A dissertation submitted to the Graduate Faculty of
North Carolina State University
in partial fulfillment of the
requirements for the degree of
Doctor of Philosophy

Fiber and Polymer Science

Raleigh, North Carolina

2014

APPROVED BY:

Dr. Jesse S. Jur
Committee Chair

Dr. Behnam Pourdeyhimi
Member

Dr. Peter Hauser
Member

Dr. Gregory Parsons
Member

Dr. Samuel Hudson
Member

DEDICATION

In loving memory of my father, John Stephen Padbury.

Ever present in your absence, your wisdom, unwavering patience and continuous support made possible my achievements of today and all that I will achieve in the future.

BIOGRAPHY

Richard was born on July 7th 1986 to Sue and John Padbury of Bloxham, Oxfordshire, UK. He obtained his Bachelor of Science in Physics in 2009 from the University of Manchester, UK. During his time at the University of Manchester, Richard also spent a year studying physics at La Universidad de Cantabria, Santander, Spain. After a short stint analyzing web pages and helping clients reach the front page of Google as an Internet Marketing Analyst, Richard moved to America in July 2010 to pursue his graduate education at NC State University. He received his Master of Science in Textile Engineering in December 2012 and began working towards his Ph.D. in Fiber and Polymer Science in August 2011. Richard has always had a fascination in other cultures and ways of living as reflected by his ambition to continue his education abroad in both Spain and the USA.

ACKNOWLEDGMENTS

I would first like to acknowledge my advisor Dr. Jesse S. Jur for his guidance, support and time invested in my personal development throughout my Ph.D. program. Dr. Jur encouraged me to continuously focus on my future goals and improve my abilities as a researcher. He recognized my strengths and gave me confidence to improve on my weaknesses, for which I am grateful. As a member of Dr. Jur's research group I will always cherish the opportunity to have worked with a diverse team of researchers and take part in numerous outreach opportunities.

I am sincerely grateful to my committee members Dr. Gregory Parsons, Dr. Behnam Pourdeyhimi, Dr. Peter Hauser and Dr. Samuel Hudson for their support throughout my project and for always helping me to overcome my greatest challenges. I would also like to extend my thanks to Dr. Stephen Michielsen for helpful discussions and for always letting me drop by for a chat, even during times that were perhaps not so convenient.

I would like to express my gratitude to the Nonwovens Institute for their financial support and the unique opportunity to work with experts from both Industry and Academia. I would like to say a special thank you to Ms. Janet O'Regan of Cotton Incorporated for her genuine interest in my research project and for always opening her door to me for helpful discussions about the project or my future aspirations.

I would like to acknowledge my research group members Dr. Jonathan Halbur, Halil Akyildiz, Murat Yokus, Nasim Farahbakhsh, Kelly Stano, Dr. Ryan Hodges, Ankesh Madan, Nathan Weiner and Kristi Barnes for their support and compassion. I am particularly grateful for your graceful attendance at numerous presentation practice sessions. I would like to

extend special thanks to Dr. Jonathan Halbur, Mr. William Sweet and Mrs. Kelly Stano for their friendship outside of graduate school.

Finally, I cannot thank my family enough for their continuous love and unwavering support through all of the good times and the hard times. Words cannot express how grateful I am. I really could not have done this without you.

TABLE OF CONTENTS

LIST OF TABLES.....	ix
LIST OF FIGURES.....	x
RESEARCH OUTLOOK.....	1
I. Overview of the literature.....	1
II. Organization of Dissertation and Key Findings.....	4
CHAPTER 1: INTRODUCTION.....	7
1.1 THE STRUCTURE OF SEMI-CRYSTALLINE POLYMERS.....	7
1.1.1 Polymer States.....	7
1.1.2 Amorphous State.....	7
1.1.3 Crystalline State.....	13
1.2 FORMATION AND PROPERTIES OF FIBROUS POLYMERS.....	15
1.2.1 Fiber formation.....	15
1.2.2 Melt Spinning.....	16
1.2.3 Nonwovens	18
1.2.4 Fiber Properties	20
1.2.5 Mechanical Properties	21
1.2.6Transport Properties	25
1.3 VAPOR PHASE MODIFICATION OF POLYMERS.....	32
1.3.1 Hybrid Organic-Inorganic Materials.....	32
1.3.2 Characteristics of ALD	35
1.3.3 ALD on Polymers.....	37
1.3.4 Comparative ALD processes	40
1.3.5 Potential Applications	42

1.3.6 Roll-to-Roll Processes.....	44
Chapter 1 Figures.....	47
Chapter 1 References.....	65
CHAPTER 2: THE EFFECT OF POLYMER MICROSTRUCTURE ON THE NUCLEATION BEHAVIOR OF ALUMINA VIA ATOMIC LAYER DEPOSITION.....	75
2.1 Introduction.....	75
2.2 Experimental.....	77
2.3 Results.....	80
2.4 Discussion.....	85
2.5 Conclusion.....	90
Chapter 2 Figures.....	92
Chapter 2 References.....	101
CHAPTER 3: TEMPERATURE DEPENDANT INFILTRATION OF POLYMERS DURING SEQUENTIAL EXPOSURES TO TRIMETHYL ALUMINUM.....	104
3.1 Introduction.....	104
3.2 Experimental Procedure.....	106
3.3 Results.....	109
3.4 Discussion.....	117
3.5 Conclusion.....	129
Chapter 3 Figures.....	131
Chapter 3 References.....	142

CHAPTER 4: AN IN-SITU COMPARISON OF PRECURSOR INFILTRATION INTO POLYMER THIN FILMS VIA ATOMIC LAYER DEPOSITION AND SEQUENTIAL VAPOR INFILTRATION.....	148
4.1 Introduction.....	148
4.2 Materials and Methods.....	150
4.3 Results and Discussion.....	152
4.4 Conclusion.....	160
Chapter 4 Figures.....	162
Chapter 5 References.....	168
CHAPTER 5: MECHANICAL MODIFICATION OF FIBER FORMING POLYMERS BY HYBRID ORGANIC-INORGANIC BUFFERS CREATED IN THE VAPOR PHASE.....	171
5.1 Introduction.....	171
5.2 Materials and Methods.....	172
5.3 Results and Discussion.....	177
5.4 Conclusion.....	186
Chapter 5 Figures.....	188
Chapter 5 References.....	197
FUTURE PROSPECTS.....	200

LIST OF TABLES

Table 1.1. WLF equation constants and glass transition temperatures of a range of polymers.

Table 2.1. Summary of absorption/desorption characteristics of TMA exposed to the polymers analyzed in this work

Table 3.1. Thermal properties of polymers examined in this work including⁴¹: glass transition temperature (T_g); melting temperature (T_m) and coefficient of thermal expansion (α). The repeat unit structure of each polymer is also provided to highlight variations in functional groups. T_m values were used to determine exposure temperature ranges for each polymer.

Table 5.1. Summary of PET specimens used in this study. Each film was heat treated under different conditions to vary % crystallinity.

Table 5.2. Fiber specimens used for investigations of the mechanical properties of SVI modified PET fibers with different crystallinities.

LIST OF FIGURES

Figure 1.1. Schematic diagram indicating volume changes that occur in polymers as temperature increases. The region labeled α represents the polymer free volume below the glass transition temperature while β corresponds to the polymer free volume at T_g .

Figure 1.2. Diagrammatic representation of the temperature dependence of the expansion coefficient

Figure 1.3. Conformation entropy as a function of temperature as stated by the Gibbs and DiMarzio thermodynamic theory of T_g .

Figure 1.4. Effect of storage temperatures above and below the glass transition temperature on the volume of a polymer. As the diagram indicates, at higher storage temperatures polymer chains are able to relax quicker which corresponds to volume shrinkage.

Figure 1.5. Diagrammatic representation of the melt spinning process adapted from Billmeyer.

Figure 1.6. Diagrams demonstrating the wet lay and dry lay processes. Figures obtained from edana.

Figure 1.7. Diagram representing the meltblown and spunbond (spunlaid) processes. Figure obtained from edana.

Figure 1.8. Diagrammatic representation of a typical stress-strain curve of a textile fiber highlighting the elastic, plastic and permanent deformation regions. Below the stress-strain curve, a series of diagrams indicates the effect that an applied load has on the structure of the polymer which corresponds to the stress-strain behaviour observed in the curve.

Figure 1.9. Stress-strain curve indicating the characteristic behaviour of textile fibers during a tensile test.

Figure 1.10. Fractional mass gain as a function of time and membrane thickness.

Figure 1.11. Analysis of publications based on hybrid organic-inorganic materials. The data was obtained from a literature search using the Web of Science search tool.

Figure 1.12. Diagram demonstrating the dosing sequence of an organometallic precursor and co-reactant of a typical ALD process

Figure 1.13. Diagrammatic representation of the ALD window indicating growth rate as a function of temperature.

Figure 1.14. TEM images of various vapor deposition compositions. a) indicates a conformal coating formed on cellulose, b) indicates a hybrid organic in-organic layer formed on PA-6 with a graded sub-surface composition, c) shows the island growth and nucleation associated with vapour deposition on PP fibers and finally d) shows a hybrid organic-inorganic layer formed on PA-6 via SVI with an ungraded finish

Figure 1.15. Diagram demonstrating the dosing sequence of an organometallic precursor and co-reactant of a typical SVI process.

Figure 1.16. Diagram describing the photocatalytic principle within the active filtration of a toxic gas

Figure 1.17. Lotusat roll-to-roll ALD process.

Figure 2.1. Growth per cycle (GPC) of alumina as a function of temperature formed by analyzing alumina growth on Si wafers using an alumina ALD cycle sequence of TMA/N₂/H₂O/N₂= 0.2/30/0.2/45 seconds. Si wafers were exposed to the sequence for 100 cycles at the various reactor temperatures. Ellipsometry measurements were used to determine the thickness of alumina coatings on Si wafers which was converted to an average growth per cycle.

Figure 2.2. (a) QCM Analysis of an Alumina ALD process at 60°C and 1 Torr on a quartz crystal pre-deposited with 100 cycles of alumina. The mass deposition rate is indicated in (b) which corresponds to the mass uptake per cycle.

Figure 2.3. QCM Analysis of an Alumina ALD process at 60°C and 1 Torr on PBT and PPMA polymer thin films. The alumina ALD process from Figure 2 (a) is provided for comparison to demonstrate the unique nucleation behavior of ALD on polymers.

Figure 2.4. QCM analysis of a single 0.2 second TMA dose in PBT and PET films at 60°C. The analysis emphasizes the unique absorption/desorption characteristics of TMA in these polymer films.

Figure 2.5. (a) QCM analysis of a single 0.2 second TMA dose in a series of poly-n-methacrylate polymer films at 60°C. The analysis emphasizes the unique absorption/desorption characteristics of TMA in these polymer films. The absorption of TMA is less than the absorption of TMA in polyesters. Therefore, (b) indicates the absorption/desorption of TMA at 60°C with a longer TMA dose of 10 secs.

Figure 2.6. Effect of temperature on the specific volume of polymers adapted from ref (27). The diagram shows that the specific volume of polymers can be split up into the volume occupied by constituent atoms and the space between polymer chains called the free volume. The glass transition temperature indicates the point at which the polymer transitions from a glassy brittle material with a low free volume, to a rubbery flexible material with a high free volume.

Figure 2.7. Diagram describing the variation in absorption characteristics of polymers that contain side chain pendant groups. The presence of pendant groups reduces available free volume for vapor infiltration as a result of the tortuous network of interconnected pores in comparison to polymers lacking pendant groups such as polyesters.

Figure 2.8. QCM Analysis of an Alumina ALD process at 60°C and 1 Torr on PPMA polymer thin films with varying TMA purge times. The analysis indicates a slower nucleation period and reduced mass gain of alumina as purge time increases.

Figure 3.1. (a) *In-situ* QCM analysis of ten consecutive TMA multi-doses onto PA-6, PET, PMMA and PAA polymer films at 60 °C. A TMA multidosing scheme was created by programming the reactor to a typical ALD cycle sequence with an eliminated water dose. The TMA multidose cycle sequence in this work follows TMA/N₂/H₂O/N₂ = 0.2/60/0/60 seconds. The polymer films were thermally equilibrated to the reactor temperature until the change in frequency recorded by the QCM was approx ±0.2Hz over a period of 60 sec. Prior to the first TMA exposure at t=0, the reaction chamber was purged with N₂ for 240 sec. For clarification, **(b)** indicates absorbed TMA and reacted TMA retained within a polymer film during 2 doses of TMA following a multidosing scheme.

Figure 3.2. *In-situ* QCM analysis of ten consecutive TMA multi-doses onto PA-6 indicating the saturation behavior of PA-6 between 30°C and 150°C.

Figure 3.3. *In-situ* QCM analysis of ten consecutive TMA multi-doses onto PAA indicating the saturation behavior of the polymer film between 30°C and 150°C.

Figure 3.4. (a) *In-situ* QCM analysis of ten consecutive TMA multi-doses onto PMMA indicating the saturation behavior of the polymer film between 30°C and 120°C. A lower maximum exposure temperature was selected in comparison to other polymer chemistries due to the melting temperature of PMMA at 130°C. **(b & c)** The infiltration of TMA in PMMA is explored in more detail by separating the absorbed and reacted components of the TMA mass uptake behavior from Figure 4. (a)

Figure 3.5. (a) *In-situ* QCM analysis of ten consecutive TMA multi-doses into a series of acrylic polymer films at 60°C. The length of the pendant group increases from PMMA to PBMA as the addition of C-H groups increases. This has an effect on the T_g of each polymer film which varies from 115°C for PMMA to 15°C for PBMA. **(b)** The infiltration of TMA is explored further by investigating the absorbed TMA per dose of each polymer in the series.

Figure 3.6. (a) *In-situ* QCM analysis of ten consecutive TMA multi-doses in PET between 30°C and 150°C. The data indicates that at higher reactor temperatures, a saturated mass gain is not observed within the time frame of the experiments. **(b & c)** The infiltration of TMA in PET is explored in more detail by separating the absorbed and reacted components of the TMA mass uptake behavior.

Figure 3.7. (a) *In-situ* QCM analysis of 100 consecutive TMA multi-doses onto PET thin at 100 °C. An exposure temperature of 100 °C was selected since the greatest mass gain, as

shown in Figure 6, was achieved at this temperature. The data proves that a significantly larger number of TMA doses are required to saturate a PET film. **(b)** The infiltration of TMA in PET is explored in more detail by separating the absorbed and reacted components of the TMA mass uptake behavior.

Figure 3.8. ToF-SIMS depth profiles are used to elucidate the bulk infiltration of TMA in PET at 100°C after (a) 10 TMA doses and (b) 50 TMA doses. The Al⁺, Si⁺ and C⁺ markers represent TMA, Si wafer support and PET polymer film, respectively.

Figure 3.9 Schematic diagram describing the sub-surface nucleation behavior of TMA in PA-6 and PET based on observations from in-situ QCM analysis as shown in this. The Figures indicate possible reaction modes between TMA and functional groups along the backbone of PA-6 and PET polymer chains.

Figure 3.10. Schematic diagram representing the sub-surface infiltration of TMA in PMMA using observations from in-situ QCM analysis shown in Figures 5 and 6. The weak interaction between the interfaces of the gold plated quartz crystal and PMMA polymer film corresponds to a lower T_g at the free surface. This promotes the absorption of TMA into the sub-surface of the polymer where reactions take place with functional groups within denser regions of the polymer film.

Figure 4.1 *In-Situ* QCM analysis of a complete SVI process in a PBT polymer thin film at 60°C. The figure indicates the mass gain associated with the TMA and water exposure cycles separated by an inert gas purge step. The mass uptake behavior of TMA in PBT via the SVI technique is compared to the mass uptake behavior of an alumina ALD process at 60°C.

Figure 4.2. *In-situ* QCM analysis comparing the mass uptake of ten consecutive TMA exposure steps to PBT and PA6 films at 60°C. Panel (a) and Panel (b) compare the mass uptake of TMA dose and hold steps in PBT and PA-6, respectively using a half exposure cycle of TMA Dose/Hold/Purge = 0.2/30/90 seconds. The mass uptake behaviour of dose and hold steps in PBT and PA-6 are compared with TMA multidoses using an ALD cycle sequence of TMA/N₂/H₂O/N₂ = 0.2/60/0/60 seconds.

Figure 4.3. ToF-SIMS depth profiles are used to demonstrate the bulk infiltration of TMA in PBT and PA-6 at 60°C after exposure to 10 TMA half exposure cycles of the SVI process. The CsAl⁺, Si⁺ and C⁺ markers represent alumina, Si wafer support and polymer films, respectively

Figure 4.4. For clarification, the figure indicates the absorption of TMA within PBT attributed to the hold step of the SVI technique in comparison to the absorption of TMA via an ALD multidosing scheme.

Figure 4.5 Panel (a). Time segment comparing the first dose and hold step of the SVI process highlighting the characteristic mass uptake behavior of TMA in PBT at 60°C with a cycle sequence of TMA Dose/Hold/Purge = 0.2/X/90 seconds, in which X = 0, 30, 45 and 60 second hold steps. **Panel (b).** Time segment comparing the effect of dose time on the

characteristic mass uptake behavior of TMA in PBT at 60°C with a constant hold time of 60 sec.

Figure 4.6. Time segment comparing variations in both dose time and hold time of the SVI process highlighting the characteristic mass uptake behavior of TMA in PBT at 60°C.

Figure 5.1. XRD Diffractogram of PET specimens annealed under different heating conditions to vary crystallinity. The diffractogram shows the formation of crystalline peaks characteristic of the crystallographic planes (010), ($1\bar{1}0$), and (100) for scattering angles $2\theta = 17.5, 22.5$ and 25.5° , respectively.

Figure 5.2. Mass uptake behavior of TMA in PET polymer films with different crystallinities. *In-situ* QCM was used to monitor the mass uptake of 10 consecutive multidoses of TMA in PET at 100°C using an ALD cycle sequence with an eliminated water dose.

Figure 5.3. Diagrammatic representation of the effect of crystallites on the diffusion of precursor vapor and the corresponding mass uptake as measured by in-situ QCM analysis.

Figure 5.4. DSC thermogram of PET fiber specimens explored in this study. The thermograms were obtained using a heat rate of 20°C/min.

Figure 5.5. Peak load-elongation curve of the control specimens (*i.e. unmodified specimens*) for the 1:1, 1:2 and 1:4 PET fiber samples. The data was obtained using a 250lb load cell and a crosshead speed of 15 mm/min in a conditioned laboratory at 21°C and 65% RH.

Figure 5.6. Peak load-elongation curve of PET fibers modified by sequential infiltrations of TMA at 50°C. The mechanical properties of modified and control fibers are compared to elucidate the process-structure-property relationships of the PET fibers. The data was obtained using a 250lb load cell and a crosshead speed of 15mm/min.

Figure 5.7. Diagrammatic representation of the infiltration of TMA into the bulk of the PET fibers forming intra-chain R-O-Al-O-R complexes. These act as a mechanical buffer within the amorphous region of the fiber by preserving the structure and reinforcing the orientated amorphous chains.

RESEARCH OUTLOOK

I. Overview of the literature

Atomic layer deposition (ALD) is a technique of forming a broad range of nanoscale films on a surface by sequential exposures of an organometallic precursor and a co-reacting vapor species such as water. The principle of ALD growth is based on the cycling of organometallic precursor and co-reactant vapor exposures separated by an inert gas purge step. The corresponding self-limiting chemical reactions result in atomic scale precision of the pinhole free, conformal coatings on both planar and complex surfaces. A comprehensive description of the principal features of the ALD process and 'ALD like' processing can be found in the literature.^{1,2}

A wide range of oxides, nitrides and pure metals have been demonstrated on a range of surfaces. However, the most well studied and well understood ALD process is the alumina ALD process that is typically formed by trimethylaluminum (TMA) and water exposures. The highly favorable free energy change of the overall deposition reaction between TMA and water (~ 370 kcal/mol)² corresponds to an 'ideal' ALD process. A review by Puurunen describes the TMA/water alumina ALD process in great detail from the perspectives of surface chemistry, saturation behavior and growth mechanisms.³

It has been demonstrated that the direct reaction between certain ALD precursors and an organic substrate can form a hybrid organic-inorganic film.^{4,5} A unique feature of hybrid materials is the formation of a material that is neither purely organic nor inorganic. A desirable feature of hybrid materials is the incorporation of inorganic material properties such as: excellent thermal stability, high dielectric constants, low permeability's, photocatalytic behavior and chemical resistance, without compromise to the attractive properties of organic materials such as flexibility and ease of form.⁶⁻¹⁰

Depending on the processing technique and materials used, the development of hybrid materials affords the opportunity to tailor the properties of a material for a specific application. Therefore, the innovative materials space transition by hybrid materials offers opportunities to acquire materials with unique mechanical, electrical, and optical behavior.

Hybrid coatings are formed as a result of precursor diffusion through the porous sub-surface of the organic material which is followed by chemical reaction and nucleation.^{4,11} Therefore, in contrast to the surface self-limiting reactions of a traditional ALD process, the precursor diffusion and reaction process is distinguished by an infiltration mechanism that is limited by the number of reactive sites that are accessible within the bulk of the material as the process proceeds. Hybrid organic-inorganic film formation via ALD was initially demonstrated on polyamide-6 (PA-6).⁴ The reaction that occurs between TMA and the carbonyl group along the PA-6 backbone has also been shown to occur with polyethylene terephthalate (PET), polybutylene terephthalate (PBT), polylactic acid and poly(methyl methacrylate) (PMMA).^{4, 11-14} A bilayer surface form as a combination of infiltration and ALD processes, resulting in a hybrid metal-oxide polymer layer followed by dense ALD layer nucleated outward from the polymer surface, respectively. These results have inspired adaptations to the ALD process which extend the precursor exposure conditions to promote the infiltration mechanism. Processes such as multiple pulse infiltration^{15,16}, sequential infiltration synthesis¹⁷ and sequential vapor infiltration¹⁸⁻²⁰ are described in the literature.

As described above, the driving force behind the infiltration mechanism that promotes the formation of a hybrid organic-inorganic coating is the ability for the organometallic precursor molecules to diffuse into the polymer subsurface. To date, the evidence of hybrid growth within polymers using ALD processes is supported in the majority of the literature by ex-situ characterization methods such as cross section TEM, XPS and FT-IR and in-situ methods such as

quartz crystal microgravimetry (QCM).²¹⁻²³ These techniques are pertinent analytical tools for probing the growth mechanism (TEM, QCM) and elucidating the fundamental chemical reactions between precursors and functional groups of the polymer (XPS, FT-IR). In-situ FT-IR has also been used to investigate the fundamental chemical reactions between precursors and polymer functional groups during a process.¹⁴ QCM is particularly useful for investigating the growth of hybrid coatings due to its incredibly low mass resolution that is attributed to the high Q-factor, high frequency oscillation of the piezoelectric quartz crystal. The utilization of QCM has successfully elucidated the unique absorption/desorption behavior of a broad range of polymers exposed to different organometallic precursors. Furthermore, QCM analysis has revealed the infiltration of precursors into polymers as indicated by unusually high initial mass gains and transient growth periods prior to linear growth regimes typical of traditional ALD processing.^{4, 11, 14}

Efforts to develop growth mechanisms that describe the infiltration of precursor in polymers include fundamental studies to elucidate the diffusion of precursors during ALD processing. A review by Knez discusses diffusion phenomena in ALD however, from the principle viewpoint of surface and interfacial diffusion that is characteristic of traditional ALD processing. Diffusion through coatings and diffusion into substrates i.e. polymers, is briefly discussed however, from a purely qualitative outlook.²⁴ The physics required to describe the motion of small molecules through a polymer already exists. Henderson used a physical theory of diffusion based on Fick's law, to describe the motion of precursors through polymer masking layers used in area selective ALD.²⁵

The physics of such diffusion-reaction processes exist and inspiration can be drawn from polymer fiber processes such as reactive dyeing which involves the diffusion of dye molecules and subsequent chemical reaction with functional groups of the polymer.²⁶ However, one of the significant challenges of developing a physical model is accounting for the effect that varying process

temperatures and chemical reactions between precursors and functional groups of the polymer has on the successive diffusion of precursors within polymers. Before a comprehensive physical model can be developed, a more extensive investigation based on the infiltration of organometallic precursors through polymers within a wider temperature range in addition to understanding fundamental chemical reactions is an important area of focus.

II. Organization of Dissertation and Key Findings

Since the diffusion coefficient of a molecule through a polymer is influenced by factors such as temperature and polymer morphology, it is clear that a comprehensive understanding of polymer science in addition to ALD process conditions is required to understand the hybrid material formation in polymers. To this end, Chapter 1 describes the important states of semi-crystalline polymers, namely the amorphous and crystalline regions. This is followed by a brief description of fiber formation and fiber properties with a principle focus on mechanical properties and transport behavior. The section on transport behavior elucidates the basic physics that describes the motion of small molecules through a polymer with examples from reactive dyeing and diffusion through polymer membranes. Finally, hybrid materials and the ALD technique on polymers are introduced followed by a description of modified ALD processes that promote reactive vapor infiltration. This is complemented by a short section outlining high throughput processes and their future development.

Chapter 2 focuses on a range of polymers which have subtle variations in microstructure to elucidate the nucleation behavior of inorganic coatings on polymers in more detail. Specifically, in-situ quartz crystal microgravimetry is employed to understand the nucleation behavior of alumina ALD in a series of poly-n-methacrylate and polyester thin films. The data indicates that the glass transition temperature, as influenced by variations in

microstructure, has a significant impact on the absorption of TMA. Polymers that possess lower T_g 's absorb larger quantities of TMA due to a larger free volume whereas polymers with higher T_g 's absorb less TMA due to a reduced free volume. Furthermore, the presence of side chain pendant groups in poly-n-methacrylate polymers hinders the absorption and desorption of unreacted TMA due to the tortuous path of interconnected pores created within the polymer film. This work shows that the influence of polymer microstructure on the absorption and desorption characteristics of organometallic precursors must be considered and the ALD process parameters adjusted accordingly to promote the formation of desirable inorganic material interfaces.

To study the influence of polymer free volume in more detail, Chapter 3 introduces the reactive vapor infiltration of precursors into polymers as the exposure temperature is varied. Specifically, in-situ quartz crystal microgravimetry (QCM) is employed to understand the infiltration and saturation behavior of TMA in PA-6, poly(acrylic acid) (PAA) and PET. The study indicates that the glass transition temperature of the respective polymers has a significant impact on the infiltration behavior of precursor molecules into polymers. Potential growth mechanisms based on the temperature dependent observations in the work are stated that lead to the understanding of hybrid organic-inorganic formation in polymers.

The infiltration of organometallic precursors into certain polymers has inspired adaptations to the ALD process such as sequential vapor infiltration (SVI) which enhances the diffusion of organometallic precursor into the sub surface of polymer to promote the formation of a hybrid organic-inorganic coating. Chapter 4 highlights the fundamental difference in mass uptake behavior between ALD and SVI using *in-situ* methods.

For the first time *in-situ* QCM is used to compare the mass uptake behavior of TMA in polybutylene terephthalate (PBT) and PA-6 films via both ALD and SVI techniques. The importance of TMA infiltration into the polymer film and the subsequent chemical reactions with polymer functional groups are discussed in the work. The key findings state that the ‘hold step of the SVI process promotes infiltration of TMA by increasing exposure resulting in significantly large quantities of absorbed TMA in comparison to the ALD technique.

Finally Chapter 5 explores the infiltration of organometallic precursors into fiber forming polymers and the subsequent formation of a hybrid material interface. To explore this in more detail, *in-situ* QCM is employed to investigate the infiltration of TMA into PET. Specifically, the effect of crystallinity on the infiltration mechanism in PET polymer films with varied crystallinities is investigated. Finally, the effect of TMA infiltrations on the mechanical behavior of fibrous materials is also investigated. In particular this report highlights the structure-process-property relationships between modified and unmodified PET fibers infiltrated with TMA via the SVI technique. The results indicate that the peak load and elongation of the PET fibers increase with exposure to TMA.

CHAPTER 1

INTRODUCTION

1.1. THE STRUCTURE OF SEMI-CRYSTALLINE POLYMERS

1.1.1 Polymer Structure

Semi-crystalline polymers are a distinctive class of material consisting of macromolecules that are visualized as long chains made of a unique chemical repeat unit. Due to their long chain nature, semi-crystalline polymers possess a broad range of phenomena as described by their polymer physics such as, a glass transition and visco-elastic behavior, which distinguishes them from other materials. However, it is their unique polymer chemistry that allows the behavior of one polymer to be distinguished from another.²⁷ An individual polymer's behavior is determined at the primary level by the chemical composition of its repeat unit and at the secondary level by the configuration and conformation of each repeat unit connected in a polymer chain. This determines the way that the polymer chain bends and folds as it pervades the volume that it occupies. Consequently, segments of the polymer chain can be found in two main states, namely the amorphous state and the crystalline state.

1.1.2 Amorphous Region

The amorphous region of a semi-crystalline polymer possesses an unordered, entangled structure. The total volume, V_T , pervaded by the system of polymer chains can be split up into two sections as shown in Figure 1.1²⁸ Namely the volume that is physically

occupied by each constituent atom, V_o , that makes up the polymers long chains and the unoccupied volume, V_f that is typically called the polymer free volume. At the melt temperature, crystalline materials experience a sharp melting point followed by a sharp increase in volume as molecular packing becomes disordered and the increase in interatomic spacing causes a significant increase in free volume between constituent atoms.²⁹ At the onset of melting, X-ray analysis indicates an amorphous halo rather than the specific X-ray bands of the crystalline material. Conversely, semi-crystalline polymers possess a continuous increase in volume as the melting process takes place over a larger temperature range. At a specific temperature, it is possible to observe a discontinuity in the Volume versus Temperature plot of Figure 1.1 indicating that there is an abrupt change in the expansion coefficient of the semi-crystalline polymer.

Starting from the melt, as the polymer is cooled quickly the motion of polymer chain segments is greatly reduced. If the cooling rate is much larger than the re-orientation time of the polymer (*also called the relaxation time*) it is unable to volumetrically relax therefore, excess free volume is 'frozen' inside the polymer. This is called the glassy state hence; the discontinuity in the Specific Volume versus Temperature plot is associated with the temperature at which the polymer changes from a flexible rubbery material to a brittle glassy material and is thus named the glass transition temperature, T_g . At temperatures above T_g , polymer chains have greater mobility and larger segments of the polymer chain are able to re-orient therefore, they are able to achieve their equilibrium conformations which corresponds to an increase in free volume. Below T_g , polymer chain mobility is greatly decreased corresponding to a reduction in polymer free volume.

Significant efforts have been made to model the glass transition phenomenon. A single theoretical understanding of T_g has not been formulated therefore; the theoretical models that describe T_g can be separated into three main categories, namely the thermodynamic, kinetic and free volume theories. The following section provides a conceptual approach to describe each of the theories individually.

Arguments for a thermodynamic T_g includes the fact that when a polymer is cooled from the melt, volume changes are associated with the conformational rearrangement of the polymer chains which determines the conformational entropy (S_c) of the system.³⁰ Furthermore, the discontinuity demonstrated by the volume changes of the polymer as a function of temperature is also observed in thermodynamic quantities such as the specific heat capacity, enthalpy and expansion coefficient. For example, if the derivative of the specific volume with respect to temperature is plotted versus temperature, the glass transition temperature is indicated by the turning point on the curve as shown in Figure 1.2. Therefore, T_g is considered to be a second order transition. The thermodynamic theory of Gibbs and DiMarzio (1958)³¹ considers the conformation entropy of the polymer chains as a function of temperature. In 1948, Kauzmann published a theory which suggested that the extrapolated conformational entropy passes through zero at very low temperatures.³² This is thermodynamically 'forbidden' therefore, Kauzmann recommended that the material will undergo a phase transition and crystallize before the conformational entropy reaches zero. However, ten years later Gibbs and DiMarzio recognized that the crystalline state was not true for all materials since some polymers possessed an equilibrium amorphous state over a broad temperature range. Consequently, the Gibbs DiMarzio theory overcomes the

Kauzmann paradox by stating that the glass formation occurs when the conformational entropy is zero at a temperature above zero Kelvin as shown in Figure 1.3.³⁰ This is due to the fact that as conformational entropy approaches zero, the number of arrangements of polymer chain segments decreases since there are fewer vacancies at lower temperatures. A consequence of the thermodynamic theory is that the second order transition can only be observed if the polymer is cooled infinitely slow i.e. the relaxation time of the polymer chain segments is comparable to the time scale of the cooling experiment. This forms the fundamental basis for the kinetic theory of the glass transition temperature.

In the kinetic theory, T_g is not a thermodynamic variable but it is associated with the rate at which the polymer achieves equilibrium. Therefore, T_g is the temperature at which the time scale of the experiment *i.e.* rate of cooling, is equal to the relaxation time of the polymer chain. This forms the basis of the conceptual approach of the Kinetic theory of T_g .³⁰

In thermal experiments, it is important to note the hysteresis and aging effects associated with the T_g of polymeric materials and the effect that cooling and heating rates have on their ability to achieve an equilibrium volume. Firstly; faster cooling rates have been shown to correspond to a higher T_g while slower cooling rates lead to a lower T_g since the polymer chains have more time to adjust to their environment and the polymer approaches its equilibrium volume.³³ Furthermore, storage temperature has an important effect on the specific volume of the polymer as demonstrated diagrammatically in Figure 1.4.³³ If the polymer is cooled rapidly and maintained at a temperature close to T_g , the polymer chains will relax and assume their equilibrium conformation in a shorter period of time compared to

a storage temperature well below T_g . The higher storage temperature releases the free volume 'frozen' inside the polymer upon cooling which corresponds to volume shrinkage. The same is true if a rapidly cooled polymer is stored at a temperature well below T_g and exposed to a slow heating rate. The polymer chains have time to adjust to the environment they were exposed to upon cooling and assume their equilibrium conformation which also leads to volume shrinkage below T_g . Mathematically, the rate of volume shrinkage is proportional to the volume at time t (V_t) minus the volume at infinity (V_∞) as stated in Equation 1.³⁰

$$\frac{dV}{dt} = -\left(\frac{1}{\tau}\right) (V_t - V_\infty) \quad (1)$$

where τ is the relaxation time of the polymer chains.

The kinetic theory provides a useful understanding of the effects of aging on polymer properties which is of commercial importance and states the significance of experimental time scales on T_g which is essential for analytical methods such as DSC.

Some of the most notable theoretical developments of the glass transition include the free volume theories which form the fundamental basis for understanding other polymer properties such as transport properties discussed in Section 1.2.6. The most historical free volume theory is that developed by Williams, Landel and Ferry, also called WLF theory.^{30 - 35} The principle behind the theory is associated with the volume-temperature relationship demonstrated in Figure 1.1 As the glass transition is approached from the melt, polymer specific volume and free volume decrease. At a certain temperature below T_g , the polymer

free volume reduces to a critical volume which imposes polymer chain segmental motion. Therefore, in general, WLF theory relates the microscopic changes in the magnitude and re-distribution of polymer free volume as temperature is varied to the global value of T_g . The mathematical description of the WLF theory begins with the Doolittle equation:³⁴

$$\mu = Ae^{\left(\frac{BV_0}{V_f}\right)} \quad (2)$$

where μ is the polymer viscosity, B is a numerical constant and V_0 and V_f are the occupied and free volumes respectively. The WLF theory is developed by solving the ratio of the viscosity at any temperature, T and the viscosity at T_g which leads to the following expression:

$$\ln\left(\frac{\mu_T}{\mu_g}\right) = \ln a_T = B\left(\frac{1}{f_T} - \frac{1}{f_g}\right) \quad (3)$$

where f_T and f_g are the free volume fractions at temperatures T and T_g respectively.

Assuming that the free volume fraction increases above T_g with the expansion coefficient, then the fractional free volume at any temperature, T , above T_g may be summarized by Equation 4:³⁴

$$f_T = f_g + \alpha_f(T - T_g) \quad (4)$$

By substituting Equation 4 into Equation 3 the WLF equation is obtained:

$$\log(a_T) = -\frac{B}{2.3f_g} \left[\frac{T-T_g}{(f_g/\alpha_f)+T-T_g} \right] \quad (5)$$

The typical ‘universal’ form of the WLF equation that is valid for a broad range of polymers is shown in Equation 6:

$$\log(a_T) = \frac{c_1(T-T_g)}{(c_2+T-T_g)} = \frac{-17.4(T-T_g)}{51.6+T-T_g} \quad (6)$$

The universal constant in Equation 6, $c_1 = 1/2.3f_g = 17.4$ indicates that the fractional free volume at the glass transition temperature is approximately 2.5% for a broad range of polymers. Similarly the constant, $c_2 = f_g/\alpha_f = 51.6$ suggests that the free volume expansion coefficient, using $f_g = 2.5$, is approximately $4.8 \times 10^{-4} K^{-1}$. While this is not the case for all glassy polymers it is a reasonable approximation as shown in Table 1.1³⁶

The WLF theory is useful for understanding visco-elastic events, transport phenomena, the effect of molecular weight and plasticizer content on Tg and understanding the relationship between coefficients of expansion above and below Tg.

1.1.2 Crystalline Region

The driving force behind crystallization is the necessity of a material to achieve its lowest energy state which dictates the microscopic morphology of a material. Therefore, given adequate time most materials crystallize. However, one of the significant factors that prevent a polymer from being 100% crystalline is the chain entanglements that form in the melt. As the polymer melt is cooled, the chain entanglements cannot disentangle quick enough to allow the long polymer chain to pack into a lattice and crystallize.²⁹ Furthermore, crystallization in polymers is affected by the presence of bulky functional groups or asymmetry along the main chain. Therefore, crystallinity in polymers is favored by regularity

such as, isotactic and syndiotactic configurations, which allows the polymer chain to fold and pack into a specific crystal lattice.

Polyethylene is one of the simplest polymers to describe the packing of long polymer chains within a crystal lattice. There are two important stages associated with crystallization from the melt. Firstly, the polymer chains obtain their equilibrium conformations in order to be in the lowest energy state. The equilibrium conformation of polyethylene is the planar zigzag structure in which the angle between bonds is approximately 112° . Secondly, the polymer chains pack together into a lattice with lattice constants a, b and c which for polyethylene are 7.41, 4.94 and 2.55 respectively.^{29, 35} The polymer chains are arranged parallel to each other in the crystal lattice with a high degree of orientation in order to achieve the lowest energy state i.e. to minimize the Gibbs free energy. Since the unit cell of polyethylene is the smallest representation of the crystal, the entire crystal can be constructed via translations of the unit cell by lattice vectors equal to the lattice parameters a, b and c. Although bulky side groups may inhibit crystallization by preventing the packing of polymer chains within the crystal lattice, some polymer chains may overcome this by introducing 'twist' along the polymer backbone which prevents the overlap of the larger atoms. The result is the formation of polymer chains with helical twist within the crystal lattice.²⁹ For example, the center of each hydrogen atom in polyethylene is separated by approximately 254pm. The diameter of a fluorine atom is approximately 270pm therefore, the planar zigzag structure is not suitable for polytetrafluoroethylene (PTFE) to pack into a similar crystal lattice as polyethylene. To overcome this, the PTFE backbone rotates approximately 20° and the C-C bond opens up to approximately 116° ^{29, 35} In polymers such as polyamide-6 (PA-6)

intra-chain hydrogen bonds between the hydrogen atom of the amine group and oxygen atom of the carbonyl group promote crystallization by orienting neighboring chains. Conversely, the crystallization of polyethylene terephthalate is affected by secondary bonding between aromatic rings which stack in the c direction of the crystal lattice to maximize their electronic interaction.³⁵

1.2 FORMATION AND PROPERTIES OF FIBER FORMING POLYMERS

1.2.1 Fiber Formation

There are numerous manufacturing processes available to form both natural and synthetic continuous fibers such as wet spinning, dry spinning, and melt spinning. Wet spinning, in which the polymer has first been dissolved in a solvent, is the adopted process for forming acrylic, rayon and aramid fibers. Dry spinning is also used for forming fibers from a polymer/solvent solution however, contrary to wet spinning in which the polymer precipitates from solution; the polymer is solidified by the evaporation of the solvent via the application of dry air or inert gas. A specialized method of forming micro to nano sized fibers is the electrospinning process. In which fibers are formed by the application of a voltage to a polymer solution. The voltage causes the polymer solution to become charged and if the voltage is sufficiently large the electrostatic repulsion of the liquid is capable of overcoming the surface tension of the liquid. This force's the liquid to elongate forming a jet that dries and solidifies as it travels from a spinning tip to a grounded collector plate. Melt spinning, in which a thermoplastic polymer is converted from a solid into a molten viscous

liquid, is the typical method for forming fibers such as polypropylene, polyesters and polyamides.

1.2.2 Melt Spinning

In melt spinning, fibers are formed by extruding³⁷, that is to force the viscous polymer liquid at high pressure through a spinneret via a mechanical pump as shown in Figure 1.5. The spinneret is analogous to a shower head and contains a series of tiny holes from which the polymer liquid emerges. Prior to extrusion, polymer chips or beads are dried in air, typical drying temperatures and times for polyester and polypropylene are 120 and 70°C for 4 hours respectively. The removal of water is particularly important prior to melt spinning of polyester due to hydrolysis that can correspond to polydispersity of the molecular weight which can reduce the melt strength of the polymer and its mechanical properties after extrusion. After drying, the polymer is fed into a storage hopper and converted into a molten liquid in a melt grid. Typical melt temperatures of polyester, polyamide-6 and polypropylene are, 240, 220 and 170°C respectively. Once the polymer chips or beads have been converted into a molten liquid, it is transported from the melt grid to the spinneret via a mechanical spin pump. The polymer emerges from the spinneret and enters the spin shaft which is also called the quench zone. A cooling air inlet and series of fans solidifies the polymer as it passes through the quench zone which initializes crystal growth within the polymer. At the end of the quench zone, the fibers are passed through a spin finish which prevents the buildup of static charge and allows the fibers to move freely over a series of rollers which consists of a

take-up roller, draw roller and relax roller. The series of rollers stretch the fiber and further crystallize the polymer by orienting adjacent polymer chains within the fiber axis.

The drawing process is important for establishing certain mechanical properties within the fiber such as percent elongation at break, toughness and ultimate tensile strength. There are two main strategies to introduce mechanical properties within the fiber which include drawing the fiber during quench and drawing the fiber after quench. To draw the fiber during quench, the take up roller and draw roller are typically maintained at the same speed while the relax roller is always maintained at a slightly lower speed to take tension off the line. This is important for the storage of the tow since high tensions builds up within the fiber line at high take-up speeds which can crush the packages that they are wound onto. Increasing the speed of the take-up roller increases the orientation of the polymer chains which increases the crystallinity of the fiber. In general, high take-up speeds are required to induce crystallinity within the fiber; however, this requires higher mechanical pump velocities and certain polymers do not possess the melt strength to cope with the high velocities. Therefore, drawing fibers after quench, typically called cold drawing, is the most suitable strategy for polymers with lower melt strengths. During cold drawing, a ratio of velocities is created between the take up roller and draw roller. For example, if the take-up roller is running at 500 mpm and the draw roller is running at 2000 mpm, this corresponds to a draw ratio of 4. Drawing the fiber via this type of process elongates the crystalline region of the polymer, increases orientation of the polymer chains within the fiber.

The art of fiber formation via melt spinning is not only dependant on polymer chemistry and molecular weight; but it is a careful balance between the quench temperature, quench rate and drawing process. However, variations in polymer chemistry and molecular weight distinguish the behaviors of different polymers from each other and determine the optimum spinning parameters to achieve a given mechanical property. In general a fast quench, fast stretch process corresponds to fibers that possess a fringed fibril structure in which crystalline regions are aligned and amorphous regions are greatly extended and oriented. Conversely, a fast quench, slow stretch process corresponds to a fiber with a fringed-micelle structure. These fibers are typically referred to as partially oriented fibers or yarns and do not typically serve a broad range of application due to lower mechanical properties.

1.2.3 Nonwovens

In comparison to single fibers or yarns, nonwoven fabrics are defined as web structures bonded together by entangling fiber or filaments mechanically, thermally, or chemically. Nonwovens have a flat, porous structure made from separate fibers or molten polymer and do not require weaving or knitting to form fabrics.³⁸

Nonwoven webs can either be made with natural and synthetic fixed length staple fibers or synthetic continuous filaments. The choice of fiber type is important in determining the method of web formation. In general, staple fiber nonwoven webs are made by a wet lay or dry lay process in which a water slurry of fibers is sprayed onto a conveyer or, in the case

of the dry lay process, the nonwoven web is formed by carding and cross-lapping as shown in Figure 1.6.³⁹

For synthetic continuous filaments, the nonwoven web may be formed by meltblown or spun bond processes as shown in Figure 1.7.³⁹ The difference between these two processes is that the melt blown process does not require a post process bonding step to add integrity to the web. For the spunbond process, bonding of fibers may be achieved by mechanical bonding, thermal bonding or chemical bonding. Examples of mechanical and thermal bonding include needle punching, hydroentangling and calendaring respectively.

Typically, nonwoven fabrics have been predominantly used as disposable, single use engineered materials satisfying uses in a broad range of applications such as health and hygiene, wipes, filtration, and medical. This distinguishes nonwoven fabrics from traditional textiles which are widely used for apparel. The driving force behind the production of nonwoven fabrics, of which approximately 6 million tons of nonwoven roll goods are produced each year, is high speed, large volumes and low cost.⁴⁰

As mentioned above, due to the production of large volumes of nonwoven fabrics at high speed, the focus of nonwoven products has mainly been single use applications. However, there is a growing trend in the production of durable nonwovens for technical textile applications that emphasize functionality and performance. It is important not to confuse durable nonwovens with long life nonwovens such as geosynthetic fabrics used in building applications therefore, herein; durable refers to a material that more than sufficiently performs its job. It has been stated that two important contributions to the production of

durable nonwovens include Polymer Group Inc's (PGI) Miratec fabrics and Freudenberg Nonwovens Evolon.⁴⁰ The former product, Miratec, is a durable nonwoven made from staple fibers that possesses good strength, and a high resistance to fraying or pilling. The high strength of Miratec fabric allows the use of lighter basis weights to achieve similar performance of parallel fabrics of higher basis weights.⁴¹ The later product, Evolon, is made from a 'splittable' continuous fiber. The 'splittable' fibers are achieved by the formation of continuous fibers named bicomponent fibers which are synthesized from two dissimilar polymer types that come apart mechanically during the web formation process. The result is a versatile, durable, high strength microdenier fiber that is light weight and compact.⁴² Although nonwoven fabrics have not traditionally been used in technical textile applications, there is a growing trend in the development of durable, high performance nonwoven fabrics as industry searches for new niche market opportunities and academic institutions shift their curiosity towards the development of novel, flexible materials based on natural and synthetic polymers.

1.2.4 Fiber Properties

So far the discussion of polymers has included a description of their unique semicrystalline structures and the methods used to form useful materials such as fibers. The property of a fiber such as optical, dielectric, electrical, thermal, mechanical and transport properties are influenced by the chemistry of the polymer's repeat unit and the ratio of crystalline regions to amorphous regions which is also determined by the fiber formation as

described in Section 1.1.1. The Fiber properties important to this study include mechanical properties and transport properties of textile fibers.

1.2.5 Mechanical Properties

During a tensile test, the load cell applies a stress, defined as the force per unit area, to the fiber which causes an elongation.⁴³ Since there is a broad range of fiber cross-sectional areas it is convenient to use the linear density of the fiber which is often referred to as the fiber denier. If a fiber has a denier of 1, the linear density corresponds to 1 gram per 9 km of fiber. Therefore, the specific stress is defined as the force measured in gram-force (gf) or Newton's (N) per denier i.e. *gf/den* or *N/den*. The elongation or strain is defined as the change in length divided by the original length of the fiber i.e. $\varepsilon = \frac{\Delta l}{l_0} = \frac{l-l_0}{l_0}$ where l is the length of the fiber after a certain extension and l_0 is the original length.

Figure 1.8 shows a diagrammatic representation of a stress-strain curve of a typical textile fiber where the stress on the y-axis is plotted versus strain along the x-axis. The modulus of the material can be estimated by the slope of the stress-strain curve. Firstly, the initial modulus can be calculated at zero strain however, the modulus can be calculated at a certain % strain for example a 10% offset. The toughness of the fiber, also considered the work required to rupture the fiber, can be calculated by the area under the stress strain curve.

Three regions are highlighted in Figure 1.8, namely the elastic, plastic and permanent deformation regions. As the fiber is stressed, the amorphous chains uncoil and elongate. In the elastic region between $\varepsilon = 0$ and ε_1 , if the load is released the fiber is able to achieve full

recovery as the amorphous chains are able to obtain their original conformations. The stress-strain behavior in the elastic region maybe described by Hook's law: $\sigma = E\varepsilon$. At a certain yield point, which is determined by the point at which the initial slope of the curve meets the slope of the plastic region, the fiber enters the plastic region. As the fiber is stressed in the plastic region the crystalline segments begin to tilt in the direction that they are being drawn. As the stress continues to increase the strain on the fiber causes the amorphous chains to extend and adjacent crystalline and amorphous regions begin to align. The amorphous chains experience some permanent deformation however, if the load is released, the amorphous chains are able to elastically recover some of the strain. Finally, the stress imposed on the fiber is sufficient to cause permanent deformation on the fiber. In this region between ε_2 and ε_3 the amorphous chains are fully extended and unable to elastically recover some of the strain. The stress also causes the crystalline region to break up into smaller crystals. Finally, the fiber fails when the amorphous chains between crystals begin to break as they are unable to support the load.

The stress-strain behavior of textile fibers exist in in four main categories: synthetic fibers with high modulus and high strength, tough synthetic fibers, weak synthetic or natural fibers, and elastomeric fibers. The characteristic stress-strain curves are summarized in Figure 1.9.⁴³

One can see that there is a compromise between high performance high tensile strength fibers with lower elongations at break and fibers that have large elongations at break and lower tensile strengths as indicated by weak extensible or elastomeric fibers. The origin

of this observation in tensile properties is confined within in the polymer structure of the fiber. Imagine that we have produced two polymer fibers with the same linear density. One polymer fiber has a fringed fibril structure with a high degree of orientation and percent crystallinity while the other fiber has a fringed-micelle structure with a higher amorphous content. The fiber with the higher degree of orientation and percent crystallinity possesses a greater ultimate tensile strength and a larger modulus while the more amorphous fiber possesses a greater elongation at break. The amorphous and crystalline regions of the fiber with the greater crystallinity are highly oriented and the polymer chains in the amorphous region are fully extended therefore, the polymer fiber behaves more elastically under tensile strain. In comparison, the polymer chains in the more amorphous polymer are randomly coiled and entangled therefore, under tensile strain the randomly coiled chains are able to unfold and untangle resulting in large elongations prior to failure. The dotted curve in Figure 9 represents a fiber that possesses both high strength and high toughness which, as described above, is not observed in synthetic fibers. However, some biological organisms such as spiders are capable of engineering fibers with both high strength and high toughness.

The time scale of the tensile test experiment has a significant impact on the final properties of the polymer fiber. For example, fast test speeds correspond to an increase in modulus due to the fixed polymer chain entanglements which correspond to constrained motion as stress is applied to the fiber. Conversely, slow test speeds correspond to greater elongations at break and a lower modulus since the polymer chain entanglements have time to relax and flow past each other. The stress-strain behavior of polymer fibers at slow and fast test speeds is influenced by the visco-elastic behavior that is distinctive of polymers.⁴³

The visco-elastic behavior of polymers may be described mathematically by a simple Maxwell model. The viscous behavior of the polymer is modeled by a dash-pot which has ideal viscous behavior:^{35,43}

$$\tau = \mu \frac{d\gamma}{dt} \quad (7)$$

where τ is the shear modulus, μ is the viscosity and γ is the shear strain.

The elastic behavior is modeled by a spring with ideal elastic behavior:

$$\sigma = E\epsilon \quad (8)$$

where σ is the stress, E is the elastic modulus and ϵ is the extension.

The dash-pot and spring are connected in series and fixed at both ends. Since the spring and dash-pot are attached in series, their strains are additive such that:

$$\epsilon_T = \epsilon_{spring} + \epsilon_{dash-pot} \quad (9)$$

Since the strain occurs at a certain rate the time derivative of each term is taken corresponding to the following relationship:

$$\frac{d\epsilon_T}{dt} = \frac{d}{dt} \frac{\sigma}{E} + \frac{\sigma}{\mu} \quad (10)$$

With respect to stress relaxation, the strain rate is zero therefore the stress can be solved by rearranging Equation 10 and integrating:

$$\frac{d\sigma}{\sigma} = \left(\frac{-E}{\mu} \right) dt \quad (11)$$

Therefore:

$$\ln \sigma = \left(\frac{-E}{\mu} \right) t \quad (12)$$

Finally:

$$\sigma = \sigma_0 \exp \left[\left(\frac{-E}{\mu} \right) t \right] \quad (13)$$

The Maxwell model is not sufficient to explain the exact stress relaxation phenomena observed in polymers therefore, more complex models, such as the Voight-Kelvin model has been developed to overcome the limitations of the Maxwell model.⁴³ However complex these models are, they are still more appropriate for introducing the fundamental visco-elastic behavior of polymers rather than complement experimental data.

1.2.6 Transport Properties

Fick's first law of diffusion states that the rate of mass transfer through a specific area is proportional to the concentration gradient of the diffusing species passing through the medium as shown in Equation 14:²⁶

$$F = -D \frac{dC}{dx} \quad (14)$$

where F is the flux, C is the concentration of the diffusing species and x is the space coordinate normal to the area of the medium. Fick's first law is an example of a steady state diffusion equation in which the accumulation of diffusing species within a material does not change with time.²⁶ Therefore; Fick's first law is suitable for isotropic materials in which the

diffusion coefficient remains the same independent of position. Fick's second law was developed to account for the non-steady state behavior of diffusion in which the buildup of the diffusing species is a function of time:²⁶

$$\frac{dC}{dt} = D \left(\frac{d^2C}{dx^2} + \frac{d^2C}{dy^2} + \frac{d^2C}{dz^2} \right) \quad (15)$$

For diffusion in one dimension, Equation 15 reduces to:

$$\frac{dC}{dt} = D \left(\frac{d^2C}{dx^2} \right) \quad (16)$$

As described above, Fick's laws assume that the diffusion coefficient is constant and that the concentration gradient of the diffusing species is perpendicular to the surface of the material. However, real systems such as textile fibers are anisotropic due to their variation in crystalline to amorphous regions. In general, the diffusion coefficient in amorphous regions is much larger than the diffusion coefficient in the crystalline region since amorphous polymer chains are able to change conformation and create free volume voids large enough to accommodate a diffusing species. Therefore, diffusion can be a function of position in addition to the concentration of the diffusing species and the temperature of the system. Hence, a more generalized form of Fick's law is expressed in Equation 17 which describes diffusion as a function of position and concentration:²⁶

$$\frac{dC}{dt} = \frac{d}{dx} \left(D \frac{dC}{dx} \right) + \frac{d}{dy} \left(D \frac{dC}{dy} \right) + \frac{d}{dz} \left(D \frac{dC}{dz} \right) \quad (17)$$

In one dimension, Equation 17 reduces to:

$$\frac{dC}{dt} = \frac{d}{dx} \left(D \frac{dC}{dx} \right) \quad (18)$$

A further factor of the anisotropy in textile fibers is that the diffusion coefficient may also be a function of direction.²⁶ For example, if a diffusing molecule approaches a crystalline region, it must traverse the boundary of the crystal which means that the measured diffusion coefficient is averaged over the diffusion coefficients in the x, y and z directions. Therefore, the most general form of Fick's first law is provided in Equations (19-21):²⁶

$$-\phi_x = D_{xx} \frac{dC}{dx} + D_{xy} \frac{dC}{dy} + D_{xz} \frac{dC}{dz} \quad (19)$$

$$-\phi_y = D_{yx} \frac{dC}{dx} + D_{yy} \frac{dC}{dy} + D_{yz} \frac{dC}{dz} \quad (20)$$

$$-\phi_z = D_{zx} \frac{dC}{dx} + D_{zy} \frac{dC}{dy} + D_{zz} \frac{dC}{dz} \quad (21)$$

The Cartesian coordinates in Equations 19-21 may be transformed to define the principle axis of diffusion which leads to the most general form of Fick's second law as shown in Equation (22):²⁶

$$\frac{dC}{dt} = \frac{d}{d\zeta} \left(D_1 \frac{dC}{d\zeta} \right) + \frac{d}{d\eta} \left(D_2 \frac{dC}{d\eta} \right) + \frac{d}{d\xi} \left(D_3 \frac{dC}{d\xi} \right) \quad (22)$$

In Equation 22, the diffusion is still a function of position and concentration however, D_1 , D_2 and D_3 are only dependent on the directions ζ , η and ξ respectively. In most diffusion experiments, the diffusion coefficient is measured in one principle direction such that the concentration gradient occurs perpendicular to one direction, for example the x-axis which may translate to diffusion through the front and back or side to side of the material.

Therefore, for homogeneous materials it is acceptable to use the form of Fick's law stated in Equation 16. In this case, D in Equation 16 would be equal to one of D_1 , D_2 or D_3 principle diffusion coefficients.²⁶

Two interesting examples of diffusion through polymers include diffusion through a polymer membrane and reactive dyeing. Each case will be discussed separately.

In a simple sorption experiment a polymer membrane is exposed to a diffusing species under constant pressure. The species diffuses into the polymer membrane and the fractional mass gain i.e., the mass gain at time t versus the mass gain at equilibrium, of the membrane may be measured. If the surface area of the membrane is significantly larger than the thickness of the membrane one may assume diffusion in one dimension and Equation 18 may be used to describe the diffusion of the species through the membrane. The solution to Equation 18 for short diffusion times is stated in Equation 23:²⁸

$$\frac{M_t}{M_\infty} = 8 \left(\frac{Dt}{L^2} \right)^{\frac{1}{2}} \left[\pi^{-\frac{1}{2}} + 2 \sum_{m=0}^{\infty} (-1)^m \text{ierfc} \frac{mL}{4(Dt)^{\frac{1}{2}}} \right] \quad (23)$$

where $\frac{M_t}{M_\infty}$ is the ratio of the mass uptake at time t versus the mass uptake at equilibrium, L is the membrane thickness and ierfc is the integral of the error function. At even shorter experimental times Equation 23 may be approximated by the following expression:

$$\frac{M_t}{M_\infty} = \frac{8}{\pi^{\frac{1}{2}}} \left(\frac{Dt}{L^2} \right)^{\frac{1}{2}} \quad (24)$$

Values of $\frac{M_t}{M_\infty}$ can be obtained experimentally and plotted versus \sqrt{t}/L allowing the diffusion coefficient to be determined from the gradient of the curve. A typical curve that obeys Fick's law of diffusion is shown in Figure 1.10.²⁸

Reactive dyeing involves the diffusion of a dye from an aqueous dye bath into the bulk of a textile fiber. In reactive dyeing, the dye molecules react with functional groups of the polymer hence; reactive dyeing is an interesting example of a diffusion-reaction process. The diffusion coefficient of the diffusing dye molecules is not only dependent on the properties of the material, but it is also affected by the consumption of dye molecules as they react with functional groups or ionized sites. Assuming that diffusion takes place in one dimension within an infinite fiber, the form of Fick's law stated in Equation 16 may be used to describe the diffusion of the dye molecules. If there is an excess of reactive sites within the polymer, the chemical reaction maybe assumed to be a first-order reaction. Therefore, Equation 16 becomes:²⁶

$$\frac{dc}{dt} = D \left(\frac{d^2c}{dx^2} \right) - kC_s \quad (25)$$

where k is the first order rate constant and C_s is the surface concentration of the dye. If Kt is small Equation 25 becomes:²⁶

$$\frac{dc}{dt} = C^*(Dk)^{\frac{1}{2}} \quad (26)$$

where C^* is the surface saturation concentration of the dye molecules.

Diffusion through polymers is influenced by the temperature of the system as well as polymer morphology such as crystallinity or the presence of crosslinks. However, there is another feature of polymers that influences diffusion, the polymer free volume. As described previously, the polymer free volume is a consequence of the long randomly coiled nature of the polymer chains which causes a volume difference between the space they occupy and the space that they traverse. It has been demonstrated that temperature affects the magnitude of the free volume which is also influenced by the motion of polymer chain segments. Until now, the Fickian behavior of a diffusing species within a polymer has been considered. However, free volume theories of diffusion have been developed to accurately predict the self-diffusion properties of a polymer.

We will introduce the free-volume theory of diffusion by considering a simple jump diffusion model. The motion of a single solute molecule from one region of the polymer to an adjacent location depends on the presence of a free volume void large enough to accommodate the solute molecule. This is the theory behind the free volume model of diffusion developed by Turnbull and Cohen in 1959 for hard-sphere molecules that form idealized liquids and amorphous glasses, and serves the foundation for more complicated free-volume models of diffusion.⁴⁴ A distribution function was developed which states that the diffusion coefficient is dependent on the probability of forming a critical free volume void in an adjacent location that is large enough to accommodate a small solute molecule, following:^{26, 44}

$$D = u \exp\left(\frac{-\gamma V_*}{V_f}\right) \quad (27)$$

where D is the diffusion coefficient, γ is a correction factor between 0.5 and 1 to account for free volume void overlap, and V_* is the volume of a critical free volume void. It is important to note that an activation energy is not required to initiate the re-distribution of the polymer free volume.

Equation 27 only considers the motion of solute molecules into a sufficiently large free volume voids however, it is also possible that if the void is large enough, a thermally activated polymer chain segment may change conformation and occupy the free-volume void. This alters the diffusion coefficient by preventing the motion and occupation of the free volume void by the diffusing species. Therefore, polymer chain segment motion is accounted for in the following expression:²⁸

$$D = D_0 \exp\left(\frac{-\gamma(\omega_1 V_1^* + \omega_2 \xi V_2^*)}{V_{FH}}\right) \quad (28)$$

where V_1^* and V_2^* are the critical free volume voids required to accommodate components 1 and 2 respectively, ω_1 and ω_2 are the number of moles of components 1 and 2, $\xi = \frac{V_1^*}{V_2^*}$ and V_{FH} is the specific free volume of the polymer which is the difference between the specific volume of the polymer and the occupied volume. As a suggestion, the occupied volume may be calculated by group contribution methods such as the Van der Waals volume.⁴⁵

The most dramatic changes in the diffusion coefficient of small molecules through a polymer have been observed at T_g .⁴⁶ Below this temperature, the diffusion coefficient is

greatly reduced however at T_g ; studies have shown that there is a sharp increase in the diffusion coefficient. This is attributed to the temperature dependent increase in free volume and re-distribution as larger polymer chain segments are able to move and form sufficient voids to accommodate the motion of diffusing molecules.

1.3 VAPOR PHASE MODIFICATION OF POLYMERS

1.3.1 Hybrid Organic-Inorganic materials

A hybrid organic-inorganic material is a material that incorporates both organic and inorganic material properties blended together.⁴⁷⁻⁴⁸ Therefore, a unique feature of hybrid materials is the formation of a material that is neither purely organic nor inorganic. Hybrid organic-inorganic materials can be distinguished between each other in terms of the interaction between the organic and inorganic component. For example, weak interactions such as hydrogen bonding, Van der Waals forces or weak electrostatic forces or strong interactions such as covalent bonds.^{47, 48, 51} One question that arises is what is the difference between composites and hybrids? On the macroscale, an organic-inorganic composite consists of a discrete inorganic material, which typically provides mechanical strength, distributed in a flexible organic medium which bonds the inorganic material together.^{6, 49} In this type of composite, there is a mechanical difference between the organic and inorganic component which means that the mechanical strength is dependent on good interfacial bonding between the individual components.^{49- 50} In comparison, hybrid materials are mixed together at the molecular scale and as we go down in scale from macroscale composites to hybrid materials, the homogeneity of the mixed components increases.^{47, 51} While there may

not be a definitive difference between hybrid materials and nano-composites, there may be a point at which a hybrid material transitions to a nano-composite since one of the components, either the organic or inorganic component, may be in the appropriate size range which is typically 1-100nm.^{47, 52}

Due to the increased homogeneity afforded by hybrid materials, one of their key benefits is overcoming the mechanical property mismatch that is typical of traditional composite materials.⁴⁷ A further benefit is the development of multifunctional materials by incorporation of inorganic material properties such as: excellent thermal stability, high dielectric constants, low permeability's, photocatalytic behavior and chemical resistance, without compromise to the attractive properties of organic materials such as flexibility and ease of form.⁶⁻¹⁰ Since the composition of the hybrid material can be controlled at the atomic scale, hybrid materials afford the opportunity to tailor the properties of a material for a specific application.

Figure 1.11 analyzes the number of publications based on hybrid organic-inorganic materials over a 25 year period. It is clear that the most productive years for hybrid-materials development was between the years 2008 and 2012. It is not clear why productivity dropped after 2012 however, it may be related to the necessity for the development of new techniques to form hybrid materials. As can be seen in Figure 1.11, the most widely used and well understood process for forming hybrid materials is the sol-gel process.^{50, 51, 53} The sol-gel process is a wet chemical technique which forms a network gel of inorganic particles from a sol, which is typically a solution of colloid particles.^{47, 54} A historical example of a sol-gel

process is the formation of silica via the hydrolysis of silicon alkoxide.⁵⁴ The hydrated silica molecules are able to interact with each other and form a sol via a polycondensation reaction. Initially, the solution has a low viscosity and is capable of diffusing into porous substrates such as textiles.^{9, 55} Over time, the solution becomes more viscous as more silica molecules link together which forms the gel component of the process. The sol is allowed to solidify within the substrate and residual liquid is removed from the substrate via a heat treatment.

In comparison, vapor phase techniques such as atomic layer deposition (ALD) make up only 1% of the literature based on hybrid organic-inorganic material formation. ALD is a unique processing for forming a broad range of nanoscale films on a surface by sequential exposures of an organometallic precursor and a co-reacting vapor species such as water. The principle of ALD growth is based on the cycling of organometallic precursor and co-reactant vapor exposures separated by an inert gas purge step. The corresponding self-limiting chemical reactions result in atomic scale precision of the pinhole free, conformal coatings. As a result of the pin-hole free nature of ALD films, the process has been widely adopted by the microelectronics industry to form high k dielectric films on the transistors of microchips.⁵⁶⁻⁶⁰ The saturation and self-limiting behavior of the chemical reactions on the surface of a substrate afford the opportunity to deposit inorganic films on both planar and complex surfaces consequently; ALD has been explored on polymer substrates such as polymer films and textile fibers.⁶¹⁻⁷⁶ The research exploring ALD on polymers lead to the discovery of a hybrid organic-inorganic coating on certain polymer chemistries affording the opportunity to use ALD as a unique hybrid material formation technique.

1.3.2 Characteristics of ALD

Atomic layer deposition (ALD) is a technique that is used to deposit nanoscale inorganic coatings onto the surface of a specific substrate with atomic scale precision. The atomic scale precision of the conformal, pinhole free coatings is achieved by ALD's unique attribute; a carefully chosen sequence of self-limiting surface reactions that typically involve two complementary precursor gases.^{1-3, 77} The first precursor is an organometallic vapour that is composed of an inorganic atom, such as Aluminum or Zinc, surrounded by organic ligands such as methyl or ethyl groups. The second precursor, also named the co-reactant, contains an oxygen source such as, water or ethylene glycol that is capable of undergoing a ligand exchange process. The precursor vapors are introduced to a surface individually in a sequential fashion to promote the formation of a monolayer therefore, a purge step is required to separate the dose of each precursor and prevent any unwanted reactions that could occur between them.

A traditional prerequisite for ALD is that the substrate must ideally have a high concentration of surface functional groups that are reactive towards the ALD precursors. When the first precursor gas (A) is introduced to the substrate, it will react with the surface functional groups until they have all been consumed leaving the surface covered with adsorbed molecules of A as shown in Figure 1.12. Any molecules of A that have not adsorbed to the surface will be removed from the system by the first purge step (P1) along with any reaction by-products. After (P1), the second precursor (B) is introduced to the system which reacts with (A) until all reactive sites have been consumed and the surface is

terminated with molecules of (B). This is followed by another purge (P2) which removes the reaction by-products and any un-reacted molecules of (B). The second step of the cycle permits the repetition of the ALD sequence since (B) leaves the surface terminated with reactive surface sites that can be used to facilitate a further cycle of self-limiting reactions. Consequently, through the use of sequential, self-limiting surface reactions it is possible to build up an inorganic coating of a desired thickness with atomic scale precision.

The above sequence describes one cycle of an ALD process and it can be summarized by the following expression, A/P1/B/P2. This is called the dose sequence which indicates the dose time of each precursor and purge step. The dose times of each step in the ALD sequence can be optimized, based on the geometry, size and gas flow characteristics of the ALD reactor, to promote a fully saturated surface and sufficient exposure time that will correspond to one sub-atomic layer of growth per ALD cycle (GPC). At the laboratory scale, the dose time of each precursor is typically on the order of a tenth of a second while the purge steps are on the order of seconds for example, 0.2/30/0.2/45 therefore, one ALD cycle can be completed within minutes.

In addition to precursor dose and surface exposure times, the GPC of the ALD process can also be optimized for a range of temperatures which is aptly named the ALD window. The ALD window encompasses a range of temperatures that consistently promote one sub atomic GPC as shown in Figure 1.13. If the ALD process is operated outside of the ALD window, uneven growth can occur as a result of precursor condensation at low temperatures or precursor decomposition and desorption at high temperatures. The ALD

window is important for ALD on polymers when one considers the thermally activated chemical reactions between precursors and the variety of decomposition temperatures possessed by different polymer chemistries. This made the development of low temperature ALD processes particularly important.^{4, 67, 73, 78-86}

1.3.3 ALD on polymers

Multiple ALD cycles can produce thin film coatings on a broad range of polymers as shown in Figure 1.14.^{67,68} However, the coating morphology depends strongly on the polymer composition and the reaction mechanism between the polymer and ALD precursors. There are two main types of nano-scale finish that can be formed on polymer fibres: 1) Uniform, conformal coatings with an abrupt interface between the inorganic and fibre surface, and 2) hybrid organic-inorganic finishes. The former, follows the principles of ALD, whereas the latter results from the direct reaction or penetration of the ALD vapour precursors and the polymer.

Firstly, polymers such as polyolefins typically do not possess the functionality to react with organometallic precursors. However, precursor molecules can react with potential nucleation sites such as; chain ends, chain defects, impurities from the polymerization process and oxidation products from melt processing or storage. During the first half reaction of an ALD process on polyolefins such as PP, organometallic precursor penetrates and diffuses into the polymer subsurface. During the second half reaction, the co-reactant such as water reacts with the absorbed precursor creating nucleation sites of alumina. These grow

and coalesce into a film via a Volmer-Weber growth mechanism with increasing number of ALD cycles.^{4, 11, 67}

Polymers, such as cotton, PVOH and PLA, form conformal inorganic coatings on their surfaces due to a high concentration of surface functional groups that are reactive towards organometallic precursors. Since organometallic precursors react favorably with hydroxylated surfaces and the reactive surface group density of these polymers is high, there is minimal diffusion of precursor into the subsurface of the polymer.^{4, 64, 67}

Alternatively, metallo-organic precursor exposure to polymers that contain functional groups, such as the amide group in PA-6 and carbonyl group in PET, have shown to form a unique organic-inorganic hybrid interface.^{4, 14} Analysis has shown that organometallic precursors penetrate the sub-surface of the polymer and directly react with the polymer backbone. With ALD processing, a graded finish is observed that is dependent on the diffusion of ALD precursors into the polymer sub-surface and the chemical reactions with the functional groups of the polymer.⁴ After a certain incubation period in which the hybrid layer is promoted, additional ALD cycling results in conformal inorganic growth on the surface of the polymer, following a typical ALD process.⁴ Processing by a single precursor exposure cycle has also been shown to result in an ungraded hybrid modification after diffusion of precursors into the subsurface of the polymer.¹⁸

Additional factors that may influence the infiltration of organometallic precursors into the subsurface of the polymer, includes the temperature of the process and the presence of pre-absorbed water within the polymer matrix.¹⁸ With respect to water absorption,

organometallic precursors will preferentially react with the hydroxyl group of the water molecule which may affect successive diffusion of precursor molecules and the saturation behavior of the polymer. The chemical reaction between pre-absorbed water and organometallic precursor molecules could form a sub-surface diffusion barrier against consecutive exposures.¹⁸ Furthermore, water molecules or unreacted monomer, evaporating from the sub-surface of the polymer, may diffuse against the concentration gradient of the organometallic precursor within the polymer matrix. In theory this could impede the diffusion and mass uptake of precursor molecules, especially during the first few exposures.

With respect to temperature, the Arrhenius relationship predicts that an increase in temperature increases the diffusion coefficient of the respective vapor. Additionally, an increase in temperature also leads to polymer expansion hence, increasing the free volume of the polymer matrix. For non-reactive polyolefins, studies have shown that TMA mass uptake scales with increased diffusion coefficients and polymer free volumes as a result of higher reaction temperatures.^{4,11,67} However; in an ALD like process on reactive polymers, one must consider the effect of temperature on the extent of the chemical reaction. Previous research has indicated that thinner films form at higher temperatures on polymers such as PA-6⁸⁷ due to a more complete reaction between organometallic precursors and the polymer backbone, creating a barrier against diffusion of successive precursor doses.

As described above, analysis has shown that organometallic precursors penetrate the sub-surface of the polymers and react to produce a graded finish. The control over this finish is dependent on a combination of the rates of diffusion and reaction between the ALD

precursors and polymer sub-surface and the chemical reactions with the functional groups of the polymer. These results have inspired adaptations to the ALD process which extend the precursor exposure conditions to exploit the infiltration of organometallic precursors into the polymer subsurface.

1.3.4 Comparative ALD processes

Examples of other vapor phase techniques which follow the principles of ALD Processes include multiple pulse infiltration (MPI)^{16 15}, sequential infiltration synthesis (SIS)¹⁷ and sequential vapor infiltration (SVI).^{18 19 20} Each technique varies in the exposure timing and sequencing and thus results in different material growth behavior. For example, sequential vapor infiltration (SVI) processing is defined by a single elongated exposure of a precursor, followed only then by exposure of the second reactant.¹⁸ Unlike ALD, sequential cycling of the precursor and reactant are not performed in SVI. Thus, the SVI process allows for growth of the hybrid layer into the polymer surface in a single exposure cycle. As a result, no graded interface is observed on the surface of the polymer.¹⁸

Like ALD, the SVI process can be used to form inorganic coatings on textile fibers and nonwovens. When the first precursor gas (A) is introduced to the reaction chamber, like ALD, it will react with the surface functional groups of the substrate. However, during the SVI process (A) is held inside the reaction chamber for an extended period of time. This allows molecules of (A) to penetrate the subsurface of the polymer and seek out all the potential reactive sites thus, leaving the internal sub-surface terminated with adsorbed molecules of (A). Any molecules of (A) that have not reacted are removed from the system

by a purge step (P1). After (P1), the second precursor (B) is introduced to the system and is held inside the reaction chamber for an extended period of time which allows molecules of (B) to seek out and react with adsorbed molecules of (A) until all reactive sites have been consumed. This is followed by another purge (P2) which removes the reaction by-products and any un-reacted molecules of (B). Therefore, the typical dose sequence of the ALD process, (A/P1/B/P2), has been subtly modified to (A/H/P1) \times N (B/H/P2) \times N as shown in Figure 1.15.¹⁸ The SVI technique has been used to form high surface area ceramics from a PET fabric.¹⁹ The infiltration of TMA into the PET fabric formed alumina coatings within the internal porous networks of the polymer. The polymer component was burnt out leaving a pure ceramic that mimicked the internal surface area of the PET polymer. The surface area was dependent on the number of SVI cycles and the porosity of the polymer.

In comparison, multiple pulsed infiltration utilizes a single precursor exposure held for a period of time, followed by exposure of a second reactant in the same manner. Like ALD, multiple cycles are employed, but the hold period accentuates any reaction between the precursor and the polymer to form a hybrid material as long as the precursor is not fully consumed.^{15, 16} Therefore the characteristic dose sequence of MPI may be summarized by (A/H/P1/B/H/P2) \times N. This particular technique has been applied to mechanically strengthen protein-based fibers such as spider silk and collagen through an internal modification.¹⁵ Finally, during an SIS process the first reaction promotes the nucleation of the second reaction sequence. Therefore, the dose sequence may be summarized by A/P1/B/(C/P1/D) \times N.¹⁷ Conversely to SVI and MPI, increased exposure in SIS is established by extended doses of each precursor rather than the incorporation of a hold step. This

particular technique has been applied to selective reaction of a block co-polymer system as a new technique for nanopatterning.¹⁷

1.3.5 Potential Applications

As described above, inorganic coatings such as alumina, zinc oxide and titania have been deposited onto the surface of textile materials such as PP, cotton and PA-6 via vapor phase processes such as ALD and infiltration processes. One of the main benefits of these processes versus alternative inorganic modification techniques such as chemical vapor deposition, sol-gel, and dip coating is the conformal, pinhole free nature of the ALD coatings that is difficult to achieve with the inorganic modification techniques mentioned above.

A phenomenon related to various inorganic modification techniques is photocatalysis. This is an extensive area of research due to the numerous applications that take advantage of photocatalytic chemical reactions such as the detoxification of gases, decontamination of water, denaturing of viruses and bacteria and self-cleaning surfaces.⁸⁸⁻⁹⁰ Titania is one of the most widely used semiconducting photocatalysts due to its environmental compatibility and band gap energy equivalent to the energy of UVA photons from terrestrial radiation. Furthermore, a titania treated cement capable of decomposing hydrocarbon smog was rated one of the top 50 inventions by Time's Magazine in 2008.^{88, 91}

An area of interest within the textile industry that may benefit from photocatalysis is active filtration. In active filtration, fabrics are treated with titania which absorb UVA photons and generate electron-hole pairs on the surface of the semiconductor as shown in

Figure 1.16. The electron-hole pairs can be used to reduce or oxidize water vapor and oxygen molecules adsorbed to the surface of the filter which forms hydroxyl and oxygen radicals that can be used in secondary chemical reactions to purify contaminated water and decompose organic liquids or hydrocarbon gas.⁸⁸ Since titania is a catalyst, it only facilitates the chemical reactions therefore; no material from the photocatalytic coating is lost. However, the photocatalytic efficiency may degrade if the coating is not uniform or durable. Therefore, ALD may be a suitable solution for improving the efficiency of existing technologies as a result of the pinhole free nature of the inorganic coatings. The development of photocatalytic filters may allow us to fulfill the environmental aspect of sustainability within many textile manufacturing processes. For example, the development of filters that breaks down dye residues in water used during the dyeing process.

An alternative application includes the use of inorganic coatings on battery separators to enhance electrolyte uptake and prevent shrinkage of the separator at high temperatures.⁹² The shrinkage of the polymer membrane is caused by a hysteresis effect that is related to the thermal history of the polymer during the manufacturing process and subsequent storage.³³ Shrinkage of the separator membrane leads to a short circuit of the battery since it is no longer preventing contact between the electrodes. Compared with dip coating and other sol gel methods, ALD could provide an effective alternative to coating PP battery separators with durable, conformal, defect free inorganic coatings that possesses good thermal properties and chemical resistance such as alumina. Moreover, if the surface energy changes associated with ALD coatings promotes improved electrolyte uptake, it may be possible to incorporate more environmentally friendly, solvent free electrolytes, such as room

temperature ionic liquids and aqueous electrolytes, in various energy storage technologies.^{93,}

94

As stated previously, vapor phase techniques have been used to strengthen biological fibers such as regenerated spider silk.¹⁵ This is significant work since historically it has been difficult for researchers to replicate the true strength of natural spider silk due to factors such as, the use of caustic uncharacteristic solvents,⁹⁵ difficulties expressing the gene sequence and spinning the precise pattern of amino acid residues within the primary structure of the fiber.^{95 -98} Typically, man-made fibers are either high performance high tensile strength fibers with lower elongations at break or fibers that have large elongations at break and lower tensile strengths.³³ Therefore, a further application of SVI is the strengthening of textile fibers via SVI. Furthermore, the SVI technique may afford the opportunity to replicate the high toughness, high strength nature of spider silk fibers in man-made synthetic fibers. The infiltration and intrachain covalent bonding of metallo-organic precursor molecules to function groups within the sub surface of the polymer could prove to improve the ultimate strength and increase the elongation at break of synthetic fibers by acting as a mechanical buffer layer. A potential benefit of ALD or SVI strengthened fabrics is the opportunity to reduce the basis weight of the material to achieve the equivalent mechanical strength.

1.3.6 Roll-to-roll processes

As described in Section 1.3.2, during a typical ALD process, a single reaction chamber is filled with an organometallic precursor to saturate the reactive surface sites of a particular substrate which is followed by the introduction of a suitable co-reactant. Lengthy

purge steps are required to remove excess precursor and by-products formed during the organometallic precursor and co-reactant exposure steps respectively. Since the characteristic dosing times of the organometallic precursor and co-reactant exposure steps are relatively short and the chemical reactions are completed quickly, the purge step has generally prevented extensive commercialization of the ALD process. However, as described previously, due to the quality, pin-hole free nature of ALD films, the process has been widely adopted by the microelectronics industry to form high k dielectric films on the transistors of microchips.

An area of industry that ALD has found its inadequacy is within the textile and polymer film industries. The mismatch between processing times, since textile fibers and fabrics can be produced at thousands of meters per minute (mpm), creates a significant engineering challenge that historically has made it difficult to envision ALD as a practical surface modification technique. However, the promising and exciting results from studies exploring the surface and sub-surface modification of polymers makes the vision of ALD, as a viable surface modification technique, more worthwhile and realistic. This has inspired the investigation of ALD roll-to-roll processes with success. Infact, many of the concepts are as attractive in their apparent simplicity as the ALD process itself and most of the designs are based on the main characteristics of the ALD process.⁹⁹ Therefore, one can imagine separate chambers that contain the necessary vapors to form a metal oxide coating on a fabric or polymer film via the ALD process. A series of rollers that allow the flexible material to move back and forth between each chamber promotes the growth of an inorganic film with a desired thickness that is dependent on the number of passes made between each chamber.

This is the concept behind the roll-to-roll process designed by lotusat as shown in Figure 1.17.¹⁰⁰

This concept could easily be extended to the SVI process which may afford the opportunity to cut down on processing time by the single passing of the fabric through each chamber rather than multiple passes that is characteristic of the ALD process. Either ALD or SVI techniques are viable options for modifying continuous quantities of flexible substrates and the chosen technique should be based on the final properties most desired and whether bulk properties or surface properties are more important for the intended application. Ultimately, through studies that are dedicated to better understand the unique chemical reactions and growth mechanisms of ALD and infiltration processes on polymers and the development of atmospheric ALD¹⁰¹⁻¹⁰⁵ or SVI techniques, roll-to-roll processes stand a greater chance of realizing wide spread commercialization in the future.

Chapter 1 Figures:

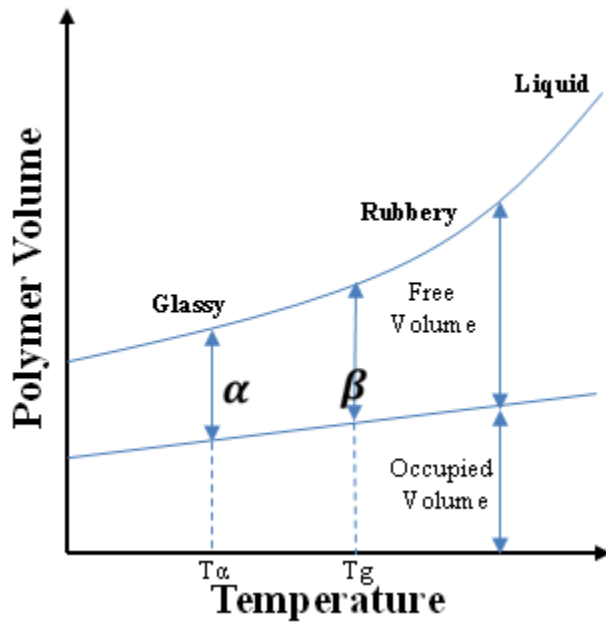


Figure 1.1. Schematic diagram indicating volume changes that occur in polymers as temperature increases. The region labelled α represents the polymer free volume below the glass transition temperature while β corresponds to the polymer free volume at T_g .¹⁴

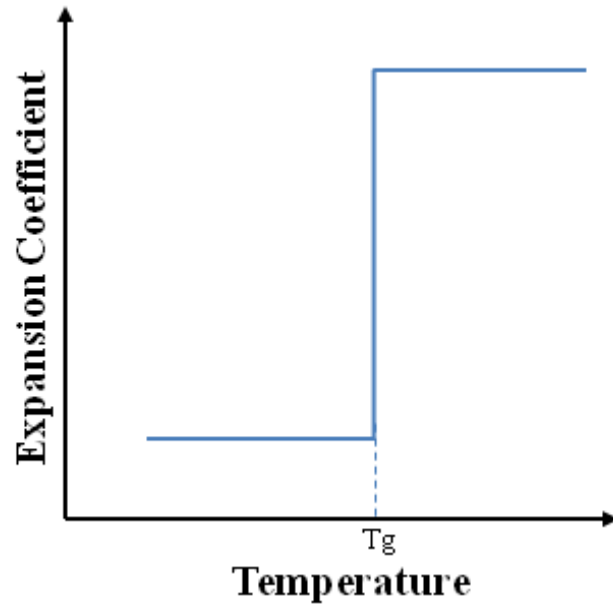


Figure 1.2. Diagrammatic representation of the temperature dependence of the expansion coefficient.

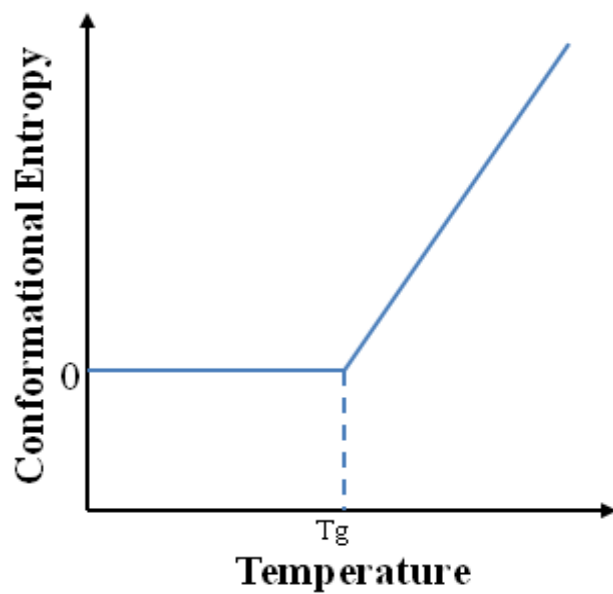


Figure 1.3. Conformation entropy as a function of temperature as stated by the Gibbs and DiMarzio thermodynamic theory of T_g .³⁰

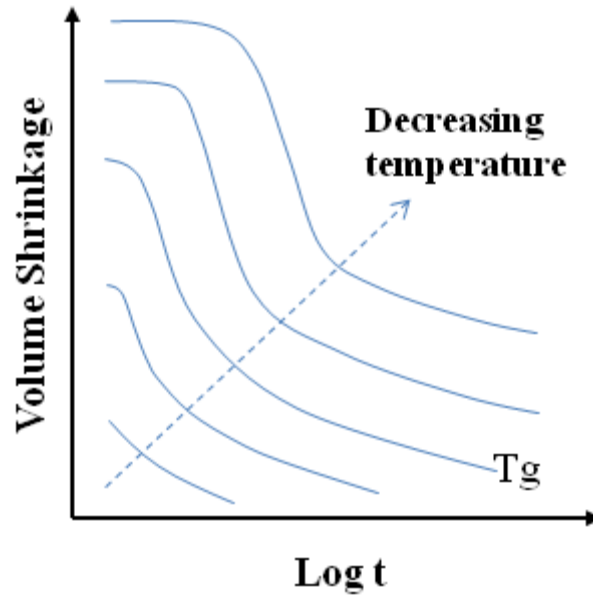


Figure 1.4. Effect of storage temperatures above and below the glass transition temperature on the volume of a polymer. As the diagram indicates, at higher storage temperatures polymer chains are able to relax quicker which corresponds to volume shrinkage.³³

Table 1.1. WLF equation constants and glass transition temperatures of a range of polymers.³⁶

Polymer	C_1 (K)	C_2 (K)	T_g (K)
Polyisobutylene	16.6	104	202
Natural rubber	16.7	53.6	200
Polyurethane	15.6	32.6	238
Polystyrene	14.5	50.4	373
Poly(ethyl methacrylate)	17.6	65.5	335
Polyethylene	12.7	66.3	317
Atactic polypropylene	12.9	34.7	262

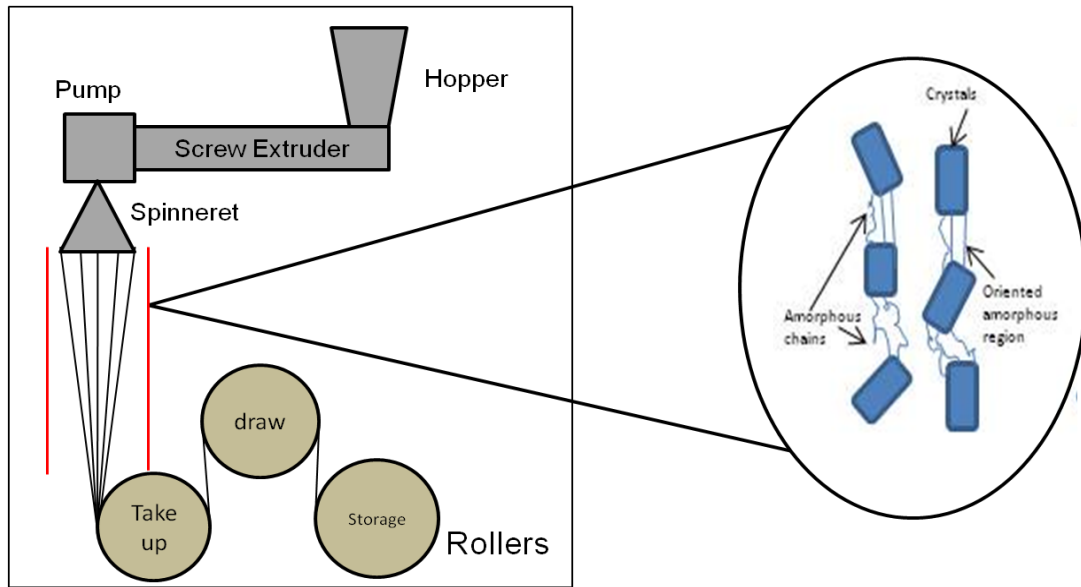


Figure 1.5. Diagrammatic representation of the melt spinning process adapted from Billmeyer.³⁷

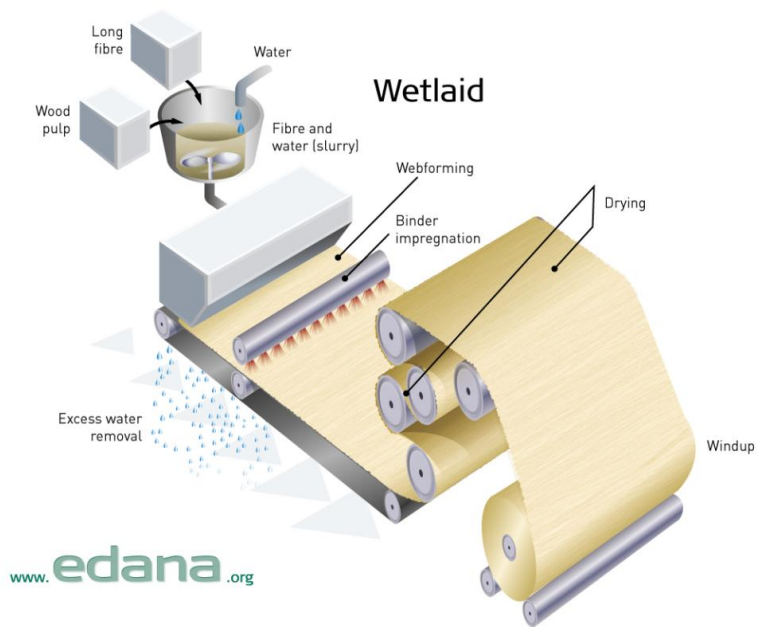
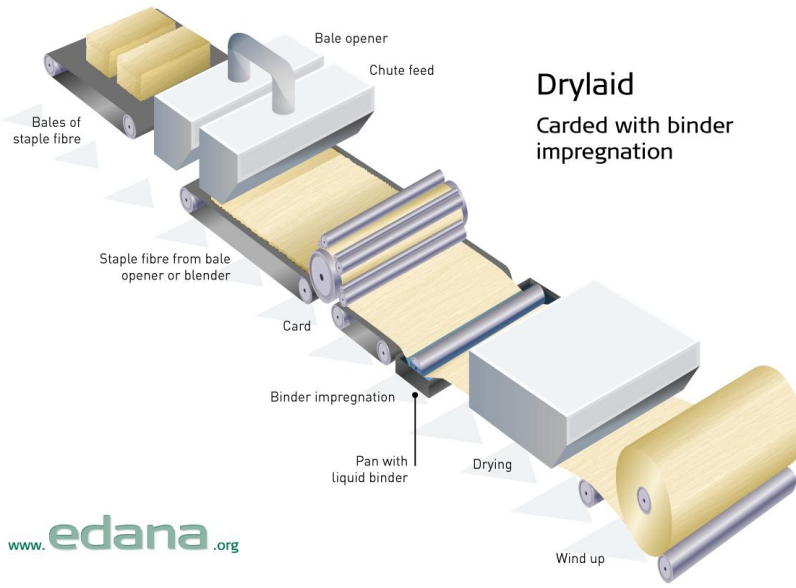


Figure 1.6. Diagrams demonstrating the wet lay and dry lay processes. Figures obtained from edana.³⁹

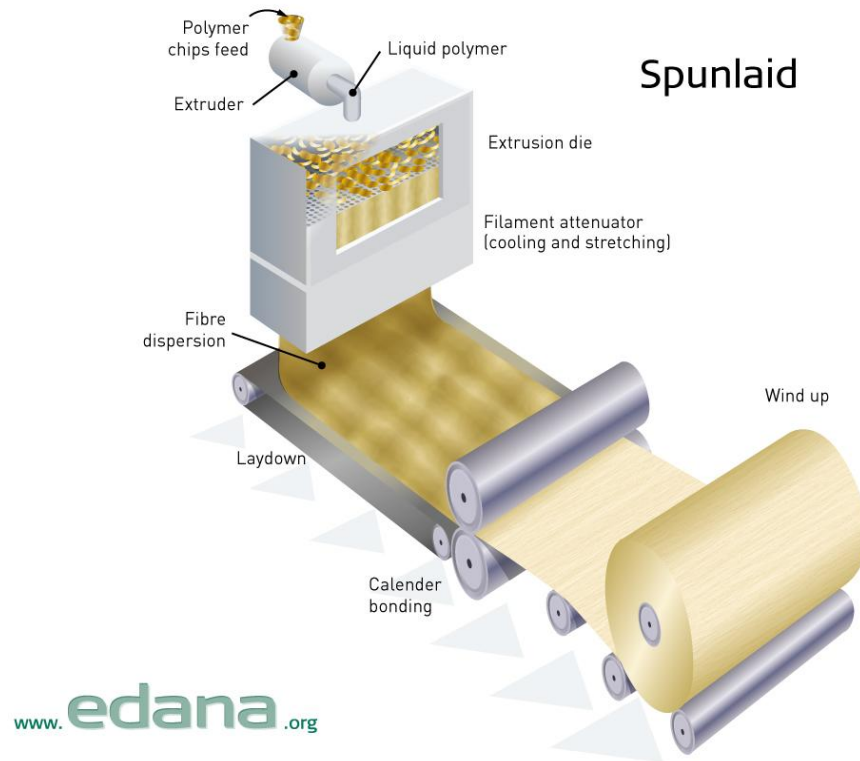


Figure 1.7. Diagram representing the meltblown and spunbond (spunlaid) processes. Figure obtained from edana.³⁹

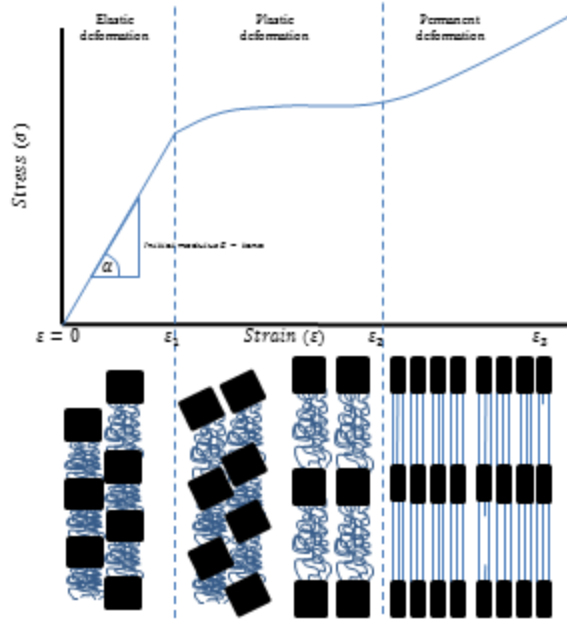


Figure 1.8. Diagrammatic representation of a typical stress-strain curve of a textile fiber highlighting the elastic, plastic and permanent deformation regions. Below the stress-strain curve, a series of diagrams indicates the effect that an applied load has on the structure of the polymer which corresponds to the stress-strain behaviour observed in the curve.

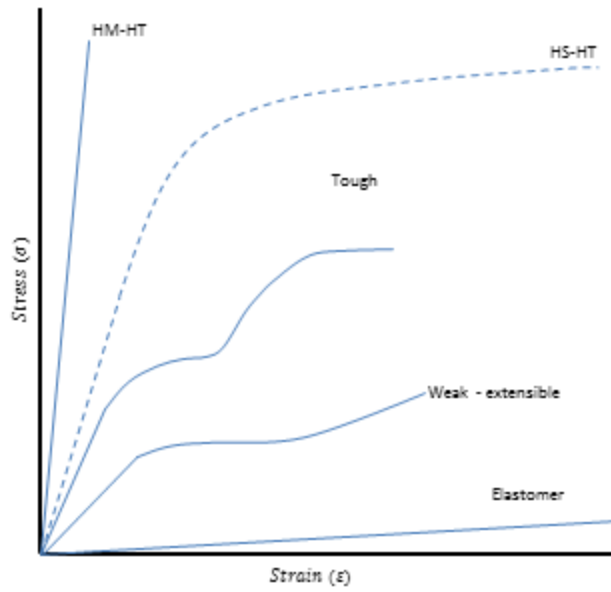


Figure 1.9. Stress-strain curve indicating the characteristic behaviour of textile fibers during a tensile test.⁴³

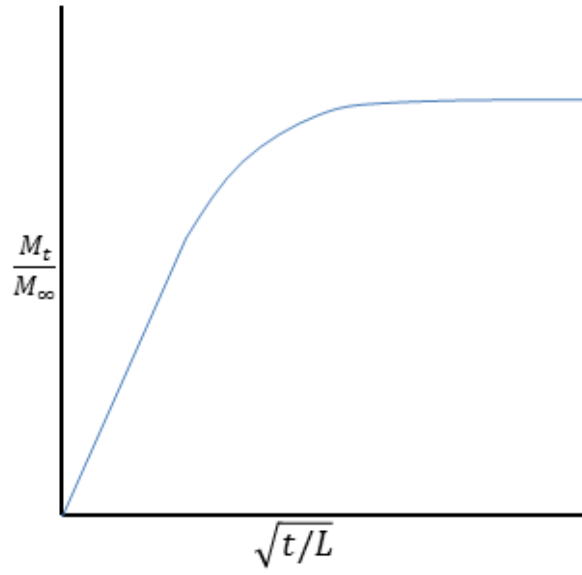


Figure 1.10. Fractional mass gain as a function of time and membrane thickness.²⁸

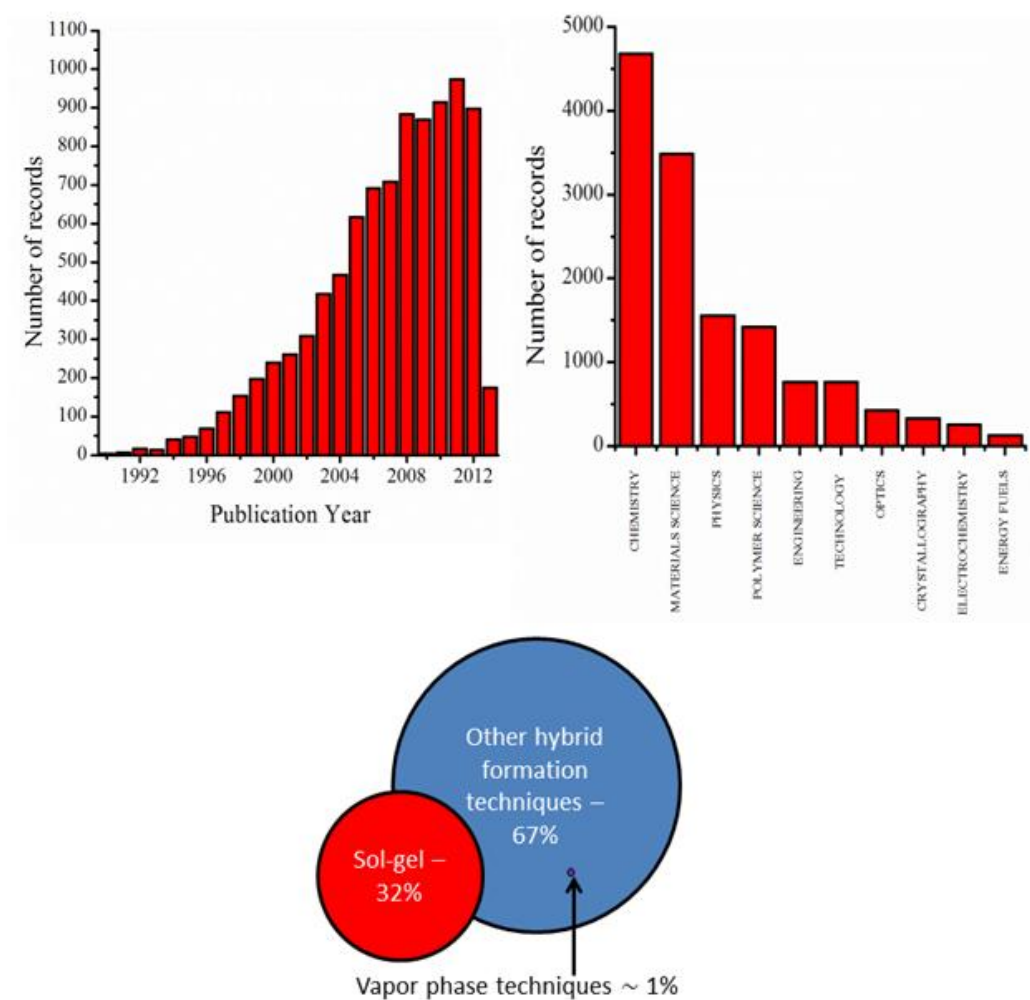


Figure 1.11. Analysis of publications based on hybrid organic-inorganic materials. The data was obtained from a literature search using the Web of Science search tool.

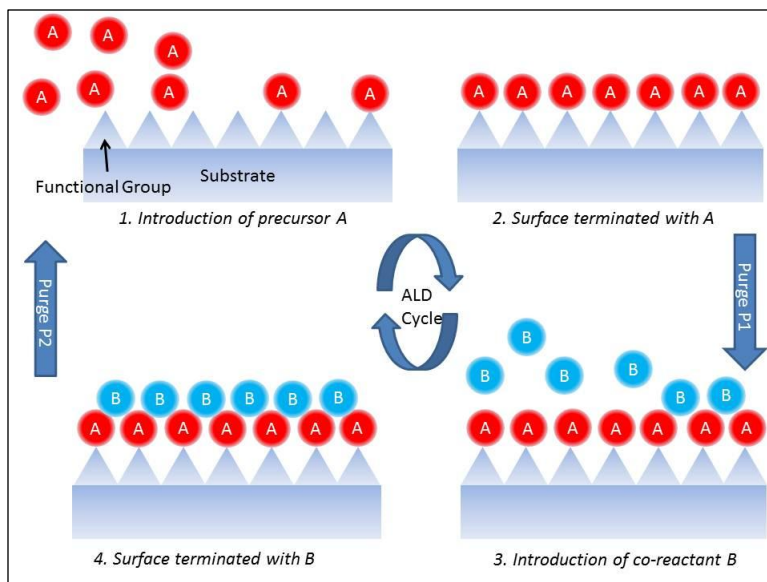


Figure 1.12. Diagram demonstrating the dosing sequence of an organometallic precursor and co-reactant of a typical ALD process

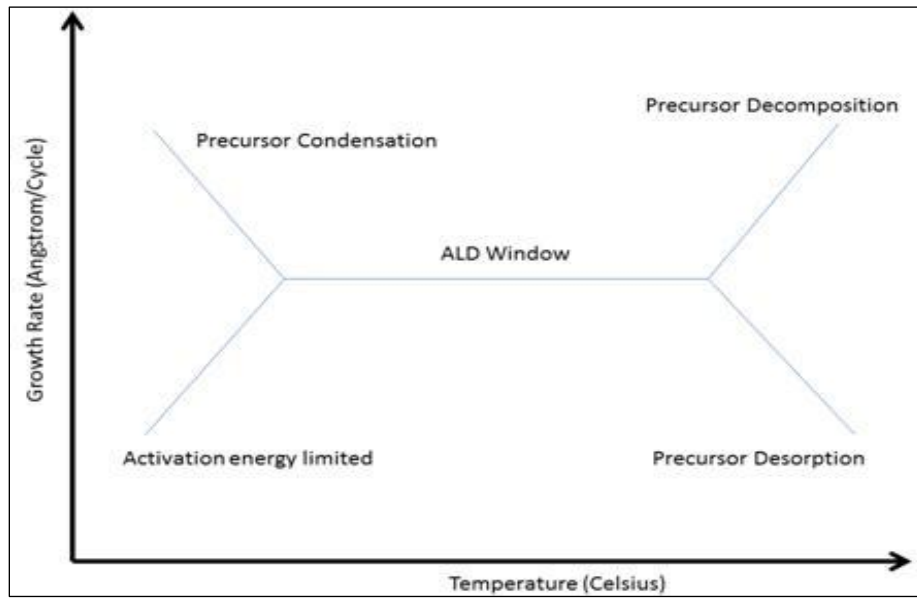


Figure 1.13. Diagrammatic representation of the ALD window indicating growth rate as a function of temperature.

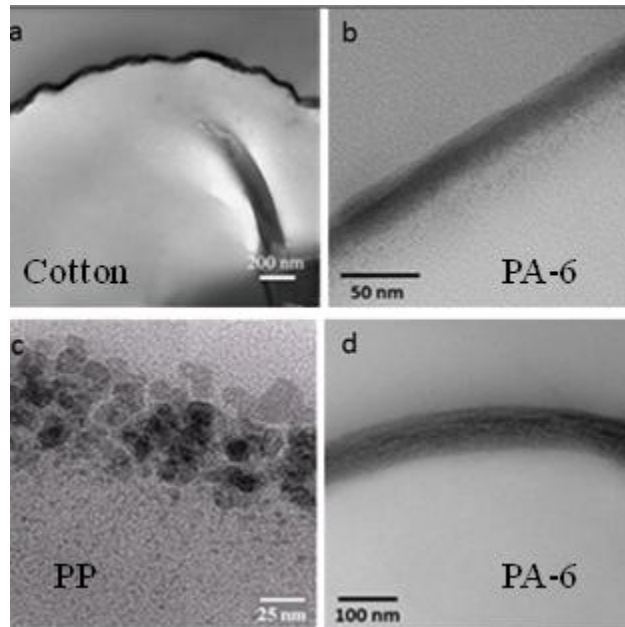


Figure 1.14. TEM images of various vapor deposition compositions. a) indicates a conformal coating formed on cellulose, b) indicates a hybrid organic in-organic layer formed on PA-6 with a graded sub-surface composition, c) shows the island growth and nucleation associated with vapour deposition on PP fibers and finally d) shows a hybrid organic-inorganic layer formed on PA-6 via SVI with an ungraded finish

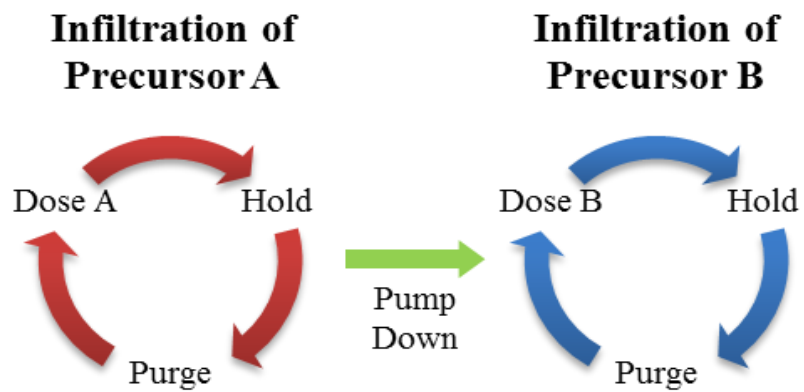


Figure 1.15. Diagram demonstrating the dosing sequence of an organometallic precursor and co-reactant of a typical SVI process.¹⁸

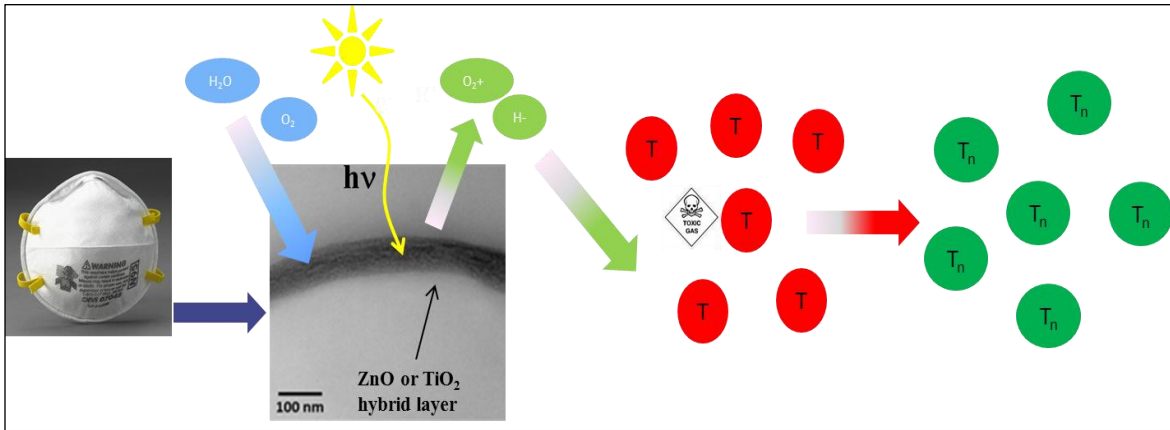


Figure 1.16. Diagram describing the photocatalytic principle within the active filtration of a toxic gas

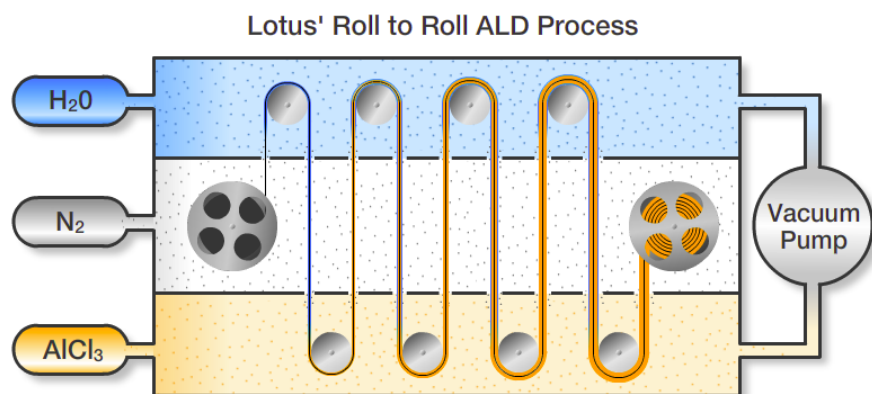


Figure 1.17. Lotusat roll-to-roll ALD process.¹⁰⁰

Chapter 1 references:

1. George, S. M., Atomic Layer Deposition: An Overview. *Chemical Reviews* 2010, 110 (1), 111-131.
2. Parsons, G. N.; George, S. M.; Knez, M., Progress and future directions for atomic layer deposition and ALD-based chemistry. *Mrs Bulletin* 2011, 36 (11), 865-871.
3. Puurunen, R. L., Surface chemistry of atomic layer deposition: A case study for the trimethylaluminum/water process. *Journal of Applied Physics* 2005, 97 (12).
4. Spagnola, J. C.; Gong, B.; Arvidson, S. A.; Jur, J. S.; Khan, S. A.; Parsons, G. N., Surface and sub-surface reactions during low temperature aluminium oxide atomic layer deposition on fiber-forming polymers. *Journal of Materials Chemistry* 2010, 20 (20), 4213-4222.
5. Peng, Q.; Tseng, Y. C.; Darling, S. B.; Elam, J. W., Nanoscopic Patterned Materials with Tunable Dimensions via Atomic Layer Deposition on Block Copolymers. *Advanced Materials* 2010, 22 (45), 5129-+.
6. Pandey, S.; Mishra, S. B., Sol-gel derived organic-inorganic hybrid materials: synthesis, characterizations and applications. *Journal of Sol-Gel Science and Technology* 2011, 59 (1), 73-94.
7. Nicole, L.; Rozes, L.; Sanchez, C., Integrative Approaches to Hybrid Multifunctional Materials: From Multidisciplinary Research to Applied Technologies. *Advanced Materials* 2010, 22 (29), 3208-3214.
8. Judeinstein, P.; Sanchez, C., Hybrid organic-inorganic materials: A land of multi-disciplinarity. *Journal of Materials Chemistry* 1996, 6 (4), 511-525.
9. Alongi, J.; Malucelli, G., State of the art and perspectives on sol-gel derived hybrid architectures for flame retardancy of textiles. *Journal of Materials Chemistry* 2012, 22 (41), 21805-21809.
10. Mao, Q. H.; Fell, C. J.; Scully, A. D., Self-assembled nano-phase particles for enhanced oxygen barrier coatings on polymeric materials. *Progress in Organic Coatings* 2013, 76 (1), 51-59.
11. Wilson, C. A.; Grubbs, R. K.; George, S. M., Nucleation and growth during Al₂O₃ atomic layer deposition on polymers. *Chemistry of Materials* 2005, 17 (23), 5625-5634.

12. Peng, Q.; Sun, X.-Y.; Spagnola, J. C.; Hyde, G. K.; Spontak, R. J.; Parsons, G. N., Atomic layer deposition on electrospun polymer fibers as a direct route to Al₂O₃ microtubes with precise wall thickness control. *Nano Letters* 2007, 7 (3), 719-722.
13. Kaariainen, T. O.; Cameron, D. C.; Tanttari, M., Adhesion of Ti and TiC Coatings on PMMA Subject to Plasma Treatment: Effect of Intermediate Layers of Al₂O₃ and TiO₂ Deposited by Atomic Layer Deposition. *Plasma Processes and Polymers* 2009, 6 (10), 631-641.
14. Gong, B.; Parsons, G. N., Quantitative in situ infrared analysis of reactions between trimethylaluminum and polymers during Al₂O₃ atomic layer deposition. *Journal of Materials Chemistry* 2012, 22 (31), 15672-15682.
15. Lee, S. M.; Pippel, E.; Gosele, U.; Dresbach, C.; Qin, Y.; Chandran, C. V.; Brauniger, T.; Hause, G.; Knez, M., Greatly Increased Toughness of Infiltrated Spider Silk. *Science* 2009, 324 (5926), 488-492.
16. Lee, S. M.; Ischenko, V.; Pippel, E.; Masic, A.; Moutanabbir, O.; Fratzl, P.; Knez, M., An Alternative Route Towards Metal-Polymer Hybrid Materials Prepared by Vapor-Phase Processing. *Advanced Functional Materials* 2011, 21 (16), 3047-3055.
17. Peng, Q.; Tseng, Y. C.; Darling, S. B.; Elam, J. W., A Route to Nanoscopic Materials via Sequential Infiltration Synthesis on Block Copolymer Templates. *Acs Nano* 2011, 5 (6), 4600-4606.
18. Akyildiz, H. I.; Padbury, R. P.; Parsons, G. N.; Jur, J. S., Temperature and Exposure Dependence of Hybrid Organic-Inorganic Layer Formation by Sequential Vapor Infiltration into Polymer Fibers. *Langmuir* 2012, 28 (44), 15697-15704.
19. Gong, B.; Peng, Q.; Jur, J. S.; Devine, C. K.; Lee, K.; Parsons, G. N., Sequential Vapor Infiltration of Metal Oxides into Sacrificial Polyester Fibers: Shape Replication and Controlled Porosity of Microporous/Mesoporous Oxide Monoliths. *Chemistry of Materials* 2011, 23 (15), 3476-3485.
20. Gong, B.; Spagnola, J. C.; Parsons, G. N., Hydrophilic mechanical buffer layers and stable hydrophilic finishes on polydimethylsiloxane using combined sequential vapor infiltration and atomic/molecular layer deposition. *Journal of Vacuum Science & Technology A* 2012, 30 (1).
21. Elam, J. W.; Groner, M. D.; George, S. M., Viscous flow reactor with quartz crystal microbalance for thin film growth by atomic layer deposition. *Review of Scientific Instruments* 2002, 73 (8), 2981-2987.

22. Rocklein, M. N.; George, S. M., Temperature-induced apparent mass changes observed during quartz crystal microbalance measurements of atomic layer deposition. *Analytical Chemistry* 2003, 75 (19), 4975-4982.
23. Wind, R. A.; George, S. M., Quartz Crystal Microbalance Studies of Al₂O₃ Atomic Layer Deposition Using Trimethylaluminum and Water at 125 degrees C. *Journal of Physical Chemistry A* 2010, 114 (3), 1281-1289.
24. Knez, M., Diffusion phenomena in atomic layer deposition. *Semiconductor Science and Technology* 2012, 27 (7).
25. Sinha, A.; Hess, D. W.; Henderson, C. L., Transport behavior of atomic layer deposition precursors through polymer masking layers: Influence on area selective atomic layer deposition. *Journal of Vacuum Science & Technology B* 2007, 25 (5), 1721-1728.
26. Johnson, A., The theory of coloration of textiles. Second ed.; The Society of Dyers and Colorists: 1989.
27. Alan E. Tonelli, M. S., Polymers From the Inside Out: An Introduction to Macromolecules. Wiley: 2001.
28. P. Neogi, *Diffusion in Polymers*. New York : Marcel Dekker: 1996.
29. Norman G. MacCrum, C. P. B., Clive B. Bucknall, Principles of Polymer Engineering. Oxford University Press: 1997.
30. Gedde, U. W., Polymer Physics. Springer: 1995.
31. Gibbs, J. H.; Dimarzio, E. A., NATURE OF THE GLASS TRANSITION AND THE GLASSY STATE. *Journal of Chemical Physics* 1958, 28 (3), 373-383.
32. Kauzmann, W., THE NATURE OF THE GLASSY STATE AND THE BEHAVIOR OF LIQUIDS AT LOW TEMPERATURES. *Chemical Reviews* 1948, 43 (2), 219-256.
33. Jean-Pierre Pascault, H. S., Jacques Verdu, Roberto J. J. Williams, Thermosetting Polymers. CRC Press: 2002.
34. Frederick, B., Physical properties of polymers. Interscience Publishers: 1969.
35. Warner, S. B., Fiber science. Illustrated ed.; Prentice Hall PTR: 1995.
36. Mark, J. E., Physical properties of polymers handbook. Springer: 2007.

37. Billmeyer, F. W., TEXTBOOK OF POLYMER SCIENCE. Springer: 2007.
38. <http://www.inda.org/about-nonwovens/>].
39. <http://www.edana.org/discover-nonwovens/how-they're-made/formation>.
40. Pourdeyhimi, B.,
http://www.textileworld.com/Articles/2011/May/May_June_issue/Durable_Nonwovens.html.
2011.
41. <http://www.pgi-industrial-europe.com/en/apex-fabrics>.
42. <http://www.freudenberg-nw.com/en/Company/Brands/Pages/Evolon-Microfilament-Microfiber.aspx>.
43. William Ernest Morton, J. W. S. H., Physical Properties of Textile Fibres. Fourth ed.; Woodhead Publishing Limited: 2008.
44. Cohen, M. H.; Turnbull, D., MOLECULAR TRANSPORT IN LIQUIDS AND GLASSES. *Journal of Chemical Physics* 1959, 31 (5), 1164-1169.
45. Krevelen, D. W. v., Properties of Polymers: Their correlation with chemical structure; their numerical estimation and prediction from group contributions. Third ed.; Elsevier: 1990.
46. Vieth, W. R.; Laird, S. P., THE EFFECTS OF GLASSY MICROSTRUCTURE ON SMALL MOLECULE TRANSPORT IN AMORPHOUS POLY (ETHYLENE TEREPHTHALATE). *Journal of Membrane Science* 1992, 72 (2), 119-136.
47. Kickelbick, G., Hybrid materials : synthesis, characterization, and applications. Wiley: 2007.
48. Pedro Gómez-Romero, C. S., *Functional Hybrid Materials*. Weinheim : Wiley-VCH,: 2004.
49. Gao, Y. C., DEBONDING ALONG THE INTERFACE OF COMPOSITES. *Mechanics Research Communications* 1987, 14 (2), 67-72.
50. Sanchez, C.; Ribot, F.; Lebeau, B., Molecular design of hybrid organic-inorganic nanocomposites synthesized via sol-gel chemistry. *Journal of Materials Chemistry* 1999, 9 (1), 35-44.

51. Schottner, G., Hybrid sol-gel-derived polymers: Applications of multifunctional materials. *Chemistry of Materials* 2001, 13 (10), 3422-3435.
52. Haas, K. H., Hybrid inorganic-organic polymers based on organically modified Si-alkoxides. *Advanced Engineering Materials* 2000, 2 (9), 571-582.
53. Jena, K. K.; Rout, T. K.; Narayan, R.; Raju, K., Novel organic-inorganic hybrid coatings prepared by the sol-gel process: corrosion and mechanical properties. *Polymer International* 2012, 61 (7), 1101-1106.
54. Hench, L. L.; West, J. K., THE SOL-GEL PROCESS. *Chemical Reviews* 1990, 90 (1), 33-72.
55. Mahltig, B.; Haufe, H.; Bottcher, H., Functionalisation of textiles by inorganic sol-gel coatings. *Journal of Materials Chemistry* 2005, 15 (41), 4385-4398.
56. Cheng, Y. L.; Hsieh, C. Y.; Chang, Y. L., Deposition cycle of atomic layer deposition HfO₂ film: Effects on electrical performance and reliability. *Thin Solid Films* 2013, 528, 77-81.
57. Eisenbraun, E.; van der Straten, O.; Zhu, Y.; Dovidenko, K.; Kaloyeros, A.; Ieee, Atomic layer deposition (ALD) of tantalum-based materials for zero thickness copper barrier applications. *Proceedings of the Ieee 2001 International Interconnect Technology Conference* 2001, 207-209.
58. Wang, X. W.; Dong, L.; Zhang, J. Y.; Liu, Y. Q.; Ye, P. D. D.; Gordon, R. G., Heteroepitaxy of La₂O₃ and La_{2-x}Y_xO₃ on GaAs (111)A by Atomic Layer Deposition: Achieving Low Interface Trap Density. *Nano Letters* 2013, 13 (2), 594-599.
59. Fischer, P.; Pierreux, D.; Rouault, O.; Sirugue, J.; Zagwijn, P.; Tois, E.; Haukka, S., Batch Atomic Layer Deposition of HfO₂ and ZrO₂ Films Using Cyclopentadienyl Precursors. *Atomic Layer Deposition Applications* 4 2008, 16 (4), 135-148.
60. Niinisto, L.; Paivasaari, J.; Niinisto, J.; Putkonen, M.; Nieminen, M., Advanced electronic and optoelectronic materials by Atomic Layer Deposition: An overview with special emphasis on recent progress in processing of high-k dielectrics and other oxide materials. *Physica Status Solidi a-Applied Research* 2004, 201 (7), 1443-1452.
61. Ferguson, J. D.; Weimer, A. W.; George, S. M., Atomic layer deposition of Al₂O₃ films on polyethylene particles. *Chemistry of Materials* 2004, 16 (26), 5602-5609.
62. Hyde, G. K.; Park, K. J.; Stewart, S. M.; Hinstroza, J. P.; Parsons, G. N., Atomic layer deposition of Conformal inorganic nanoscale coatings on three-dimensional natural

fiber systems: Effect of surface topology on film growth characteristics. *Langmuir* 2007, 23 (19), 9844-9849.

63. Hyde, G. K.; McCullen, S. D.; Jeon, S.; Stewart, S. M.; Jeon, H.; Lobo, E. G.; Parsons, G. N., Atomic layer deposition and biocompatibility of titanium nitride nano-coatings on cellulose fiber substrates. *Biomedical Materials* 2009, 4 (2).

64. Hyde, G. K.; Scarel, G.; Spagnola, J. C.; Peng, Q.; Lee, K.; Gong, B.; Roberts, K. G.; Roth, K. M.; Hanson, C. A.; Devine, C. K.; Stewart, S. M.; Hojo, D.; Na, J. S.; Jur, J. S.; Parsons, G. N., Atomic Layer Deposition and Abrupt Wetting Transitions on Nonwoven Polypropylene and Woven Cotton Fabrics. *Langmuir* 2010, 26 (4), 2550-2558.

65. Jen, S. H.; Lee, B. H.; George, S. M.; McLean, R. S.; Carcia, P. F., Critical tensile strain and water vapor transmission rate for nanolaminate films grown using Al₂O₃ atomic layer deposition and alucone molecular layer deposition. *Applied Physics Letters* 2012, 101 (23), 3.

66. Jen, S. H.; George, S. M., Alucone Interlayers to Minimize Stress Caused by Thermal Expansion Mismatch between Al₂O₃ Films and Teflon Substrates. *Acs Applied Materials & Interfaces* 2013, 5 (3), 1165-1173.

67. Jur, J. S.; Spagnola, J. C.; Lee, K.; Gong, B.; Peng, Q.; Parsons, G. N., Temperature-Dependent Subsurface Growth during Atomic Layer Deposition on Polypropylene and Cellulose Fibers. *Langmuir* 2010, 26 (11), 8239-8244.

68. Jur, J. S.; Sweet, W. J.; Oldham, C. J.; Parsons, G. N., Atomic Layer Deposition of Conductive Coatings on Cotton, Paper, and Synthetic Fibers: Conductivity Analysis and Functional Chemical Sensing Using "All-Fiber" Capacitors. *Advanced Functional Materials* 2011, 21 (11), 1993-2002.

69. Kaariainen, T. O.; Kelly, P. J.; Cameron, D. C.; Beake, B.; Li, H. Q.; Barker, P. M.; Struller, C. F., Nanoscratch testing of atomic layer deposition and magnetron sputtered TiO₂ and Al₂O₃ coatings on polymeric substrates. *Journal of Vacuum Science & Technology A* 2012, 30 (1), 9.

70. Kemell, M.; Pore, V.; Ritala, M.; Leskela, M.; Linden, M., Atomic layer deposition in nanometer-level replication of cellulosic substances and preparation of photocatalytic TiO₂/cellulose composites. *Journal of the American Chemical Society* 2005, 127 (41), 14178-14179.

71. Kemell, M.; Ritala, M.; Leskela, M.; Groenen, R.; Lindfors, S., Coating of Highly Porous Fiber Matrices by Atomic Layer Deposition. *Chemical Vapor Deposition* 2008, 14 (11-12), 347-352.

72. Knez, M.; Kadri, A.; Wege, C.; Gosele, U.; Jeske, H.; Nielsch, K., Atomic layer deposition on biological macromolecules: Metal oxide coating of tobacco mosaic virus and ferritin. *Nano Letters* 2006, 6 (6), 1172-1177.
73. Lee, G. B.; Son, K. S.; Park, S. W.; Shim, J. H.; Choi, B.-H., Low-temperature atomic layer deposition of Al₂O₃ on blown polyethylene films with plasma-treated surfaces. *Journal of Vacuum Science & Technology A* 2013, 31 (1).
74. Ras, R. H. A.; Kemell, M.; de Wit, J.; Ritala, M.; ten Brinke, G.; Leskela, M.; Ikkala, O., Hollow inorganic nanospheres and nanotubes with tunable wall thicknesses by atomic layer deposition on self-assembled polymeric templates. *Advanced Materials* 2007, 19 (1), 102-+.
75. Wang, Y.; Qin, Y.; Berger, A.; Yau, E.; He, C.; Zhang, L.; Gosele, U.; Knez, M.; Steinhart, M., Nanoscopic Morphologies in Block Copolymer Nanorods as Templates for Atomic-Layer Deposition of Semiconductors. *Advanced Materials* 2009, 21 (27), 2763-+.
76. Skoog, S. A.; Elam, J. W.; Narayan, R. J., Atomic layer deposition: medical and biological applications. *International Materials Reviews* 2013, 58 (2), 113-129.
77. Marin, E.; Lanzutti, A.; Andreatta, F.; Lekka, M.; Guzman, L.; Fedrizzi, L., Atomic layer deposition: state-of-the-art and research/industrial perspectives. *Corrosion Reviews* 2011, 29 (5-6), 191-208.
78. Choi, D.-w.; Kim, S.-J.; Lee, J. H.; Chung, K.-B.; Park, J.-S., A study of thin film encapsulation on polymer substrate using low temperature hybrid ZnO/Al₂O₃ layers atomic layer deposition. *Current Applied Physics* 2012, 12, S19-S23.
79. Genevee, P.; Donsanti, F.; Renou, G.; Lincot, D., Study of the aluminum doping of zinc oxide films prepared by atomic layer deposition at low temperature. *Applied Surface Science* 2013, 264, 464-469.
80. Groner, M. D.; Fabreguette, F. H.; Elam, J. W.; George, S. M., Low-temperature Al₂O₃ atomic layer deposition. *Chemistry of Materials* 2004, 16 (4), 639-645.
81. Herrmann, C. F.; DelRio, F. W.; George, S. M.; Bright, V. M., Properties of atomic layer deposited Al₂O₃/ZnO dielectric films grown at low temperature for RF MEMS. In *Micromachining and Microfabrication Process Technology X*, Maher, M. A.; Stewart, H. D., Eds. 2005; Vol. 5715, pp 159-166.
82. Huang, Y.; Pandraud, G.; Sarro, P. M., Characterization of low temperature deposited atomic layer deposition TiO₂ for MEMS applications. *Journal of Vacuum Science & Technology A* 2013, 31 (1).

83. Jung, T.-H.; Park, J.-S.; Kim, D.-H.; Jeong, Y.; Park, S.-G.; Kwon, J.-D., Effect of in situ hydrogen plasma treatment on zinc oxide grown using low temperature atomic layer deposition. *Journal of Vacuum Science & Technology A* 2013, 31 (1).
84. Lin, Z.; Jiang, C.; Zhu, C.; Zhang, J., Development of Inverted Organic Solar Cells with TiO₂ Interface Layer by Using Low-Temperature Atomic Layer Deposition. *ACS applied materials & interfaces* 2013, 5 (3), 713-8.
85. Nam, T.; Kim, J.-M.; Kim, M.-K.; Kim, H.; Kim, W.-H., Low-temperature Atomic Layer Deposition of TiO₂, Al₂O₃, and ZnO Thin Films. *Journal of the Korean Physical Society* 2011, 59 (2), 452-457.
86. Tai, K.; Hirano, T.; Yamaguchi, S.; Ando, T.; Hiyama, S.; Wang, J.; Nagahama, Y.; Kato, T.; Yamanaka, M.; Terauchi, S.; Kanda, S.; Yamamoto, R.; Tateshita, Y.; Tagawa, Y.; Iwamoto, H.; Saito, M.; Nagashima, N.; Kadomura, S., High performance pMOSFET with ALD-TiN/HfO₂ gate stack on (110) substrate by low temperature process. In *ESSDERC 2006: Proceedings of the 36th European Solid-State Device Research Conference*, Ionescu, A. M.; Declercq, M.; Leblebici, Y., Eds. 2006; pp 121-124.
87. Sun, Y.; Padbury, R. P.; Akyildiz, H. A.; Goertz, M. P.; A., P. J.; Jur, J. S., Influence of Subsurface Hybrid Material Growth on the Mechanical Properties of Atomic Layer Deposited Thin Films on Polymers. *Chemical Vapor Deposition*: 2013.
88. Malato, S.; Fernandez-Ibanez, P.; Maldonado, M. I.; Blanco, J.; Gernjak, W., Decontamination and disinfection of water by solar photocatalysis: Recent overview and trends. *Catalysis Today* 2009, 147 (1), 1-59.
89. Mills, A.; Doyle, G.; Peiro, A. M.; Durrant, J., Demonstration of a novel, flexible, photocatalytic oxygen-scavenging polymer film. *Journal of Photochemistry and Photobiology a-Chemistry* 2006, 177 (2-3), 328-331.
90. Sherrill, J.; Michielsen, S.; Stojiljkovic, I., Grafting of light-activated antimicrobial materials to nylon films. *Journal of Polymer Science Part a-Polymer Chemistry* 2003, 41 (1), 41-47.
91. http://www.time.com/time/specials/packages/article/0,28804,1852747_1854195_1854176_00.html.
92. Choi, J. A.; Kim, S. H.; Kim, D. W., Enhancement of thermal stability and cycling performance in lithium-ion cells through the use of ceramic-coated separators. *Journal of Power Sources* 2010, 195 (18), 6192-6196.

93. Balducci, A.; Soavi, F.; Mastragostino, M., The use of ionic liquids as solvent-free green electrolytes for hybrid supercapacitors. *Applied Physics a-Materials Science & Processing* 2006, 82 (4), 627-632.
94. Tsunashima, K.; Sugiya, M., Electrochemical Behavior of lithium in room-temperature phosphonium ionic liquids as lithium battery electrolytes. *Electrochemical and Solid State Letters* 2008, 11 (2), A17-A19.
95. Mello, C. M.; Soares, J. W.; Arcidiacono, S.; Butlers, M. M., Acid extraction and purification of recombinant spider silk proteins. *Biomacromolecules* 2004, 5 (5), 1849-1852.
96. Lazaris, A.; Arcidiacono, S.; Huang, Y.; Zhou, J. F.; Duguay, F.; Chretien, N.; Welsh, E. A.; Soares, J. W.; Karatzas, C. N., Spider silk fibers spun from soluble recombinant silk produced in mammalian cells. *Science* 2002, 295 (5554), 472-476.
97. Prince, J. T.; McGrath, K. P.; Digirolamo, C. M.; Kaplan, D. L., CONSTRUCTION, CLONING, AND EXPRESSION OF SYNTHETIC GENES ENCODING SPIDER DRAGLINE SILK. *Biochemistry* 1995, 34 (34), 10879-10885.
98. Xia, X. X.; Qian, Z. G.; Ki, C. S.; Park, Y. H.; Kaplan, D. L.; Lee, S. Y., Native-sized recombinant spider silk protein produced in metabolically engineered Escherichia coli results in a strong fiber. *Proceedings of the National Academy of Sciences of the United States of America* 2010, 107 (32), 14059-14063.
99. Kessels, W. M. M.; Putkonen, M., Advanced process technologies: Plasma, direct-write, atmospheric pressure, and roll-to-roll ALD. *Mrs Bulletin* 2011, 36 (11), 907-913.
100. http://www.lotusat.com/roll_to_roll.html.
101. Beetstra, R.; Lafont, U.; Nijenhuis, J.; Kelder, E. M.; van Ommen, J. R., Atmospheric Pressure Process for Coating Particles Using Atomic Layer Deposition. *Chemical Vapor Deposition* 2009, 15 (7-9), 227-233.
102. Fitzpatrick, P. R.; Gibbs, Z. M.; George, S. M., Evaluating operating conditions for continuous atmospheric atomic layer deposition using a multiple slit gas source head. *Journal of Vacuum Science & Technology A* 2012, 30 (1).
103. Jur, J. S.; Parsons, G. N., Atomic Layer Deposition of Al₂O₃ and ZnO at Atmospheric Pressure in a Flow Tube Reactor. *Acs Applied Materials & Interfaces* 2011, 3 (2), 299-308.

104. Mousa, M. B. M.; Oldham, C. J.; Jur, J. S.; Parsons, G. N., Effect of temperature and gas velocity on growth per cycle during Al₂O₃ and ZnO atomic layer deposition at atmospheric pressure. *Journal of Vacuum Science & Technology A* 2012, 30 (1).
105. van Deelen, L.; Kniknie, B.; Grob, F.; Volintiru, I.; Roozeboom, F.; Poodt, P.; Illiberi, A.; Ieee, Atmospheric Pressure Deposition of SnO₂ and ZnO. *2012 38th Ieee Photovoltaic Specialists Conference (Pvsc)* 2012, 2014-2017.

CHAPTER 2
THE EFFECT OF POLYMER MICROSTRUCTURE ON THE NUCLEATION
BEHAVIOR OF ALUMINA VIA ATOMIC LAYER DEPOSITION.

2.1. Introduction

Atomic layer deposition (ALD) is a thin film deposition technique in which nanoscale inorganic coatings are formed by sequential, self-limiting surface reactions using gas phase precursors.^{1,2} Historically, ALD has been widely used by the microelectronics industry to deposit high κ dielectric thin films on the transistors of microchips.³⁻⁶ The self-limiting nature of the reaction results in sub-atomic control of the inorganic coating thickness on both planar and complex surfaces.^{5,7-10} In recent years, ALD has been observed as a means of introducing inorganic material properties to flexible polymer substrates by direct reaction of the ALD precursors with the polymer functional groups.¹¹⁻¹⁹

ALD has been demonstrated on a broad range of polymers however, the polymer microstructure determines the morphology of the resultant inorganic coating. Research has revealed the formation of conformal surface coatings with abrupt interfaces (e.g. cellulose)¹³ and hybrid organic-inorganic coatings with graded sub-surface compositions.¹⁴ Hybrid organic-inorganic coatings form as a result of precursor diffusion through the porous sub-surface of the polymer followed by chemical reaction and nucleation. Hybrid organic-inorganic film formation via ALD was initially demonstrated on polyamide-6 (PA-6)¹⁴ but has also been shown to occur with other carbonyl containing polymers such as polyethylene terephthalate (PET)¹⁸, polylactic acid¹⁸ and poly (methyl methacrylate) (PMMA)^{18, 15}.

Polymers are highly versatile materials with microstructures that vary in size and shape from classic linear polymers to branched polymers with long pendant groups.²⁰ The polymer microstructure plays a significant role in the final properties of the material. Therefore, numerous generations of the same polymer have been developed for specific applications by maintaining the functional group chemistry with variations to the length of the repeat unit or side chain pendant groups. Examples of variations to repeat unit length include the extensive series of polyamides from PA-3 to PA-12, where the number indicates the number of carbon atoms between amide functional groups, to the series of polyesters from PET to poly(trimethylene terephthalate) (PTT) corresponding to the addition of CH₂ groups along the backbone of the repeat unit.²¹ An example of variation in pendant group size can be observed in the series of poly-n-methacrylate polymers in which the addition of CH₂ groups varies the length of the side chain pendant group.²¹ In all cases, there is a variation in functional group concentration and flexibility of the polymer chains resulting in different glass transition temperatures and the ability of the polymer to crystallize.

This work explores the growth of alumina ALD coatings on polymers by exposing a series of poly-n-methacrylate and polyester polymer films to sequential exposures of trimethyl aluminum and water using a typical ALD cycle sequence. Specifically, in-situ quartz crystal microgravimetry (QCM) is used to draw conclusions between polymer microstructure and the nucleation behavior of alumina. The impact of polymer structure on the ALD process conditions and the resultant growth of alumina ALD coatings on the polymer films are clarified in this work.

2.2. Experimental

Chemicals and materials. A series of poly-n-methacrylate polymer solutions were prepared by dissolving 3 wt. % polymethyl methacrylate (PMMA), polyethyl methacrylate (PEMA), polypropyl methacrylate (PPMA) and polybutyl methacrylate (PBMA) pellets (Scientific Polymer Products, Inc) in 99% purity Acetone (Sigma Aldrich Inc.). A series of polyester polymer solutions were prepared by dissolving polyethylene terephthalate (PET) and polybutylene terephthalate (PBT) pellets (Eastman and BASF, respectively) in 99% reagent grade Trifluoroacetic Acid (Sigma Aldrich Inc.). The polymer solutions were allowed to mix via magnetic stirring for approximately 12 hours at room temperature. Trimethyl Aluminum (TMA) (STREM chemicals CAS no. 75-24-1, 98% purity) and high purity water (Sigma Aldrich, biotechnology performance certified grade, CAS no. 7732-18-5) was used for alumina ALD experiments. The precursors were delivered into the reaction chamber using inert N₂ (Airgas National Welders, 99.999%) that was further purified with an Entegris Gatekeeper inert gas purifier.

In-situ QCM Analysis. One method of analysing precursor reactions with polymers is via quartz crystal microgravimetry (QCM). The QCM detects changes in mass per unit area by measuring the change in frequency of a quartz crystal resonator. The principal behind QCM analysis is the converse piezoelectric effect that was established by Gabriel Lippmann in 1881. Prior to Lippmann's work, the piezoelectric effect was discovered by Pierre and Jacques Curie who were able to show that mechanical strain in certain crystals, such as quartz, caused a build-up of charge in the material due to electric polarization detected as an induced voltage.²² The significance of Lippmann's work was to prove that the opposite was

also possible (*i.e. that deformation of a piezoelectric material can occur via an applied electric field*). Hence, in QCM analysis a piezoelectric crystal is placed in an alternating electric field causing it to oscillate in a mechanically resonant mode. During an ALD process, a change in frequency of the high Q-factor mechanically resonating crystal from its initial value is related to the mass added to the surface with nanogram resolution.^{23 24} This allows for a precise *in-situ* analysis of reactivity and growth of the ALD films on the surfaces of different polymers.

Thin Film Development and QCM Assembly. Polymer thin films of PMMA, PEMA, PPMA, PBT and PET were formed by spin coating (Laurell Technologies) a sufficient quantity of each polymer solution at 3000 rpm. The polymer thin films were spuncast directly onto unpolished, gold plated quartz crystals (resonant frequency of 6 MHz) obtained from Inficon and used as received. After spin coating, the polymer coated crystals were baked at 90 °C for 1 minute to ensure all of the residual solvent was removed from the polymer films. Ellipsometry measurements confirmed that the film thicknesses of PMMA, PEMA, PPMA, PBMA, PET and PBT were ~200nm, 240nm, 240nm, 270nm, 540nm and 900nm, respectively. For the QCM analysis of alumina ALD, both a quartz crystal and Si wafer were coated with 100 cycles of alumina using a cycle sequence of TMA/N₂/H₂O/N₂ = 0.2/30/0.2/45 seconds at 60°C. Ellipsometry measurements of the alumina coating on the Si wafer confirmed a film thickness of ~12nm corresponding to a growth per cycle (GPC) of ~1.2 angstrom/cycle. The polymer and alumina coated quartz crystals were placed inside a crystal drawer (Inficon) and secured with conductive silver epoxy (Electron Microscopy Sciences). After crystal assembly, the silver epoxy was cured at room temperature for 24 hrs.

The crystal drawer was mounted to a sensor head that was vacuum sealed inside the main chamber of the viscous flow reactor. The sensor head was modified to prevent buildup of inorganic material around the electrical contacts between the sensor head and the quartz crystal by allowing N₂ gas to continuously purge the backside of the quartz crystal during experiments. The change in the frequency of the quartz crystal before, during and after the precursor doses was monitored at a rate of 4 Hz.

QCM Analysis of Alumina ALD. A custom-made viscous flow reactor with a stainless steel conflat-sealed tube, 90 cm in length and 20 cm in diameter was used for alumina ALD experiments. The reactor was operated under vacuum using an Alcatel 2021SD mechanical pump. During each experiment the flow rate of the N₂ was controlled using an MKS (model PR4000B) flow controller. The reactor is heated using Omegalux fiberglass heating tapes, and the temperature is controlled by an Omega (model 616) temperature controller. Exposure of TMA and water was transported into the reactor through the use of Swagelok ALD pneumatic valves.

Prior to each experiment, the QCM is allowed to stabilize for several hours to reduce the magnitude of temperature induced mass transients in the mass uptake data. After stabilization, the Z-factor of the QCM is calculated to check that the change in frequency caused by the polymer thin film is within 2% of the uncoated quartz crystal frequency. Under this condition the Sauerbrey relationship is used to convert the change in frequency to a change in mass.²³ For the QCM analysis of an alumina ALD process, polymer and alumina coated quartz crystals were exposed to a cycle sequence of TMA/N₂/H₂O/N₂= 0.2/30/0.2/45

seconds at 60°C. The pressure of the viscous flow reactor was kept constant at 1 Torr with a nitrogen gas flow rate of ~300 sccm. The cycle sequence was repeated for 50 cycles.

QCM analysis of TMA doses. The infiltration of TMA into a series of poly-n-methacrylate and polyester films was performed at a reactor temperature of 60°C and 1 Torr. The influence of dose and purge time on the absorption and desorption of TMA in poly-n-methacrylate and polyester films was investigated by exposing the polymer films to a 0.2 second dose of TMA followed by a 20 min purge time. The effect of dose time was further investigated in poly-n-methacrylate films by varying the dose time of TMA from 0.2 seconds to 10 seconds.

2. 3. Results

The Alumina ALD Process. A typical ALD cycle follows a sequence of precursor and co-reactant doses separated by an inert gas purge step. The dose times of each step in the ALD sequence are optimized, based on the geometry, size and gas flow characteristics of the reactor, so that the exposure is sufficient to promote a fully saturated surface corresponding to one sub-atomic layer of growth per ALD cycle (GPC). The surface reactions are considered to be self-limiting when all available reactive sites are consumed or steric hindrance prevents the absorption and reaction of precursor molecules.²⁵ The ALD cycle sequence can be repeated to grow inorganic coatings with atomic scale precision.

In addition to precursor dose and surface exposure times, the GPC of the ALD process can also be optimized for a range of temperatures.²⁶ Figure 2.1 shows the ALD window for the apparatus used in this study. The temperature range between 50°C and 175°C consistently promotes one sub-atomic monolayer with a GPC of approximately 1.2

angstrom/cycle. As shown in Figure 2.1, uneven growth occurs either side of the temperature window. Below 50°C, a higher GPC could be caused by the condensation of precursors at lower reactor temperatures while above 175°C, there could be desorption or a loss of surface species required for further ALD nucleation resulting in a lower GPC.

Figure 2.2 (a) shows the mass uptake versus time of an alumina ALD process at 60°C on a quartz crystal pre-coated with 100 cycles of alumina. Prior to the onset of the first TMA dose, the reactor was purged for 600 seconds to provide an inert atmosphere and prevent unwanted reactions with the alumina coated quartz crystal surface. After the initial purge, the specimens were exposed to the first TMA dose at $t = 600$ seconds. As shown in Figure 2.2 (a), the mass uptake of alumina constantly increases in a step-wise fashion. This is characteristic of the sequential dosing of precursor and co-reactant separated by an inert gas purge step during an ALD process. The total mass gain of alumina after 50 cycles is approximately ~ 1930 ng/cm². Figure 2.2 (b) shows the mass uptake per dose of both TMA and water during 50 cycles of the alumina ALD process represented in Figure 2.1 (a). As one can see from Figure 2.1 (b), the mass uptake per dose of TMA and water follows a linear regime. This is indicated by the constant mass uptake per cycle of approximately 35 ng/cm²/cycle and 5 ng/cm²/cycle for TMA and water doses, respectively. Using a liquid density of 0.725 g/cm³ and a molar mass of 72.086 g/mol, Wilson et al. approximated the mass of one monolayer of TMA as 39.7 ng/cm².¹⁵ We attribute the slightly lower mass uptake of TMA shown in this work to the fact that absorbed TMA forms Al(CH₃)₂ groups which has a lower molar mass of ~ 57 g/mol. The linear mass uptake per cycle is a direct

result of the optimized precursor doses that sufficiently saturate the surface of the substrate promoting self-limiting reactions and the growth of one sub-atomic monolayer of alumina.

Alumina ALD on Polymers. In contrast, Figure 2.3 shows the mass uptake behaviour of alumina ALD on PBT and PPMA polymer films using an ALD cycle sequence of TMA/N₂/H₂O/N₂ = 0.2/30/0.2/45 seconds at 60°C. The alumina ALD curve from Figure 2.2 (a) is shown in Figure 2.3 for comparison to alumina ALD on polymers. For PBT there is a nucleation period between $t = 300$ seconds and $t = 750$ seconds as indicated by the large initial absorption and desorption of TMA during the first 6 cycles. This is characteristic of precursor infiltration into the sub-surface of the polymer film. During the first 6 ALD cycles in PBT, the absorption of TMA per cycle gradually reduces as the sub-surface alumina coating progresses towards the near surface of the polymer film resulting in an alumina mass uptake of ~ 3000 ng/cm² and. This is followed by typical linear ALD growth on the surface of the polymer between $t = 750$ seconds and $t = 3500$ seconds as indicated by the constant mass uptake per cycle. The final mass uptake of alumina at $t = 3500$ seconds is ~ 4500 ng/cm².

Similarly for PPMA, there is a nucleation period of alumina between $t = 300$ seconds and $t = 1000$ seconds corresponding to the first 10 cycles of the ALD process. This indicates that the nucleation period is slightly longer in the PPMA film. However, the initial absorption of TMA in PPMA and the mass uptake of alumina during the nucleation period (~ 1100 ng/cm²) are lower in comparison to the PBT film. Typical ALD growth on the surface of the PPMA film proceeds from $t = 1000$ seconds and $t = 3500$ seconds with a final mass uptake of alumina of ~ 2500 ng/cm².

Effect of Polymer Microstructure on TMA Absorption. Figure 2.4 shows the absorption of TMA into PBT and PET polymer films at 60°C. PET and PBT have the same ester functional group chemistry along the backbone of their polymer repeat units. However, PBT contains an aliphatic chain consisting of four CH₂ groups in comparison to PET that possesses two. Therefore, PBT is more flexible than PET which is evident in their different glass transition temperatures of 66 °C and 80°C, respectively.²¹ The polymer films were exposed to a cycle sequence of TMA/N₂/H₂O/N₂ = 0.2/600/0/600 seconds to specifically observe the initial absorption of TMA and the desorption characteristics during the purge step. As shown in Figure 2.4, the PBT film absorbs more TMA (~2625 ng/cm²) in comparison to the PET polymer film (~400 ng/cm²). Clearly there is significant desorption of TMA from both the PBT and PET polymer films during the 20 min purge step. However, as shown in Figure 2.4, the desorption of TMA from the PBT film occurs for approximately 120 seconds in comparison to the desorption of TMA from the PET film of approximately 100 seconds. Finally, the total mass uptake of TMA from the 0.2 second dose exposed to PBT after desorption of unreacted TMA is ~250 ng/cm² in comparison the total mass uptake of TMA in PET which is ~ 125 ng/cm².

Figure 2.5 (a) shows the absorption of TMA into a series of poly-n-methacrylate polymer films at 60°C. Specifically, TMA is exposed to PMMA, PEMA, PPMA and PBMA which are characterized by a pendant group consisting of an acryl group attached to a CH₂ groups. The length of the pendent group changes by the contribution of additional -CH₂- groups from one (PMMA) to four (PBMA). This makes the polymer more flexible which has a resultant effect on the glass transition temperature of the polymer. The T_g's of PMMA,

PEMA, PPMA and PBMA are approximately 115°C, 65 °C, 35°C and 15°C, respectively.²¹ As shown in Figure 2.5 (a), the PBMA film absorbs the largest quantity of TMA (~640 ng/cm²) in comparison to PPMA (~375 ng/cm²), PEMA (~125 ng/cm²) and PMMA (~60 ng/cm²). As shown in Figure 2.5(a), there is significant desorption of TMA from the series of poly-n-methacrylate films however, the PBMA film possesses the longest desorption period of TMA which is ~ 525 seconds. This is followed by PPMA with a desorption time of ~300 seconds and PEMA and PMMA both with desorption times of ~ 150 seconds. Finally, the total mass uptake of TMA from the 0.2 second dose is ~50 ng/cm² which is consistent in all of the polymer films except for PPMA which has a total mass uptake of ~100 ng/cm². It is interesting to note that the absorption of TMA in the series of poly-n-methacrylate films is considerably less than the absorption of TMA in PBT. Despite the lower absorption of TMA, the poly-n-methacrylate films also possess longer desorption times in comparison to PET and PBT.

To this point, the series of poly-n-methacrylate films were exposed to a larger dose of TMA as shown in Figure 2.5(b). The polymer films were exposed to a cycle sequence of TMA/N₂/H₂O/N₂ = 10/600/0/600 seconds. Once more, the PBMA film absorbs the largest quantity of TMA (~2266 ng/cm²) however; the longer dose corresponds to the absorption of ~ 3 times as much TMA in comparison to the 0.2 sec dose. The corresponding absorption of TMA in in PPMA, PEMA and PMMA is ~1300 ng/cm², 600 ng/cm² and 400 ng/cm², respectively. As shown in Figure 2.5(b), there is a corresponding increase in desorption time as more TMA has been absorbed and the final mass uptake of TMA is also slightly higher in

comparison to the 0.2 sec dose. The total mass uptake of TMA in PMMA, PEMA and PBMA is $\sim 200 \text{ ng/cm}^2$ whereas the final mass uptake of TMA in PPMA is $\sim 300 \text{ ng/cm}^2$

2. 4. Discussion

It is clear from Figure 2.3, that the exposure of different polymer systems to sequential TMA/H₂O doses using an ALD cycle sequence results in varied nucleation behaviors of alumina. This has been demonstrated in other studies by exploring alumina nucleation in a wide variety of polymer systems.^{15 14 18} In this study, we focus on a narrower range of polymer systems to isolate the underlying effect of polymer microstructure on the nucleation behavior of alumina in polymers. Specifically, by varying the pendant group size of a series of poly-n-methacrylate films and the length of the polymer repeat unit of a series of polyesters, we are able to alter the properties of the polymer and highlight the corresponding influence that polymer microstructure has on the absorption and nucleation of ALD precursors. To this end, Table 2.1 summarizes the absorption and desorption characteristics and the mass uptake of alumina in the polymer films studied in this work.

As shown in Figure 2.4 and summarized in Table 2.1, the absorption of a 0.2 sec dose of TMA in PBT is considerably higher than a 0.2 second dose of TMA in PET at 60°C. Table 2.1 also shows that the glass transition temperature (T_g) of PBT ($\sim 66^\circ\text{C}$) is lower than the T_g of PET ($\sim 80^\circ\text{C}$). Furthermore, with respect to the absorption of TMA in the series of poly-n-methacrylates, Table 2.1 shows that there is less absorption of TMA in PMMA with the highest T_g , while the PBMA film with the lowest T_g has the greatest absorption of TMA. Numerous polymer properties are affected by the glass transition temperature of the polymer relative to the temperature of the surroundings. This is due to the influence that thermal

energy has on the motion of polymer chain segments.²⁷ It has been stated that below T_g there is insufficient thermal energy to promote motion of polymer chain segments resulting in a reduction in polymer free volume as shown in Figure 6.²⁷ Above T_g the mobility of polymer chain segments is increased which corresponds to an increase in polymer free volume. At 60°C the temperature of the reactor is above the T_g of both PPMA and PBMA but below the T_g of PMMA. Therefore, as we transition through the series of poly-n-methacrylate polymer films we transition from a rubbery polymer with a large free volume to a glassy polymer with a reduced free volume as further indicated in Figure 2.6. Consequently, the increase in absorption of TMA in PBMA and PPMA polymer films is promoted by the increase in polymer free volume which can accommodate a larger quantity of TMA. Hence, the lower absorption of TMA in PMMA is caused by a reduced free volume that corresponds to a reduction in TMA absorption. The same theory applies to the absorption behavior of TMA in PBT and PET. The longer repeat unit of PBT is more flexible which means that it is easier to move polymer chain segments resulting in a lower T_g . Therefore, the lower T_g of PBT is attributed to the larger absorption of TMA at 60°C due to a greater polymer free volume in comparison to PET with the higher T_g and thus, lower polymer free volume.

A key question that arises is whether the variations in absorbed TMA are a result of the variations in polymer film thickness and hence, the specific volume of the polymer film. With respect to the series of polyesters, the PBT film is almost twice as thick as the PET film. Similarly, ellipsometry measurements confirm that the PBMA film is 70nm thicker than the PMMA film which corresponds to thickness variation of 35%. Using the data summarized in Table 1, a quick calculation reveals that the ratio of absorbed TMA from a 0.2

sec dose in PBT to PET is ~ 6.56 and the ratio of absorbed TMA from a 0.2 sec in PBMA to PMMA is ~ 10.67 . Furthermore, table 2.1 shows that with a 10 sec dose, the 270nm thick PBMA film achieves an absorbed mass uptake of TMA of $\sim 2266 \text{ ng/cm}^2$ which is comparable to the mass uptake of a 0.2 sec dose of TMA in PBT ($\sim 2625 \text{ ng/cm}^2$) with a thickness of $\sim 900\text{nm}$. This indicates that there is not a strong correlation between polymer thickness and the absorption of TMA. We anticipate that once a critical free volume has been achieved; there is sufficient space to accommodate absorbed TMA from the precursor dose time. Explicitly, the exposure of TMA from the ALD process parameters used in this work are low enough that the resultant absorption of TMA does not influence the entire free volume of the polymer films.

Despite this result, it is interesting to observe that the absorption of a 0.2 sec dose of TMA in the series of poly-n-methacrylate polymers is less than the absorption of TMA in the series of polyesters. As shown in Table 2.1 and Figure 2.5 (b), a larger TMA dose time is required to increase the absorption of TMA in the series of poly-n-methacrylate films to comparable levels of TMA absorption in polyesters from a lower 0.2 sec dose. Dorkenoo et al.²⁸ investigated the influence of aliphatic pendant groups with varying sizes (methyl to decyl) on the gas permeation characteristics of rigid polynorbornenes. Despite decreases in T_g as aliphatic pendant group size increased, the study shows that gas permeation decreased. The authors state that the linear pendant groups pack well resulting in a reduction in free volume despite a corresponding decrease in T_g . In this work, the poly-n-methacrylate backbone is more flexible however; we propose that the presence of side chain pendant groups occupy free volume that would otherwise be available for permeation. Therefore, the

lower absorption of TMA in comparison to the polyesters is due to a reduced free volume and tortuous network of interconnected pores created by the presence of pendant groups as shown in Figure 2.7. In comparison, the lack of bulky pendant groups in PET and PBT promotes a less tortuous path for the diffusion of solute molecules through the polymer. The effect of increasing the dose time on the absorption of TMA in the series of poly-n-methacrylate films, is to increase the exposure of TMA which provides more time for the precursor molecules to infiltrate the polymer film resulting in a greater absorption of TMA. The effect of pendant group size on the motion of solute molecules is expected to be more significant in PBMA in comparison to the other poly-n-methacrylate polymer films because it has the largest pendant group. However, this attribute only becomes evident when comparing the polymer to other polymer systems that do not possess pendant groups such as, PET and PBT. Moreover, this work demonstrates that the free volume influence on precursor absorption is the dominant mechanism of the absorption characteristics in polymers, particularly for polymers within the same family.

Table 2.1 summarizes the desorption times of TMA from the polyester and poly-n-methacrylate polymer films. As shown in Table 2.1, the desorption times of TMA from the polyesters is less than the desorption times from the poly-n-methacrylate polymer films. We further attribute this observation to the position of bulky side chain pendant groups along the backbone of the poly-n-methacrylate polymer films which hinder the diffusion of unreacted TMA out of the film. The difference in desorption time between polymer films within their respective series is due to variations in absorbed TMA. Clearly, the PBT polymer film

absorbs more TMA than the PET polymer film therefore, it is reasonable that the desorption time of unreacted TMA is slightly longer.

In addition to the unique absorption behavior of the polymer films explored in this study, the desorption of unreacted TMA also has a significant impact on the nucleation behavior of alumina initially observed in Figure 2.3. The nucleation of alumina was introduced to the PBT and PPMA polymer films shown in Figure 2.3 using an ALD cycle sequence (TMA/N₂/H₂O/N₂ = 0.2/30/0.2/45 seconds) optimized for a typical ALD process on an ‘ideal substrate’ such as silicon (Si) which has a high surface concentration of functional groups. It is clear from this study that the desorption of TMA from polymer systems continues for a longer period of time in comparison to the 30 seconds required to remove unreacted TMA from ideal substrates using a typical ALD cycle sequence. Therefore, we anticipate that the water molecules from the water dose could react with desorbing TMA to promoting undesirable reactions in addition to the direct reaction between precursor molecules and functional groups of the polymer. We hypothesize that this could correspond to CVD like nucleation behaviour in preference to a purely hybrid organic-inorganic interface. The effect is greater in PBT in comparison to the PPMA film since the PBT polymer film absorbs more TMA. This explains the larger mass uptake and shorter nucleation period of alumina in the sub-surface of the PBT film in comparison to the PPMA film.

To demonstrate the importance of purge time on the nucleation behaviour of alumina in polymers, Figure 2.8 compares alumina ALD on PBMA using a typical ALD cycle sequence with alumina ALD on PPMA with a longer precursor purge time. It is important to

note that the typical water purge time was maintained at 45 seconds for both experiments since the majority of the water dose is consumed by chemical reaction with absorbed TMA. As shown in Figure 2.8, the introduction of the water dose prematurely during the typical ALD process results in a greater mass gain of alumina and a shorter nucleation period. In contrast, the mass uptake of alumina is significantly lower when unreacted TMA is given time to diffuse out of the film prior to the exposure of H₂O since the additional reaction mode between water and unreacted TMA is eliminated. Therefore, this study shows that to form a pure hybrid organic-inorganic interface using ALD, the effect of polymer microstructure on the absorption and desorption characteristics must be considered and the ALD process parameters must be adjusted accordingly. Since an increase in purge time is required to fully remove unreacted TMA from the polymer film prior to the water dose, there is a considerable increase to the overall process time. Therefore, modified ALD processes such as sequential vapour infiltration (SVI)^{11, 29-30}, sequential infiltration synthesis (SIS)³¹ or multiple pulse infiltration (MPI)³² may be more applicable to the hybrid modification of polymers by promoting vapour infiltration and providing more time for TMA to directly react with functional groups along the backbone of the polymer.

2.5. Conclusion

This study investigates the effect of polymer microstructure on the nucleation behavior of alumina during a typical ALD process using sequential exposures of TMA and water. The data indicates that the glass transition temperature as influenced by variations in microstructure has a significant impact on the absorption of TMA. As shown in this work, polymers that possess lower T_g 's absorb larger quantities of TMA due to a larger free volume

whereas polymers with higher T_g 's absorb less TMA due to a reduced free volume. Furthermore, the presence of side chain pendant groups in poly-n-methacrylate polymers hinders the absorption and desorption of unreacted TMA due to the tortuous path of interconnected pores created within the polymer film. The absorption of TMA influences the desorption time required to remove unreacted TMA from the polymer film prior to the water dose. In general, large quantities of absorbed TMA result in longer desorption times of TMA. This has a dramatic impact on the nucleation behavior of alumina using typical ALD cycle sequences that have been optimized for 'ideal' ALD processes. Therefore, this work shows that the influence of polymer microstructure on the absorption and desorption characteristics of organometallic precursors must be considered and the ALD process parameters adjusted accordingly to promote the formation of desirable inorganic material interfaces.

Chapter 2 Figures:

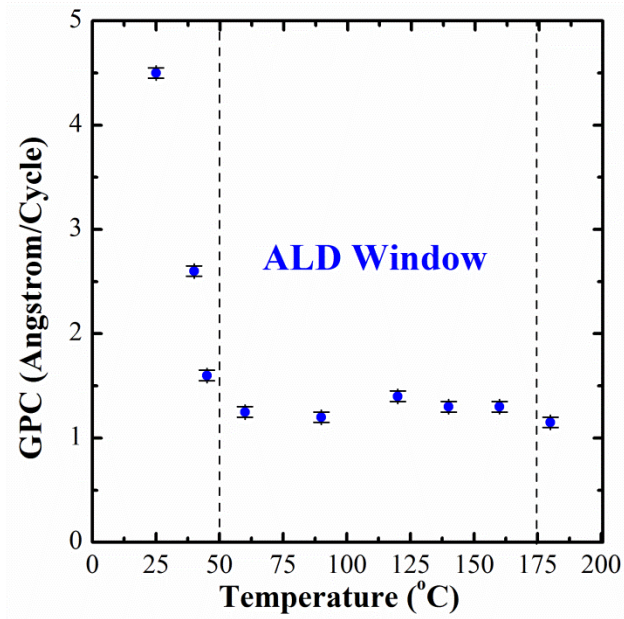


Figure 2.1. Growth per cycle (GPC) of alumina as a function of temperature formed by analyzing alumina growth on Si wafers using an alumina ALD cycle sequence of TMA/N₂/H₂O/N₂= 0.2/30/0.2/45 secocnds. Si wafers were exposed to the sequence for 100 cycles at the various reactor temperatures. Ellipsometry measurements were used to determine the thickness of alumina coatings on Si wafers which was converted to an average growth per cycle.

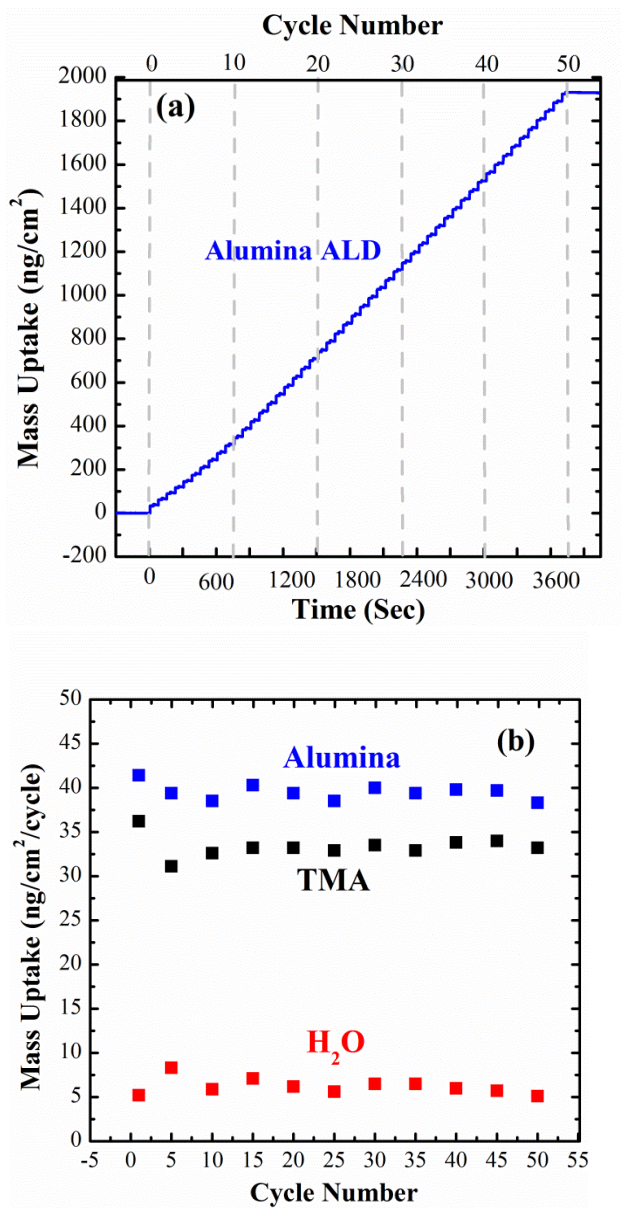


Figure 2.2. (a) QCM Analysis of an Alumina ALD process at 60°C and 1 Torr on a quartz crystal pre-deposited with 100 cycles of alumina. The mass deposition rate is indicated in (b) which corresponds to the mass uptake per cycle.

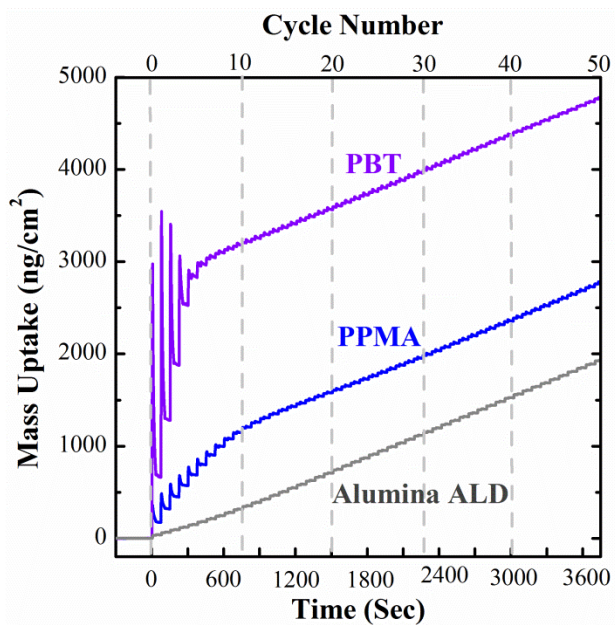


Figure 2.3. QCM Analysis of an Alumina ALD process at 60°C and 1 Torr on PBT and PPMA polymer thin films. The alumina ALD process from Figure 2 (a) is provided for comparison to demonstrate the unique nucleation behavior of ALD on polymers.

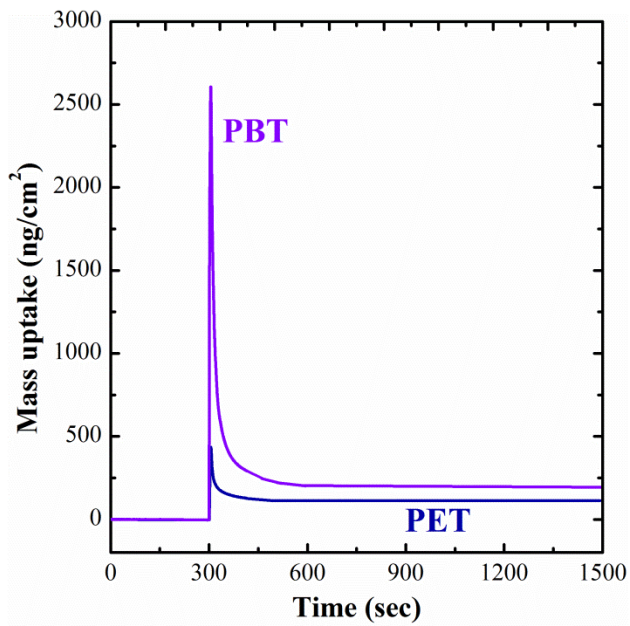


Figure 2.4. QCM analysis of a single 0.2 second TMA dose in PBT and PET films at 60°C. The analysis emphasizes the unique absorption/desorption characteristics of TMA in these polymer films.

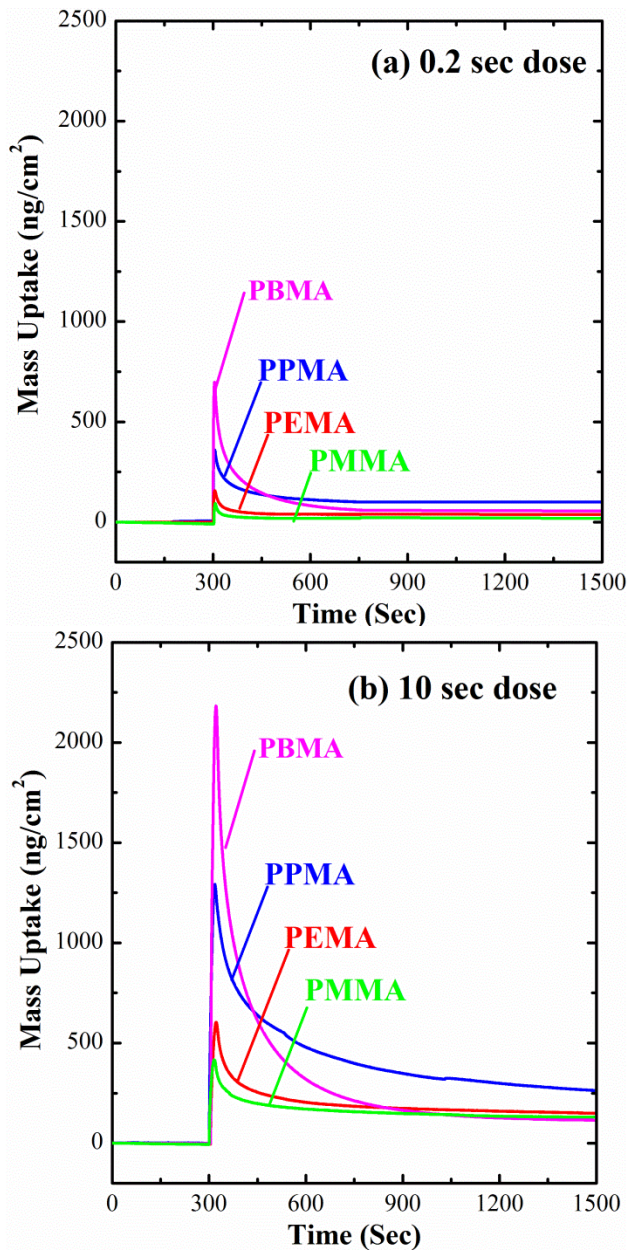


Figure 2.5. (a) QCM analysis of a single 0.2 second TMA dose in a series of poly-n-methacrylate polymer films at 60°C . The analysis emphasizes the unique absorption/desorption characteristics of TMA in these polymer films. The absorption of TMA is less than the absorption of TMA in polyesters. Therefore, (b) indicates the absorption/desorption of TMA at 60°C with a longer TMA dose of 10 secs.

Table 2.1. Summary of absorption/desorption characteristics of TMA exposed to the polymers analyzed in this work

Polymer	Tg (°C)²¹	TMA dose time (sec)	Absorbed TMA (ng/cm²)	Desorbed TMA (ng/cm²)	Desorption Time (sec)	Final TMA Mass Uptake (ng/cm²)
PMMA	115	0.2	60	10	150	50
		10	400	200	350	200
PEMA	65	0.2	125	75	150	50
		10	600	400	450	200
PPMA	35	0.2	375	275	300	100
		10	1300	1000	1200	300
PBMA	15	0.2	640	590	525	50
		10	2266	2066	900	200
PET	80	0.2	400	275	150	125
PBT	66	0.2	2625	2375	225	250

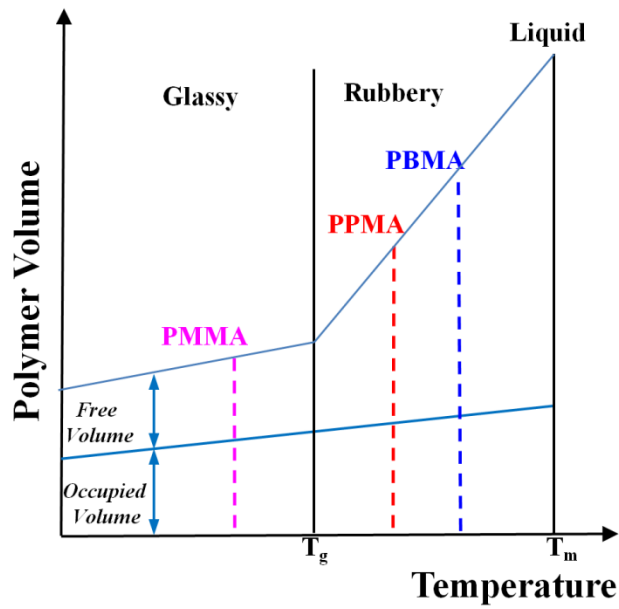


Figure 2.6. Effect of temperature on the specific volume of polymers adapted from ref (27). The diagram shows that the specific volume of polymers can be split up into the volume occupied by constituent atoms and the space between polymer chains called the free volume. The glass transition temperature indicates the point at which the polymer transitions from a glassy brittle material with a low free volume, to a rubbery flexible material with a high free volume.

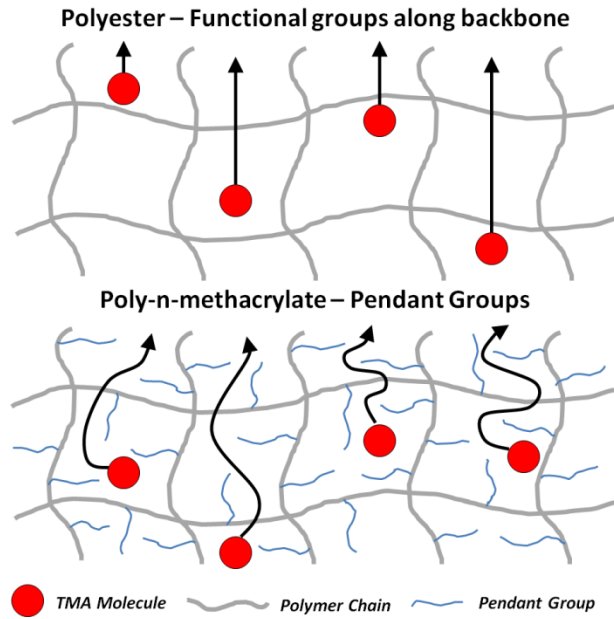


Figure 2.7. Diagram describing the variation in absorption characteristics of polymers that contain side chain pendant groups. The presence of pendant groups reduces available free volume for vapor infiltration as a result of the tortuous network of interconnected pores in comparison to polymers lacking pendant groups such as polyesters.

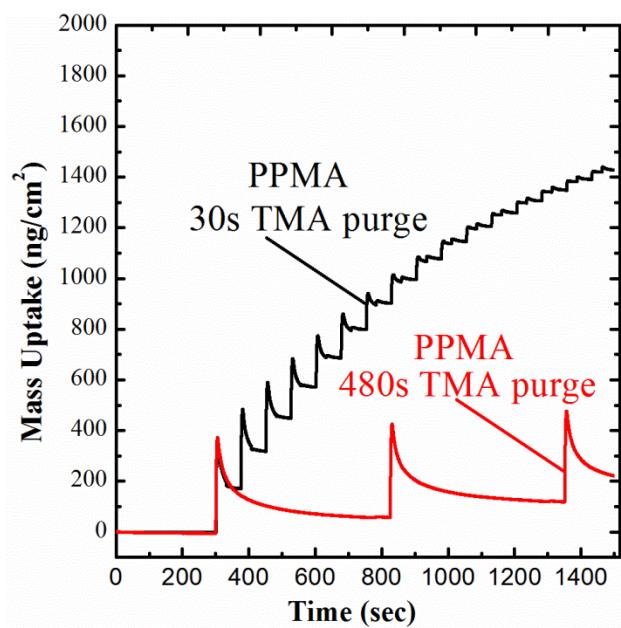


Figure 2.8. QCM Analysis of an Alumina ALD process at 60°C and 1 Torr on PPMA polymer thin films with varying TMA purge times. The analysis indicates a slower nucleation period and reduced mass gain of alumina as purge time increases.

Chapter 2 References:

1. Leskela, M.; Ritala, M., Atomic layer deposition (ALD): from precursors to thin film structures. *Thin Solid Films* **2002**, *409* (1), 138-146.
2. Parsons, G. N.; George, S. M.; Knez, M., Progress and future directions for atomic layer deposition and ALD-based chemistry. *Mrs Bulletin* **2011**, *36* (11), 865-871.
3. Cheng, Y. L.; Hsieh, C. Y.; Chang, Y. L., Deposition cycle of atomic layer deposition HfO₂ film: Effects on electrical performance and reliability. *Thin Solid Films* **2013**, *528*, 77-81.
4. Eisenbraun, E.; van der Straten, O.; Zhu, Y.; Dovidenko, K.; Kaloyeros, A.; Ieee, Atomic layer deposition (ALD) of tantalum-based materials for zero thickness copper barrier applications. *Proceedings of the Ieee 2001 International Interconnect Technology Conference* **2001**, 207-209.
5. Gluch, J.; Rossler, T.; Schmidt, D.; Menzel, S. B.; Albert, M.; Eckert, J., TEM characterization of ALD layers in deep trenches using a dedicated FIB lamellae preparation method. *Thin Solid Films* **2010**, *518* (16), 4553-4555.
6. Wang, X. W.; Dong, L.; Zhang, J. Y.; Liu, Y. Q.; Ye, P. D. D.; Gordon, R. G., Heteroepitaxy of La₂O₃ and La_{2-x}Y_xO₃ on GaAs (111)A by Atomic Layer Deposition: Achieving Low Interface Trap Density. *Nano Letters* **2013**, *13* (2), 594-599.
7. Devine, C. K.; Oldham, C. J.; Jur, J. S.; Gong, B.; Parsons, G. N., Fiber Containment for Improved Laboratory Handling and Uniform Nanocoating of Milligram Quantities of Carbon Nanotubes by Atomic Layer Deposition. *Langmuir* **2011**, *27* (23), 14497-14507.
8. Roth, K. M.; Roberts, K. G.; Hyde, G. K., Effect of Weave Geometry on Surface Energy Modification of Textile Materials via Atomic Layer Deposition. *Textile Research Journal* **2010**, *80* (18), 1970-1981.
9. Knez, M.; Niesch, K.; Niinisto, L., Synthesis and surface engineering of complex nanostructures by atomic layer deposition. *Advanced Materials* **2007**, *19* (21), 3425-3438.
10. Lu, Y. R.; Bangsaruntip, S.; Wang, X. R.; Zhang, L.; Nishi, Y.; Dai, H. J., DNA functionalization of carbon nanotubes for ultrathin atomic layer deposition of high kappa dielectrics for nanotube transistors with 60 mV/decade switching. *Journal of the American Chemical Society* **2006**, *128* (11), 3518-3519.
11. Gong, B.; Spagnola, J. C.; Parsons, G. N., Hydrophilic mechanical buffer layers and stable hydrophilic finishes on polydimethylsiloxane using combined sequential vapor

infiltration and atomic/molecular layer deposition. *Journal of Vacuum Science & Technology A* **2012**, *30* (1).

12. Hyde, G. K.; Scarel, G.; Spagnola, J. C.; Peng, Q.; Lee, K.; Gong, B.; Roberts, K. G.; Roth, K. M.; Hanson, C. A.; Devine, C. K.; Stewart, S. M.; Hojo, D.; Na, J. S.; Jur, J. S.; Parsons, G. N., Atomic Layer Deposition and Abrupt Wetting Transitions on Nonwoven Polypropylene and Woven Cotton Fabrics. *Langmuir* **2010**, *26* (4), 2550-2558.

13. Jur, J. S.; Spagnola, J. C.; Lee, K.; Gong, B.; Peng, Q.; Parsons, G. N., Temperature-Dependent Subsurface Growth during Atomic Layer Deposition on Polypropylene and Cellulose Fibers. *Langmuir* **2010**, *26* (11), 8239-8244.

14. Spagnola, J. C.; Gong, B.; Arvidson, S. A.; Jur, J. S.; Khan, S. A.; Parsons, G. N., Surface and sub-surface reactions during low temperature aluminium oxide atomic layer deposition on fiber-forming polymers. *Journal of Materials Chemistry* **2010**, *20* (20), 4213-4222.

15. Wilson, C. A.; Grubbs, R. K.; George, S. M., Nucleation and growth during Al₂O₃ atomic layer deposition on polymers. *Chemistry of Materials* **2005**, *17* (23), 5625-5634.

16. Halbur, J. C.; Padbury, R. P.; Jur, J. S., Induced wetting of polytetrafluoroethylene by atomic layer deposition for application of aqueous-based nanoparticle inks. *Materials Letters* **2013**, *101*, 25-28.

17. Kalanyan, B.; Oldham, C. J.; Sweet, W. J.; Parsons, G. N., Highly Conductive and Flexible Nylon-6 Nonwoven Fiber Mats Formed using Tungsten Atomic Layer Deposition. *Acs Applied Materials & Interfaces* **2013**, *5* (11), 5253-5259.

18. Gong, B.; Parsons, G. N., Quantitative in situ infrared analysis of reactions between trimethylaluminum and polymers during Al₂O₃ atomic layer deposition. *Journal of Materials Chemistry* **2012**, *22* (31), 15672-15682.

19. Jur, J. S.; Sweet, W. J.; Oldham, C. J.; Parsons, G. N., Atomic Layer Deposition of Conductive Coatings on Cotton, Paper, and Synthetic Fibers: Conductivity Analysis and Functional Chemical Sensing Using "All-Fiber" Capacitors. *Advanced Functional Materials* **2011**, *21* (11), 1993-2002.

20. Billmeyer, F. W., TEXTBOOK OF POLYMER SCIENCE. Springer: 2007.

21. Brandrup, J.; Immergut, E. H.; Grulke, E. A.; Abe, A.; Bloch, D. R., Handbook of Polymers. John Wiley & Sons: 2005.

22. Jones, D. J.; Prasad, S. E.; Wallace, J. B., Piezoelectric materials and their applications. *Advanced Ceramic Materials: Applications of Advanced Materials in a High-Tech Society I* **1996**, 122-1, 71-143.
23. Elam, J. W.; Groner, M. D.; George, S. M., Viscous flow reactor with quartz crystal microbalance for thin film growth by atomic layer deposition. *Review of Scientific Instruments* **2002**, 73 (8), 2981-2987.
24. Wind, R. A.; George, S. M., Quartz Crystal Microbalance Studies of Al₂O₃ Atomic Layer Deposition Using Trimethylaluminum and Water at 125 degrees C. *Journal of Physical Chemistry A* **2010**, 114 (3), 1281-1289.
25. Puurunen, R. L., Surface chemistry of atomic layer deposition: A case study for the trimethylaluminum/water process. *Journal of Applied Physics* **2005**, 97 (12).
26. George, S. M., Atomic Layer Deposition: An Overview. *Chemical Reviews* **2010**, 110 (1), 111-131.
27. P. Neogi, *Diffusion in Polymers*. New York : Marcel Dekker: 1996.
28. Dorkenoo, K. D.; Pfromm, P. H.; Rezac, M. E., Gas transport properties of a series of high T-g polynorbornenes with aliphatic pendant groups. *Journal of Polymer Science Part B-Polymer Physics* **1998**, 36 (5), 797-803.
29. Akyildiz, H. I.; Padbury, R. P.; Parsons, G. N.; Jur, J. S., Temperature and Exposure Dependence of Hybrid Organic-Inorganic Layer Formation by Sequential Vapor Infiltration into Polymer Fibers. *Langmuir* **2012**, 28 (44), 15697-15704.
30. Gong, B.; Peng, Q.; Jur, J. S.; Devine, C. K.; Lee, K.; Parsons, G. N., Sequential Vapor Infiltration of Metal Oxides into Sacrificial Polyester Fibers: Shape Replication and Controlled Porosity of Microporous/Mesoporous Oxide Monoliths. *Chemistry of Materials* **2011**, 23 (15), 3476-3485.
31. Peng, Q.; Tseng, Y. C.; Darling, S. B.; Elam, J. W., A Route to Nanoscopic Materials via Sequential Infiltration Synthesis on Block Copolymer Templates. *Acs Nano* **2011**, 5 (6), 4600-4606.
32. Lee, S. M.; Pippel, E.; Gosele, U.; Dresbach, C.; Qin, Y.; Chandran, C. V.; Brauniger, T.; Hause, G.; Knez, M., Greatly Increased Toughness of Infiltrated Spider Silk. *Science* **2009**, 324 (5926), 488-492.

CHAPTER 3

TEMPERATURE DEPENDANT INFILTRATION OF POLYMERS DURING SEQUENTIAL EXPOSURES TO TRIMETHYL ALUMINUM

3.1. Introduction

Synthetic polymers are pervasive in everyday life with an extensive range of application in apparel,¹⁻³ packaging,⁴⁻⁸ electrical insulation,^{9, 10} wound dressings and drug delivery,¹¹⁻¹⁴ filtration,¹⁵⁻¹⁷ high impact protection, chemical and fire protection.^{3, 18, 19} The large molecular mass and long chain nature of polymers corresponds to unique physical properties that distinguish them from other materials. Polymers are most often differentiated from each other by their unique chemistries and microstructures.²⁰ Therefore, polymer properties can be tuned for specific applications by varying monomer combinations, the polymerization technique and the manufacturing process to change their microstructure and morphology. Alternatively, the surface properties of polymers can be modified to maintain their bulk properties to improve performance for a given application. This typically involves a change in surface functionality or the introduction of a surface finish using one of many post processing techniques such as, pad-dry-cure²¹⁻²⁴, surface grafting^{21, 25} or atmospheric plasma.²⁶

The increasing demand for flexible, high performance materials has expanded the potential use of polymers into more novel applications. As a result, alternative techniques for developing polymers with specific surface properties are required to manage the necessity for new, high performance materials. The incorporation of inorganic materials properties into

polymers has been observed as a unique way to develop polymers with exceptional surface properties such as electrical conductivity,^{27, 28} low permeability,²⁹ catalytic behavior,^{7, 24, 30} and resistance to degradation mechanisms.³¹⁻³³ Sol-gel and chemical vapor deposition (CVD) techniques have been explored as methods for introducing inorganic coatings to polymers.^{31, 34-37} The challenges associated with the sol-gel technique includes the final thickness, uniformity and porosity of the inorganic coating due to control of the hydrolysis reaction and thermal treatment.^{34, 36} CVD can also result in non uniform coatings due to the mixing of vapor species and lack of control of their reaction with the substrate surface.³⁷ Atomic layer deposition (ALD) has also been identified as a viable surface modification technique of polymers due to the conformal, pinhole free quality of the inorganic coatings and the ability to grow inorganic coatings at low temperatures.³⁸⁻⁴²

Previous research has revealed the varied nucleation and growth behavior of inorganic coatings on different polymer chemistries via ALD. Analysis using cross-section TEM clarifies the formation of inorganic coatings with varied compositions of finish.^{40, 43} Conformal surface coatings with an abrupt interface between the ALD coating and the polymer is observed in polymers that possess high concentrations of surface functional groups, such as cotton or polyvinyl alcohol (PVOH).⁴³ In contrast, ALD growth on inert polymers such as polypropylene (PP) results in a characteristic CVD-initiated island growth, the evolution of which occurs in the subsurface regions of the polymer surface.^{43, 44} Further analysis has shown the temperature dependence of precursor infiltration into PP as the thermal expansion of the polymer at elevated temperatures leads to higher precursor mass gains.⁴³ Analysis of ALD growth on carbonyl-containing polymers (C=O), such as

polyamides and polyesters, has shown that organometallic precursors penetrate the sub-surface of the polymer and react to produce a graded hybrid (organic-inorganic) finish.^{40, 45, 46} Therefore, the growth of this finish is dependent on the balance between two competing mechanisms: (i) the rate of precursor diffusion into the polymer, and (ii) the subsequent chemical reaction between the functional groups and ALD precursors.

While numerous studies have elucidated the fundamental nucleation and growth mechanisms of inorganic coatings on polymers, these experiments investigate precursor exposures at fixed temperatures or limited temperature ranges. Various polymer properties are affected by temperature due to the thermal motion of polymer chain segments and the relative difference between the surrounding temperature and the glass transition temperature of the polymer. Therefore, this work addresses the rate of precursor infiltration as temperature varies. In particular, in-situ quartz crystal microgravimetry (QCM) is employed by spin casting polyamide-6 (PA-6), poly (acrylic acid) (PAA), poly (ethylene terephthalate) (PET) and acrylic thin films of nanoscale thickness onto quartz crystal and exposing them to multiple doses of TMA at different temperatures.

3.2. Experimental Procedure

Chemicals and materials. PA-6 polymer solutions were prepared by dissolving 3 wt. % PA-6 pellets (Ultramid®) in 95% purity formic acid (reagent grade, Sigma Aldrich Inc.). PAA solutions were prepared by dissolving 3 wt. % PAA powder (Sigma Aldrich Inc.) in deionized water. PET solutions were prepared by dissolving 3 wt. % PET pellets (BASF) in 95% purity trifluoroacetic Acid (Sigma Aldrich Inc.). The acrylic polymer solutions;

poly(methyl methacrylate) (PMMA), poly(propyl methacrylate) (PPMA) and poly(butyl methacrylate) (PBMA) (Scientific Polymer Products, Inc.) were prepared by dissolving 3 wt. % polymer powder in 99% purity Acetone (Sigma Aldrich Inc.). The polymer solutions were allowed to mix via magnetic stirring for approximately 12 hours at room temperature.

Spin coating procedure and QCM assembly. Polymer thin films of PA-6, PET, PAA, PMMA, PPMA and PBMA and were formed by spin coating (Laurell Technologies) a sufficient quantity of each polymer solution at 3000 rpm. The polymer thin films were spun directly onto unpolished, gold plated quartz crystals (resonant frequency of 6 MHz) obtained from Inficon and used as received. After spin coating, the polymer coated crystals were baked at 90 °C for 1 minute to ensure all of the residual solvent was removed from the polymer films. Ellipsometry measurements of PA-6, PET, acrylic and PAA films spun on to silicon wafers confirmed film thickness of 420 nm, 560, 260 and 210 nm respectively. The polymer coated quartz crystal was placed inside a crystal drawer (Inficon) and secured with conductive silver epoxy (Electron Microscopy Sciences). After crystal assembly, the crystal drawer was placed in an oven at 120 °C for one hour to cure the silver epoxy. The crystal drawer was mounted to a sensor head that was vacuum sealed inside the main chamber of the viscous flow reactor. The sensor head was modified to prevent buildup of inorganic material around the electrical contacts between the sensor head and the quartz crystal by allowing N₂ gas to continuously purge the backside of the quartz crystal during experiments. The change in the frequency of the quartz crystal before, during and after the precursor doses was monitored at a rate of 4 Hz. The moisture regain of each polymer varies from 0.4 wt. % in PET to 4 wt. % in PA-6. PAA is also known to absorb many times its weight in water.⁴⁷

Therefore, to remove water from the polymer films, *in situ* heating at 120 °C for 1 hr was performed in a nitrogen environment at 1 Torr. After *in situ* heating, the crystal was cooled to the desired exposure temperature.

QCM analysis and TMA exposures. The infiltration of TMA into PA-6, PET, PMMA and PAA polymer films was performed at varied reactor temperatures ranging from 30 to 150 °C. A fresh coated quartz crystal was used for each experiment performed at a different reaction chamber temperature. Prior to each experiment, the QCM was allowed to stabilize for several hours to the designated reaction chamber temperature. The temperature stabilization is important for reducing the magnitude of temperature induced mass transients in the mass uptake data. The experiments were not conducted until the change in frequency of the quartz crystal was $\leq \pm 0.2$ Hz/min.⁴⁸⁻⁴⁹ After stabilization, the Z-factor of the QCM was calculated to check that the change in frequency caused by the polymer thin film was within 2% of the uncoated quartz crystal frequency. Under this condition the Sauerbrey relationship is used to convert the change in frequency to a change in mass. The pressure of the viscous flow reactor was kept constant at 1 Torr with a nitrogen gas flow rate of ~300 sccm. To investigate the saturation of the polymer thin films with TMA, an ALD cycle sequence of TMA/N₂/H₂O/N₂ = 0.2/60/0/60 sec was selected. The above sequence was repeated for 10 cycles which corresponded to 10 consecutive exposure cycles (i.e. multi-doses) of TMA. A total purge time of two minutes was chosen to allow reaction by-products and un-reacted TMA to be removed from the reaction chamber between each TMA multi-dose.

ToF-SIMS analysis of PET polymer films. Depth profiles of TMA exposed to PET polymer films were obtained via ToF-SIMS (ION TOF TOF-SIMS 5) with Bi⁺, C₆₀ and Cs⁺ ion

sources. The depth profiles were obtained from thinner PET polymer films ~270nm produced by spin coating a 2 wt. % PET polymer solution onto Si wafers at 5300 rpm. The PET polymer films were exposed to 10 and 50 TMA doses at 100°C and 1 Torr. The TMA infiltrated PET films required no surface treatments prior to ToF-SIMS analysis.

3.3. Results of TMA exposure to polymers

QCM analysis of TMA infiltration in polymers. *In situ* QCM analysis of PA-6, PAA, PET and PMMA films exposed to consecutive TMA doses at 60°C is provided in Figure 3.1 (a). Each exposure cycle consists of TMA doses followed by a purge step using the following sequence TMA/N₂/H₂O/N₂ = 0.2/60/0/60 seconds. It is important to note that the typical water dose has been eliminated from the sequence to probe the saturation behavior of TMA in this work. For convenience in Figure 3.1 (a), the mass gain is shown as a function of both time and the number of TMA doses.

Prior to the first TMA dose, the reaction chamber was purged for 240 seconds with nitrogen gas which provides an inert atmosphere to prevent unwanted chemical reactions with the sample. During the initial purge, the QCM was stable and no chemical reactions took place as indicated by the zero mass gain from $t = -240$ to $t = 0$ seconds. After the initial purge, the specimens were exposed to the first TMA dose at $t = 0$.

As demonstrated in Figure 3.1 (a), PA-6 possesses a high initial absorption of TMA (approx. 2625 ng/cm²) which is followed by desorption of TMA prior to the second TMA dose as reaction by-products and unreacted TMA diffuse out of the film. Desorption of TMA occurs from approximately $t = 240$ to $t = 600$ seconds between the 1st and 6th TMA dose which is preceded by a zero net mass gain from $t = 600$ to $t = 1320$ seconds. This

indicates that successive doses do not influence the total mass gain (approx. 2250 ng/cm² after 10 TMA multi-doses) of TMA in the PA-6 film. In comparison, PAA possesses a low initial mass gain of TMA (approx. 45 ng/cm²). Desorption of TMA between each multidose is not observed over the total time period of multidoses in PAA. Successive doses of TMA after the first dose do not provide a significant contribution to the total mass gain of TMA in PAA (approx. 100 ng/cm²). After TMA multidoses, the reaction chamber was purged for 200 seconds from approximately $t = 1200$ to $t = 1320$ seconds. The total mass gain of TMA in both PA-6 and PAA films remains unchanged during the final purge indicating that the TMA that has reacted stays within the polymer films.

The initial absorption of TMA in PET is approximately 400 ng/cm². Unlike PA-6 and PAA, the PET film loses nearly 60% of absorbed TMA during the 2 minute purge before the second dose. The absorption and desorption behavior of TMA causes a gradual increase in mass uptake of TMA between $t = 240$ and $t = 1320$ seconds, corresponding to 10 consecutive TMA doses. A saturated mass gain is not observed suggesting that PET requires a larger number of multidoses to fully saturate the polymer film. Finally, the mass uptake of TMA in PMMA follows a similar behavior to PET; *i.e. significant desorption of TMA after each dose*. However, the initial mass gain of TMA in PMMA (approx. 200 ng/cm²) is much lower than PET. While successive TMA multidoses are required to increase the total mass gain of TMA in PMMA, the onset of a saturated mass gain of approx. 250 ng/cm² is observed after the 7th TMA dose at approximately $t = 840$ seconds.

In the following sections, TMA exposure is explored at various reactor temperatures to investigate the rate of precursor infiltration over a range of temperatures. Polymers are primarily influenced by temperature due to the relative difference between the surrounding temperature and the glass transition temperature of the polymer. This has a corresponding effect on the re-orientation of polymer chain segments and the free volume of the polymer. Therefore, to understand the growth of inorganic coatings on polymers, the following sections address the rate of infiltration specifically as it relates to polymer physics and polymer chemistry at varied temperatures. To this point, Table 3.1 provides a summary of the chemical structure, glass transition temperature (T_g), melting transition temperature (T_m), and the coefficient of thermal expansion of each polymer investigated in this work.⁴⁷ To analyze the infiltration characteristics of the TMA, *in situ* QCM is utilized to approximate the TMA absorption, desorption and reaction in each polymer film. For clarification, Figure 3.1 (b) shows a QCM time segment clearly indicating the mass uptake behavior of 2 TMA doses exposed to a polymer film. The figure indicates the absorption of TMA at the onset of the first dose followed by desorption of unreacted TMA. Finally, the difference between absorbed and desorbed TMA is referred to as the ‘reacted’ quantity of TMA left inside the polymer film before the next dose. The distinction between absorbed, desorbed and reacted TMA is identified to facilitate the results discussion of the following sections.

Temperature dependent absorption and reaction of TMA in PA-6. PA-6 is a thermoplastic polymer with a glass transition temperature ranging from 40 to 60°C as summarized in Table 3.1. PA-6 has a melting temperature ranging from 220 - 260°C therefore; it was possible to explore the exposure of PA-6 thin films to TMA between the minimum and maximum

operating range of the viscous flow reactor (30°C - 150 °C). Figure 3.2 compares the infiltration of TMA in PA-6 at various reactor temperatures as monitored by *in situ* QCM. Prior to the onset of the first TMA dose, the reaction chamber was purged with N₂ for 240 seconds to prevent undesirable reactions with the substrate and to minimize the absorption of water impinged on the surface of the PA-6 polymer film. At $t = 0$ the PA-6 film was exposed to the first 0.2 sec dose of TMA.

Figure 3.2 shows that the absorption of the first dose of TMA increases from 1250 ng/cm² to 2625 ng/cm² between 30°C and 60°C respectively. However, as temperature increases, the initial absorption of TMA decreases to 750 ng/cm² at 100°C and further decreases to 250 ng/cm² at 150°C. As shown in Figure 3.3, approximately 375 ng/cm² of TMA desorbs from the PA-6 film between $t = 0$ to $t = 360$ seconds (*i.e. between the 1st and 4th TMA dose*) at 60 °C however, at 30°C there is only slight desorption of TMA. Moreover, as the temperature increases above 60°C, it is also evident that desorption of TMA after the first dose significantly reduces. As temperature increases from 60°C to 150°C, the exposure of PA-6 to successive TMA doses does not influence the total mass gain of TMA as demonstrated by the zero net increase in mass uptake throughout the time frame of the experiments. However, at 30°C it is clear that approximately 4 TMA doses are required to achieve a saturated mass gain as shown in Figure 3.2 between $t = 0$ and $t = 480$ seconds. As temperature increases above 60°C, reductions in absorbed TMA and desorbed TMA correspond to a decrease in the total mass uptake of TMA in PA-6. It is interesting to note that the total mass uptake of TMA in PA-6 at 30°C falls between the total mass uptake of

TMA achieved at 60°C and 100°C. At all exposure temperatures, the total amount of TMA left inside the film after 10 consecutive doses is retained by the polymer film.

Temperature dependent absorption and reaction of TMA in PAA. PAA is the polymer of acrylic acid which possesses a carboxyl group in its side chain as shown in Table 3.1. Therefore, PAA contains -OH and carbonyl groups that have both been shown to be reactive towards TMA. PAA has a higher glass transition temperature of 106°C and a melting temperature of 179°C. Therefore, PAA exposure to TMA was explored in the temperature range between 30°C - 150 °C. Figure 3.3 compares the exposure of 10 TMA multidoses in PAA at various reactor temperatures as monitored by *in situ* QCM. In contrast to PA-6, PAA possesses significantly lower mass gains of TMA, independent of temperature.

Figure 3.3 indicates that there is not a significant correlation between temperature and the infiltration behavior of TMA in PAA. However, it is interesting to observe that a higher total mass gain of TMA is achieved at 30°C. The mass uptake of the first TMA dose at each exposure temperature is approximately 40 ng/cm². Since PAA is known to absorb large quantities of water, each polymer film was heat treated to remove absorbed water prior to each experiment. If there were significant quantities of pre-absorbed water contained in each polymer film, it would be expected that the first TMA dose at each reactor temperature would be much higher from the strong reaction between TMA and water. Therefore, the higher mass uptake at 30°C may be caused by condensation of precursor at the lowest reactor temperature.

Temperature dependent absorption and reaction of TMA in PMMA. PMMA has a lower melting temperature of 130°C compared to previously analyzed polymers therefore; TMA exposures to PMMA polymer thin films were analyzed between 30°C and 120 °C. Figure 3.4 (a) compares the mass uptake of TMA multidoses in PMMA at various reactor temperatures via QCM. As shown in Figure 3.4 (a), PMMA polymer films possess lower absorption of TMA and lower total mass uptakes compared with PA-6. However, the absorption of TMA and subsequent desorption during each purge step between doses increases as temperature increases to 100°C and 120°C. Despite an increase in TMA absorption with temperature, TMA mass uptake at higher reactor temperatures of 100°C and 120°C is not retained within the polymer films during the final purge between $t = 1080$ to $t = 1320$ seconds. As shown in Figure 3.4 (a), the final mass uptake of TMA decreases to approximate values between 100 and 250 ng/cm² over all exposure temperatures during the final purge.

To explore the infiltration behavior of TMA in PMMA in more detail, Figure 3.4 (b & c) show the absorbed and reacted TMA per dose as temperature varies, respectively. Figure 3.4 (b) confirms that as temperature increases the absorption of TMA also increases. Furthermore, the absorption of TMA is relatively constant for each successive dose at all exposure temperatures. Absorption of TMA ranges from approximately 50 ng/cm²/dose at 30°C to 750 ng/cm²/dose at 120°C. Figure 3.4 (c) shows that the most significant contribution to the total mass gain of reacted TMA retained in the polymer film at 100°C and 120°C is achieved during the first dose of TMA. The mass uptake of reacted TMA is negligible after the 2nd and 6th doses at 120°C and 100°C, respectively, indicating that successive doses do not have a significant impact on the final mass uptake of TMA in PMMA at these

temperatures. The mass uptake per dose at 30°C and 60°C gradually decreases however, a saturated mass gain is not observed at 60°C. The low reacted mass uptake per dose of TMA indicates that the majority of absorbed TMA subsequently desorbs from the polymer film at all exposure temperatures examined.

Figure 3.5 (a) compares the mass uptake of TMA multidoses in a series of acrylic polymers at a fixed reactor temperature of 60°C. As shown in Figure 3.5 (a) PMMA possess lower absorption compared with PPMA and PBMA. Figure 3.5 (b) shows that the absorption of TMA per dose ranges from approximately 100 ng/cm²/dose in PMMA to 750 ng/cm²/dose in PBMA at 60°C. Finally, the absorption of TMA is relatively constant for each successive dose of each specimen from the series of acrylic polymer films.

Temperature dependant absorption and reaction of TMA in PET. Figure 3.6 (a) shows the mass uptake behaviour of TMA in PET at reaction temperatures from 30°C to 150°C. Figure 3.6 (a) demonstrates that the total mass gain of 10 TMA multidoses in PET increases from less than 200 ng/cm² at 30 °C to 3750 ng/cm² at 100°C. In comparison to PA-6, PAA and acrylic films, PET achieves a much greater total mass gain of TMA after 10 TMA doses at 100°C. However, the final mass gain of 10 TMA doses decreases to approximately 1750 ng/cm² at 150°C. There is a corresponding relationship between absorbed TMA and temperature as the amount of the absorbed TMA increases between 30°C and 100°C, followed by a decrease in TMA absorption at 150°C. While significant quantities of TMA desorbs from the PET polymer films at reactor temperatures between 60°C to 100°C, the largest desorption is observed at 100°C.

To explore the infiltration behavior of TMA in PET in more detail, Figure 3.6 (b & c) shows the absorbed and reacted TMA per dose as temperature varies, respectively. In general, Figure 3.6 (b) confirms that the absorbed TMA per dose increases as temperature increases from 30°C to 100°C with a corresponding decrease in absorption per dose at 150°C. As shown in Figure 3.6 (b) the absorption of TMA per dose at 30°C and 60°C remains constant however, at 150°C and 100°C there is a gradual increase in absorbed TMA as the number of doses increases.

Figure 3.6 (c) shows that the reacted TMA per dose retained within the PET thin film increases as temperature increases from 30°C to 100°C with a subsequent decrease in reacted mass uptake per dose at 150°C. The reacted mass uptake per dose of TMA remains constant over the 10 consecutive doses at all exposure temperatures. This indicates that within the temperature range of 30°C to 150°C, a saturated mass gain is not observed within the 10 exposure cycles employed in this work.

To observe a saturated mass gain, a thinner PET polymer film ~270nm was exposed to a larger number of TMA doses. Figure 3.7 (a) shows the infiltration of 100 consecutive TMA doses in PET at 100°C. This temperature was selected for the analysis since the infiltration behavior indicates that the largest absorption and reacted mass uptake of TMA is achieved at 100°C. As shown in Figure 3.7 (a) there is a sharp increase in the mass uptake of TMA between $t = 0$ and $t = 3000$ seconds (i.e. 1st and 25th TMA dose). Following $t = 3000$ seconds, the mass uptake gradually plateaus to a total mass gain of approximately 8625 ng/cm². Figure 3.7 (b) shows the absorption per dose and reacted TMA per dose retained

within the polymer film over the 100 consecutive TMA doses. Between 0 and 10 TMA doses, there is a gradual increase in absorbed and reacted TMA per dose, which is consistent with the infiltration behavior shown in Figure 3.6 (b) at 100°C. After 10 TMA doses, the absorption of TMA and reacted TMA per doses gradually decrease towards zero by the 100th TMA dose.

Furthermore, the exposure of 10 and 50 TMA doses into 270nm thick PET films on Si wafers was investigated using a ToF-SIMS. A thinner film and 50 TMA doses instead of 100 TMA was chosen for the analysis as a compromise for the total sputter time of the experiment. Figure 3.8 shows ToF-SIMS depth profiles indicating C⁺, Al⁺ and Si⁺ markers attributed to the PET polymer film, alumina (from TMA) and Si substrate, respectively. The data in Figure 3.8 shows the natural logarithm of the ion intensity from each marker. It is important to note that the data does not correspond to the concentration of TMA in the polymer film but is representative of the ion yield during the sputtering process. The slightly higher intensities of the Al⁺ marker for both 10 and 50 TMA doses at the start of sputtering was attributed to charging on the surface of the film. The gradual increase in intensity of the Si⁺ marker between a depth of 150nm and 300nm for 10 TMA doses and 175 and 275nm for 50 TMA doses is due to the uneven surface of the PET films causing parts of the film to sputter at different rates.

3.4. Discussion

Free volume theory of precursor infiltration. The absorption of TMA into each polymer chemistry provides an interesting insight into the absorption behavior of organometallic

precursors in polymer films. Clearly, a significant driving force behind the growth mechanism of inorganic coatings in certain polymers is the ability for organometallic precursor molecules to diffuse into the polymer. For PA-6, PET and PMMA, *in-situ* QCM analysis shows that TMA absorption increases with temperature. However, it is interesting to observe that in PA-6 there is an increase in TMA absorption from 30°C to 60°C, followed by a significant decrease in absorption at 100°C and 150°C. In a similar way, absorption in PET increases from 30°C to 100°C before decreasing at 150°C.

Herein, the influence of temperature on the free volume of the polymer film is used to describe the variation in absorption of TMA as temperature increases. The total specific volume pervaded by a system of polymer chains can be split up into two sections: (i) the volume that is physically occupied by each constituent atom that makes up the polymers long chains and (ii) the unoccupied volume that is typically called the polymer free volume.⁵⁰ As a polymer is cooled, insufficient thermal energy reduced polymer chain mobility which produces the glassy state. The temperature at which the polymer changes from a flexible rubbery material to a brittle glassy material is named the glass transition temperature, T_g . The polymer chain mobility is influenced around T_g . Below T_g the polymer chain mobility is decreased resulting in a reduction in free volume. Above T_g the mobility is increased corresponding to an increase in polymer free volume which causes a subsequent increase in specific volume of the polymer.⁵⁰ The rate of specific volume increase is determined by the thermal expansion coefficient of the polymer, *i.e. the slope of the specific volume vs. temperature curve*. The values stated in Table 3.1 for the polymers studied in this work are average values measured over broad temperature ranges. The difference in values is dictated

by the structure of each polymer. In general, rigid polymer repeat units such as PET, or highly crystalline polymers possess lower thermal expansion coefficients due to reduced polymer chain mobility. While thermal expansion coefficient is an important parameter when considering the temperature dependence of polymer properties, in this work we demonstrate that the T_g of each polymer relative to the temperature of the reactor has a significant impact on the absorption of TMA.

We continue the discussion by considering a simple jump diffusion model. The motion of a single solute molecule from one region of the polymer to an adjacent location depends on the presence of free volume voids large enough to accommodate the solute molecules. This is the theory behind the free volume model of diffusion developed by Turnbull and Cohen in 1959 and serves as the foundation for more sophisticated free-volume models of diffusion discussed in more detail elsewhere.^{50, 51} The theory states that the diffusion coefficient is dependent on the probability of forming a critical free volume void in an adjacent location that is large enough to accommodate a small solute molecule. The most dramatic changes in the diffusion coefficient of small molecules through a polymer have been observed at T_g . Below this temperature, the diffusion coefficient is greatly reduced however at T_g ; studies have shown that there is a sharp increase in the diffusion coefficient.⁵⁰ This is attributed to the temperature dependent increase in free volume and re-distribution as larger polymer chain segments are able to move and form sufficient voids to accommodate the motion of diffusing molecules.

We propose that the lower mass gains of TMA in PA-6, PET and PMMA films at low reactor temperatures are attributed to diffusion of TMA into the polymer films below T_g . As a result there is a reduced probability of forming a free volume void large enough to accommodate the size of the TMA molecules due to the lower polymer chain mobility. Hence, the diffusion coefficient of the TMA molecules through the sub-surface of the polymer films are significantly reduced resulting in lower absorption and mass gains. Since the diffusion coefficient is proportional to the probability of forming a critical free volume void, higher temperatures are required to increase the mobility of the polymer chains, forming larger free volume voids to accommodate the diffusing species. Therefore, the increase in absorption of TMA in the polymer films is caused by an enhanced diffusion coefficient influenced by the polymer film free volume increase in the region of T_g .

The free volume theory is further explored via TMA exposure to a series of acrylic polymer films at 60°C as shown in Figure 3.5. Acrylic polymers are characterized by a pendant group consisting of an acryl group attached to a methyl group. The length of the pendant group can be changed by adding additional $-CH_2-$ groups. This makes the polymer more flexible which has a resultant effect on the glass transition temperature of the polymer. The T_g 's of PMMA, PPMA and PBMA are approximately 115°C, 35°C and 15°C respectively. Figure 3.5 (b) shows that the absorption of TMA is less in PMMA, which has the highest T_g , in comparison to both PPMA and PBMA. At 60°C the temperature of the reactor is above the T_g of both PPMA and PBMA and below the T_g of PMMA. Therefore, the free volume of PMMA is lower than the free volume of PPMA and PBMA. Consequently, the increase in absorption of TMA in PBMA and PPMA polymer films is caused by an

enhanced diffusion coefficient influenced by the polymer film free volume increase while the lower absorption of TMA in PMMA is caused by a reduced diffusion coefficient due to a reduced free volume. Not only does this reinforce the importance of polymer T_g on the infiltration of organometallic precursors, but the relationship shown in Figure 5 also indicates the importance of the reactor temperature relative to the T_g of the polymer.

The Arrhenius relationship predicts that an increase in temperature causes an increase in the diffusion coefficient of the respective gas. For non-reactive polyolefins, studies have shown that TMA mass increase scales with higher reactor temperatures as a result of thermal expansion.¹⁴⁻¹⁶ However, the mass uptake of TMA begins to reduce after a temperature associated with the peak mass gain of TMA *i.e.* 60°C for PA-6, 100°C for PET and 120°C for PMMA. The increase in temperature of ‘peak’ absorption is related to the slower reaction between TMA and PET. Therefore, it is reasonable to assume that the low mass gain of TMA in PAA, independent of temperature, is attributed to a faster surface reaction that prevents uptake of successive precursor dose before the polymer film has had time to reach T_g (106°C) causing an increase in free volume. This states that for infiltration in reactive polymers as demonstrated in this work, one must consider the effect of temperature on the balance between both chemical reaction and diffusion. Furthermore, in comparison to PA-6 a significant increase in absorbed TMA is not observed in PET and PMMA until higher reactor temperatures as shown in Figures 3.6 (b) and 4 (b) *i.e.* 60°C to 100°C for PET and 60°C to 120°C for PMMA. This is attributed to differences in T_g between each polymer chemistry as shown in Table 3.1. PET and PMMA have higher T_g 's in comparison to PA-6 therefore; higher temperatures are required before a considerable increase in absorption is observed.

This further indicates the importance of the reactor temperature relative to the T_g of the polymer.

Infiltration behavior of TMA in PA-6 and PAA. The large mass gain of TMA in PA-6 is representative of diffusion of precursor molecules into the subsurface of the polymer film. In contrast, the much lower mass gain of TMA in PAA is representative of precursor reactions that occur predominantly on the surface of the polymer due to larger surface concentrations of functional groups.^{40, 43} This is consistent with other studies in which QCM mass uptake behaviour is calibrated in terms of TMA monolayers.⁴⁴ Lower mass uptake corresponds to fewer precursor monolayers indicating near surface to surface growth, while higher mass uptake corresponds to a larger number of precursor monolayers signifying subsurface infiltration.

Studies have also shown that the thickness of the hybrid (organic-inorganic) coatings formed within PA-6, after sequential exposures to TMA and water, decreases as temperature increases.⁵² This is consistent with the QCM mass uptake data shown in Figure 3.2 of this study. Since the mass uptake of TMA is dependent on the competition between precursor diffusion and chemical reaction, increasing temperature increases the extent of reaction between TMA and PA-6. This eliminates diffusing TMA from the concentration gradient within the polymer film more rapidly as temperature increases. Subsequently, available reaction sites throughout the diffusion length of TMA in PA-6 are consumed creating a more dense hybrid layer within narrower sub-surface regions of the polymer. This prevents the

diffusion of successive TMA exposures resulting in shorter nucleation periods, lower mass uptake of TMA, and thinner hybrid coatings as shown in Figure 3.9.

Fundamental chemical reactions between precursors and polymer functional groups have been explored previously using in-situ FT-IR by Gong et al.⁴⁶ The removal of C=O stretching modes indicates that TMA attacks nucleophilic carbonyl groups along the polymer backbone of polyesters and polyamides. This results in the formation of R-O-Al(CH₃)₂ units where R is the respective polymer repeat unit. Intra-chain hydrogen bonds form within PA-6 due to the orientation of carbonyl and N-H groups in adjacent chains. A study exploring the incorporation of gallium trichloride (GaCl₃) in PA-6 within a common solvent suggested that the Ga nucleus coordinates with oxygen of the carbonyl group.^{53, 54} Although this work was carried out in solution, it proposes questions as to whether TMA coordinates with the carbonyl group of PA-6 in the vapor phase or forms a Lewis acid–base complex resulting in R-O-Al(CH₃)₂ units covalently bonded to the PA-6 backbone as shown in Figure 3.9.

In comparison, PAA has a highly hydroxylated surface and is much more favorable to TMA reaction. The diffusion of the TMA would therefore be limited by the enhanced reaction kinetics at higher (and lower) temperatures for PAA. This mechanism is consistent with the results that show that PAA mass increase is much lower than PA-6 and is independent of TMA exposure temperature.

Infiltration behavior of TMA in PET. The absorption and significant desorption of TMA in PET after each TMA dose, indicates a slower chemical reaction resulting in longer nucleation

periods. The slower reaction in PET may be caused by the proximity of the carbonyl to an oxygen atom within the ester group. Since oxygen is an electron withdrawing group,⁵⁵ this could make the carbonyl group less Lewis basic as electrons are drawn from the π bond of the carbonyl group. This is in comparison to PA-6 in which the carbonyl group is situated next to an $-\text{NH}-$ group which is more electron donating⁵⁵ making the carbonyl group more Lewis basic and thus, more reactive with TMA. Once TMA has reacted with PET, proposed modes in which TMA can attach itself to the polymer backbone are shown in Figure 3.9 (i) TMA reacts with the carbonyl group forming $\text{R-O-Al}(\text{CH}_3)_2$ units covalently bonded to the PET backbone, and (ii) TMA reacts with carbonyl groups in adjacent chains forming $\text{R-O-Al}(\text{CH}_3)\text{-R}$ units.

As shown in Figure 3.7 (a), a larger number of consecutive TMA doses are required to observe a saturated mass gain in PET using a TMA multidosing scheme. In comparison to PA-6, the analysis indicates that the slower reaction between TMA and PET retains access to potential reactive sites and facilitates the diffusion of successive precursor doses. Therefore, the balance between TMA diffusion and reaction in PET suggests that the infiltration of TMA can influence the bulk of the PET polymer film as shown in Figure 3.9. The bulk infiltration of TMA in PET is clarified by the ToF-SIMS data shown in Figure 3.8 (a & b). The Al^+ marker of TMA intersects the Si^+ marker of the Si substrate indicating that TMA has infiltrated the entire thickness of the polymer film. The data also shows the Al^+ marker of TMA conformally maps the C^+ marker of PET throughout the depth of the film suggesting that TMA and hence, alumina is homogeneously distributed throughout the polymer film. This explains our previously unsuccessful attempts to obtain both TEM cross-sections and

EDX spectra of TMA exposure in PET. The concentration of alumina in the homogenous structure is too low for detection via EDX or to cause density changes in the film that can be detected by TEM. The most interesting observation from the ToF-SIMS depth profile is the fact that TMA infiltrates the entire thickness of the film independent of the number of doses. The bulk infiltration of TMA in PET has been shown in other studies via SEM analysis however; much larger dose times of TMA were required to observe the result.⁴⁵ It is interesting to note that in traditional polymer processing techniques such as reactive dyeing, salts are added to the dye bath to delay chemical reactions between polymer functional groups and the dye molecules to promote the diffusion of the dye molecules into the bulk of the polymer.⁵⁶ In this case, PET is already inherently less reactive towards TMA thus promoting diffusion.

The polymer repeat unit of PET has an aromatic-aliphatic chemical structure, as shown in Table 3.1. TMA is soluble in aromatic, saturated aliphatic and cycloaliphatic hydrocarbons therefore, it is likely that there is a strong chemical solubility of TMA in PET. Good solvents promote strong interactions between polymer chain segments and the solvent molecules which causes the uncoiling of the polymer chains and swelling of the polymer. Consequently, the gradual increase in absorbed TMA per dose as shown in Figure 3.6 (b) at 100°C and 150°C is attributed to swelling of the polymer film promoting the absorption of more TMA as the number of TMA doses increases. The effect of swelling on the absorption of TMA is more apparent at 100°C and 150°C since more reacted TMA is retained within the polymer film compared with lower temperatures. The same behaviour is observed in Figure 3.7 (b) between 1 and 10 TMA doses however, after approximately 10 TMA doses the

absorption of TMA per dose decreases. Figure 3.7 (b) also shows that there is a corresponding decrease in the mass uptake of reacted TMA per dose after the 10th dose. We attribute the decrease in reacted TMA per dose after the 10th TMA dose to the consumption of potential reactive sites within the polymer film. Therefore, the decrease in absorbed TMA is likely due to the gradual densification of the polymer film as more TMA is retained per dose which confines the infiltration of more TMA. Since the ToF-SIMS depth profiles indicate that TMA infiltrates the entire thickness of the film independent of the number of doses, we anticipate that the first dose of TMA can diffuse along the entire thickness of the film consuming potential reactive sites throughout the volume of the film. Therefore, additional doses simply consume any available reactive sites eventually leading to the saturation of the polymer film.

Infiltration behavior of TMA in PMMA. Similarly, the absorption and significant desorption of TMA in PMMA after each TMA dose, indicates a slower chemical reaction. However, the reacted TMA retained in the PMMA film is much lower than PET. Despite the increase in absorbed TMA per dose as temperature increases, the lower mass uptake of reacted TMA per dose indicates that the majority of absorbed TMA diffuses out of the PMMA polymer film; this is consistent at both low and high temperatures. Furthermore, as shown Figure 3.5 (c), the PMMA film saturates with a lower number of TMA doses. Therefore, the nucleation period in PMMA compared with PET is much shorter. This indicates that TMA infiltration of PMMA does not have the potential to influence the bulk of the polymer instead, reacting and nucleating within the near surface of the polymer film.

It is interesting to observe that, unlike PA-6 and PET, successive doses of TMA absorb into the PMMA film at a constant mass uptake per dose even after the onset of a saturated mass gain has been achieved. This can be observed over the temperature range explored in this work. We relate the constant absorption of TMA after a saturated mass gain, and the much lower reacted mass gain compared with PET to the polymer film-substrate interaction after the spin coating process and the low reactivity of TMA with PMMA, respectively. Keddie et al., showed that there is a low interfacial energy between PMMA and a gold (Au) surface.⁵⁷ Furthermore, the study showed that the T_g at the free surface is lower than the T_g within the bulk of the film. This is confirmed by the study of Xia et al., who used computer simulations to explore the effect of polymer free surface and substrate effects on the T_g of polymer films.⁵⁸ The simulations confirmed that low interfacial energies at the interface of the polymer film and supporting substrate causes a gradient in the T_g of the polymer film. Therefore, we propose that TMA diffuses unrestricted through the free surface, *with lower T_g and higher free volume*, into the sub-surface of the PMMA polymer film, *with higher T_g and reduced free-volume*. Consequently, TMA reacts with functional groups in more dense regions of the polymer as shown in Figure 10. The result is that the reacted TMA consumes reactive sites and forms a barrier to reaction of successive TMA doses. However, the open structure of the free surface continues to promote the diffusion and absorption of TMA into the sub-surface of the polymer film. This is our initial understanding of the growth mechanism of the less explored acrylic polymer chemistries. Therefore, we acknowledge that further experiments are required to fully understand the infiltration mechanism of precursors in these polymers.

Significance of this work to other studies. Wilson et al. related the retention of TMA after chemical reaction to the chemical solubility of TMA within the polymer film *i.e. non-polar TMA retained in more non-polar hydrophobic polymers such as PE.*⁴⁴ However, in this study, we show that the retention of TMA occurs within polar PA-6 and PAA polymers. Therefore, in PAA we attribute the retention of TMA to the faster reactions between the precursor molecule and functional groups of the polymer. Similarly in PA-6, retention of TMA is attributed to either a faster reaction forming a Lewis acid-base complex or coordination with the carbonyl group.

Finally, in-situ FT-IR data can also be calibrated in terms of TMA monolayers which highlights differences in TMA absorption and the ‘extent’ of reaction.⁴⁶ Analysis shows a lower extent of reaction in both inert polymers and polymers containing high concentrations of surface functional groups in contrast to higher extents of reaction observed in polyamides and polyesters. The latter is consistent with QCM studies and TEM analysis that show a higher extent of reaction due to sub-surface precursor diffusion. However, the former cases suggest that a lower extent of reaction can either be caused by low reactivity between precursor and polymer, or a relatively high reactivity leading to rapid coating formation. In contrast, QCM can provide direct evidence of the unique nucleation behavior of different polymers by deconvoluting the effect of absorption, desorption and reacted components of precursor infiltration within the polymer films.

This work demonstrates that coating morphologies and thicknesses can be controlled by both polymer structure and process conditions such as temperature. With a greater

understanding of reactive vapor infiltration of precursors into polymers, the choice of polymer substrate and process parameters can be tailored for specific applications depending on whether enhanced surface, sub-surface or bulk properties are required. This work also demonstrates that the formation of surface and sub-surface coatings produced by certain polymer/precursor interactions *i.e* PA6/TMA, may be favoured by typical ALD processing. In comparison, the bulk infiltration and slower absorption of TMA in polymers such as PET may benefit from modified processes that promote reactive vapor infiltration *i.e sequential vapour infiltration (SVI)*.^{45, 59, 60}

3.5. Conclusion

In this study, the infiltration of TMA into the sub-surface of PA-6, PAA, PET and acrylic thin films was investigated via *in-situ* QCM analysis. The saturation behaviour at varying reactor temperatures was explored by exposing the polymer to multiple doses of TMA using an ALD sequence with an eliminated water dose and extended purge time. The data indicates that TMA absorption is promoted as temperature increases. The absorption of more TMA at higher temperature is related to a polymer free volume theory of diffusion. At higher temperatures above the T_g of the polymer, an increase in free volume promotes the infiltration of precursor. However, the absorption of TMA peaks at a certain temperature which is followed by a decrease in absorption as temperature increases. This observation is attributed to a faster reaction that forms more dense sub-surface layers of reacted TMA which hinders the diffusion of additional TMA molecules. While the decrease of TMA mass uptake at higher reactor temperatures is consistent with other studies, this work also provides

insight into the infiltration mechanism of organometallic vapors into polymers below T_g . The analysis of polymer films shows that the mass uptake of TMA decreases at lower reactor temperatures below the T_g of the respective polymer. An explanation for this phenomenon is presented that suggests that the diffusion is inhibited below the glass transition temperature of the polymer due to the corresponding reduction in free volume. This work has important implications on the introduction of hybrid material properties to polymer film and fibrous systems which is of increasing interest due to the ability to develop flexible materials with unique mechanical, electrical, and optical behavior.

Chapter 3 Figures:

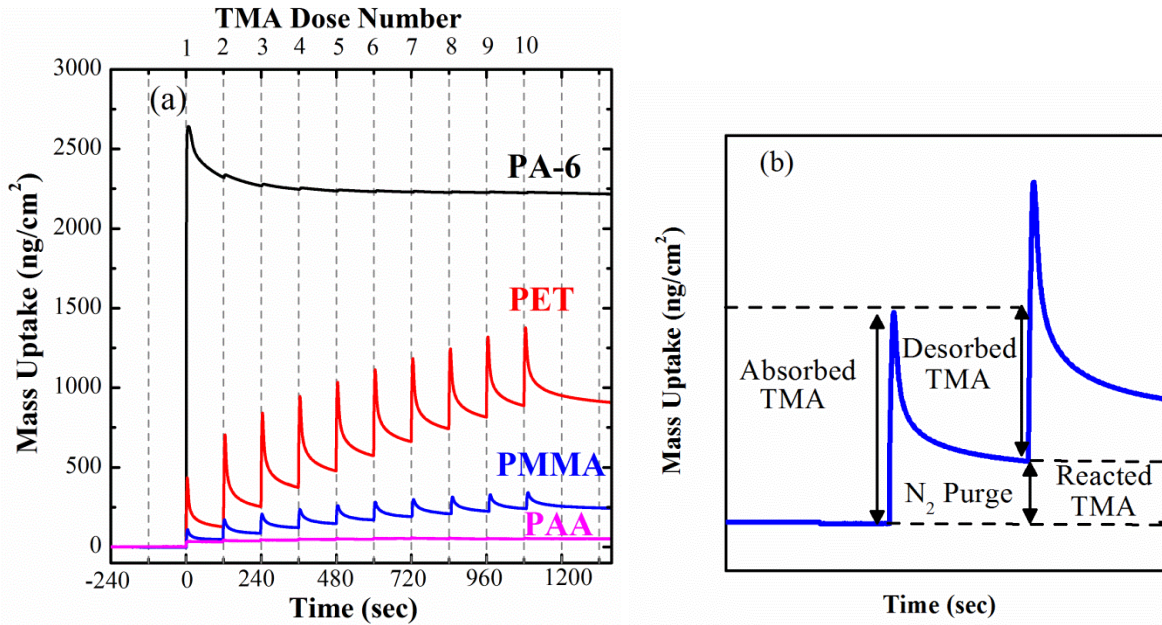
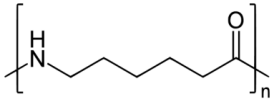
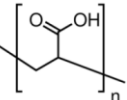
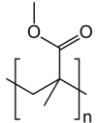
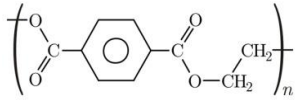


Figure 3.1. (a) *In-situ* QCM analysis of ten consecutive TMA multi-doses onto PA-6, PET, PMMA and PAA polymer films at 60 °C. A TMA multidosing scheme was created by programming the reactor to a typical ALD cycle sequence with an eliminated water dose. The TMA multidose cycle sequence in this work follows TMA/N₂/H₂O/N₂ = 0.2/60/0/60 seconds. The polymer films were thermally equilibrated to the reactor temperature until the change in frequency recorded by the QCM was approx ±0.2Hz over a period of 60 sec. Prior to the first TMA exposure at t=0, the reaction chamber was purged with N₂ for 240 sec. For clarification, (b) indicates absorbed TMA and reacted TMA retained within a polymer film during 2 doses of TMA following a multidosing scheme.

Table 3.1. Thermal properties of polymers examined in this work including⁴¹: glass transition temperature (T_g); melting temperature (T_m) and coefficient of thermal expansion (α). The repeat unit structure of each polymer is also provided to highlight variations in functional groups. T_m values were used to determine exposure temperature ranges for each polymer.

Polymer	Structure	T_g ($^{\circ}\text{C}$)	T_m ($^{\circ}\text{C}$)	α ($^{\circ}\text{C}^{-1}$)
PA-6		40-60 (dry)	220-260	$0.83-0.93 \times 10^{-4}$
PAA		106	179	N/A
PMMA		105-120	130	2.5×10^{-4}
PET		60-85	245-265	1.7×10^{-5}

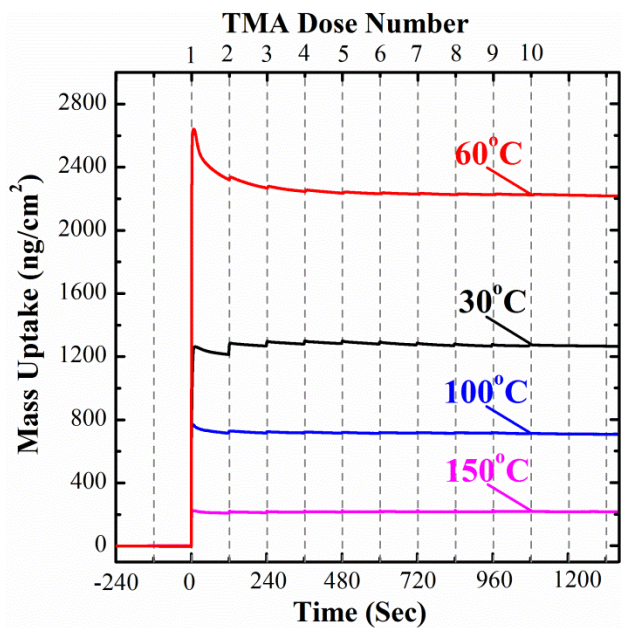


Figure 3.2. *In-situ* QCM analysis of ten consecutive TMA multi-doses onto PA-6 indicating the saturation behavior of PA-6 between 30°C and 150°C.

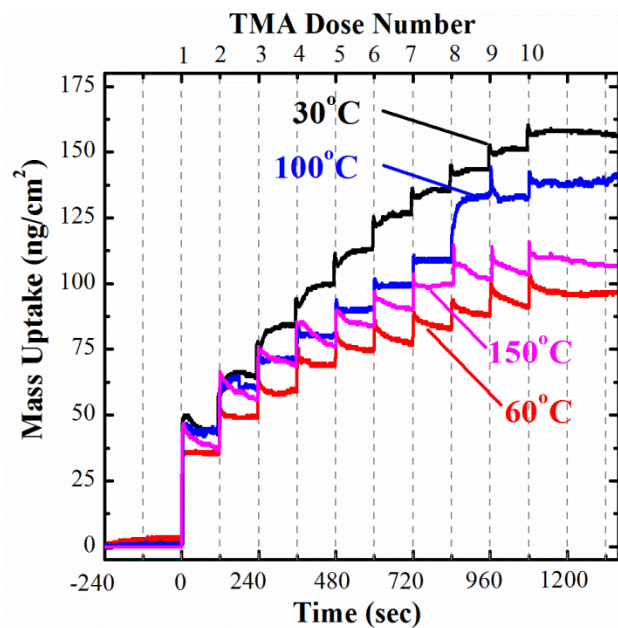


Figure 3.3. In-situ QCM analysis of ten consecutive TMA multi-doses onto PAA indicating the saturation behavior of the polymer film between 30°C and 150°C.

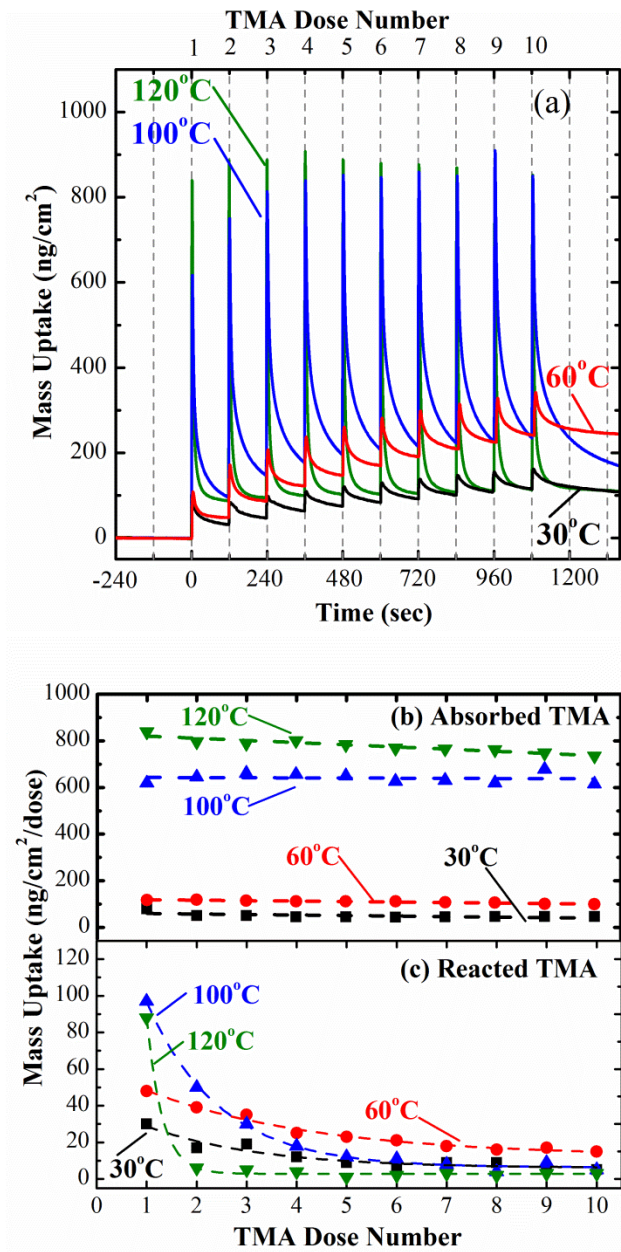


Figure 3.4. (a) In-situ QCM analysis of ten consecutive TMA multi-doses onto PMMA indicating the saturation behavior of the polymer film between 30°C and 120°C. A lower maximum exposure temperature was selected in comparison to other polymer chemistries due to the melting temperature of PMMA at 130°C. (b & c) The infiltration of TMA in PMMA is explored in more detail by separating the absorbed and reacted components of the TMA mass uptake behavior from Figure 4. (a)

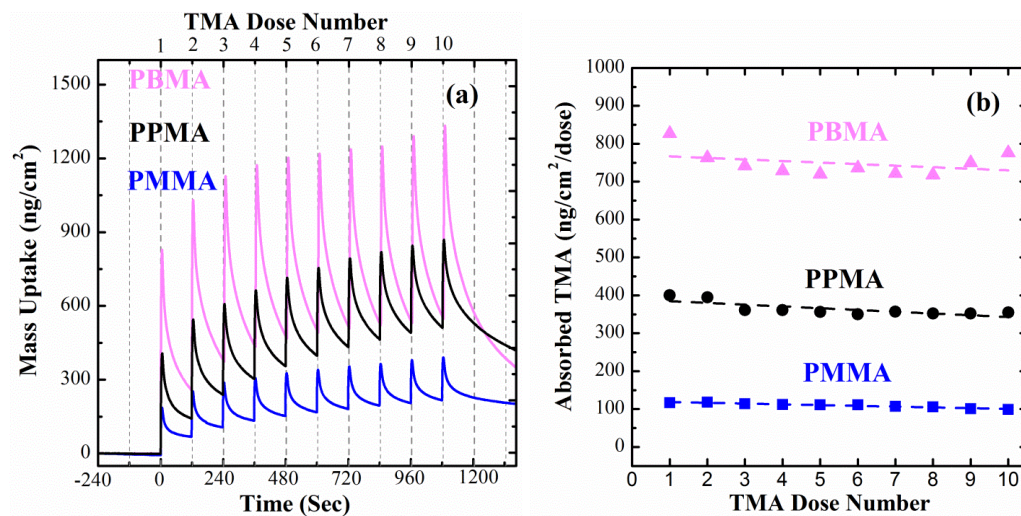


Figure 3.5. (a) In-situ QCM analysis of ten consecutive TMA multi-doses into a series of acrylic polymer films at 60°C. The length of the pendant group increases from PMMA to PBMA as the addition of C-H groups increases. This has an effect on the T_g of each polymer film which varies from 115°C for PMMA to 15°C for PBMA. **(b)** The infiltration of TMA is explored further by investigating the absorbed TMA per dose of each polymer in the series.

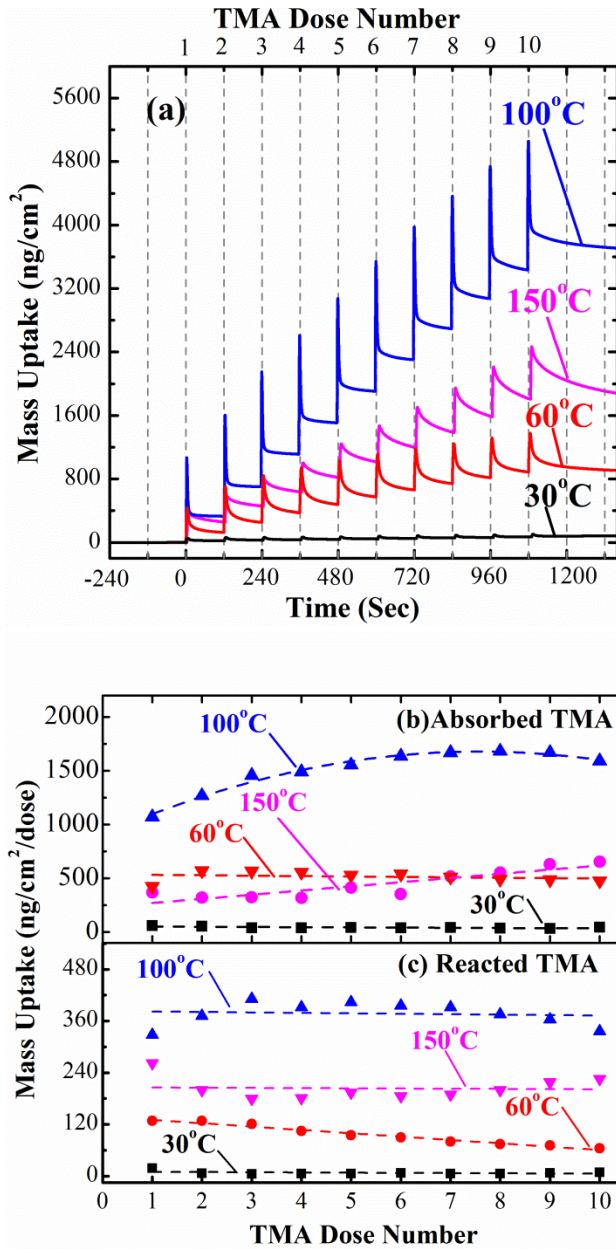


Figure 3.6. (a) In-situ QCM analysis of ten consecutive TMA multi-doses in PET between 30°C and 150°C. The data indicates that at higher reactor temperatures, a saturated mass gain is not observed within the time frame of the experiments. (b & c) The infiltration of TMA in PET is explored in more detail by separating the absorbed and reacted components of the TMA mass uptake behavior.

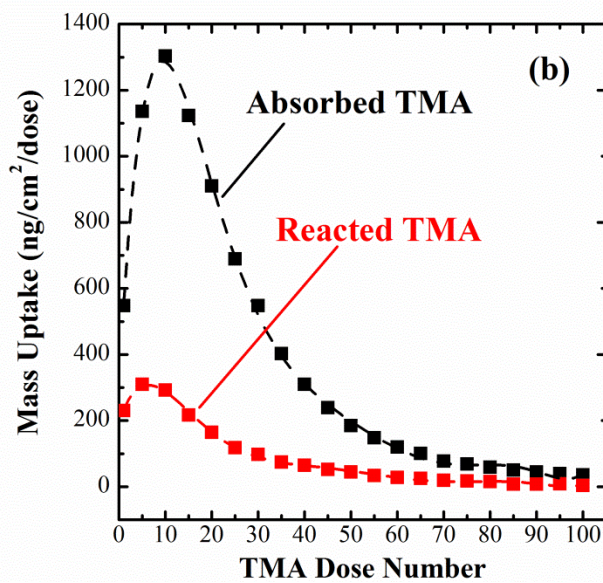
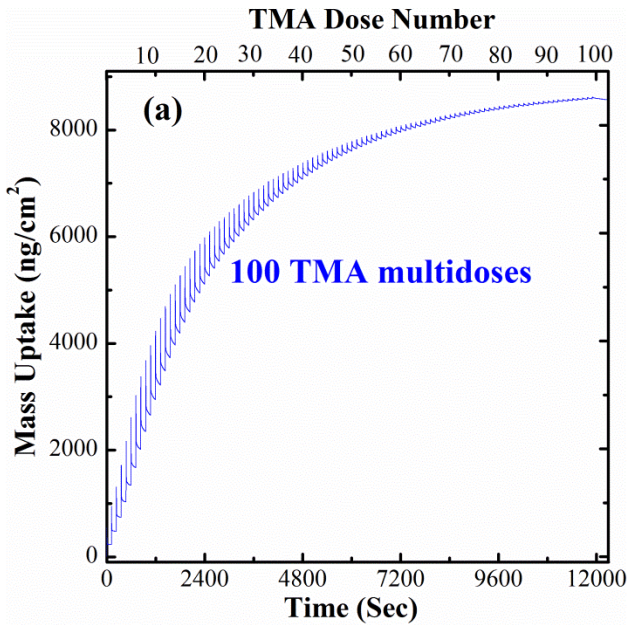


Figure 3.7. (a) *In-situ* QCM analysis of 100 consecutive TMA multi-doses onto PET thin at 100 °C. An exposure temperature of 100 °C was selected since the greatest mass gain, as shown in Figure 6, was achieved at this temperature. The data proves that a significantly larger number of TMA doses are required to saturate a PET film. (b) The infiltration of TMA in PET is explored in more detail by separating the absorbed and reacted components of the TMA mass uptake behavior.

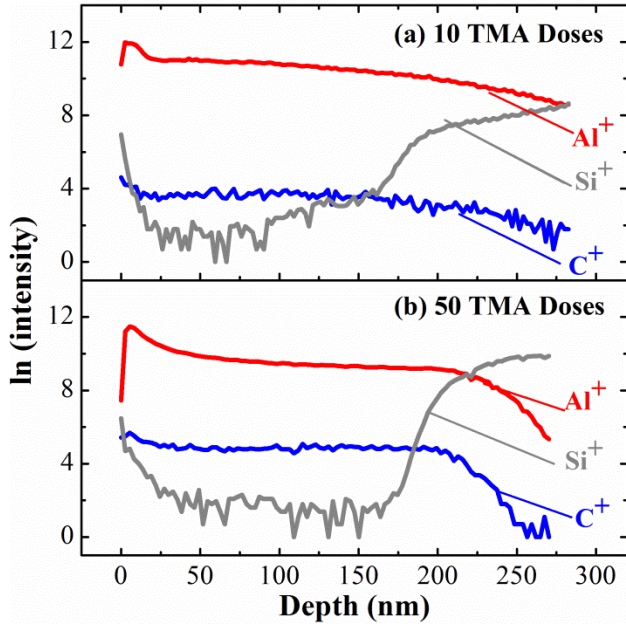


Figure 3.8. ToF-SIMS depth profiles are used to elucidate the bulk infiltration of TMA in PET at 100°C after (a) 10 TMA doses and (b) 50 TMA doses. The Al^+ , Si^+ and C^+ markers represent TMA, Si wafer support and PET polymer film, respectively.

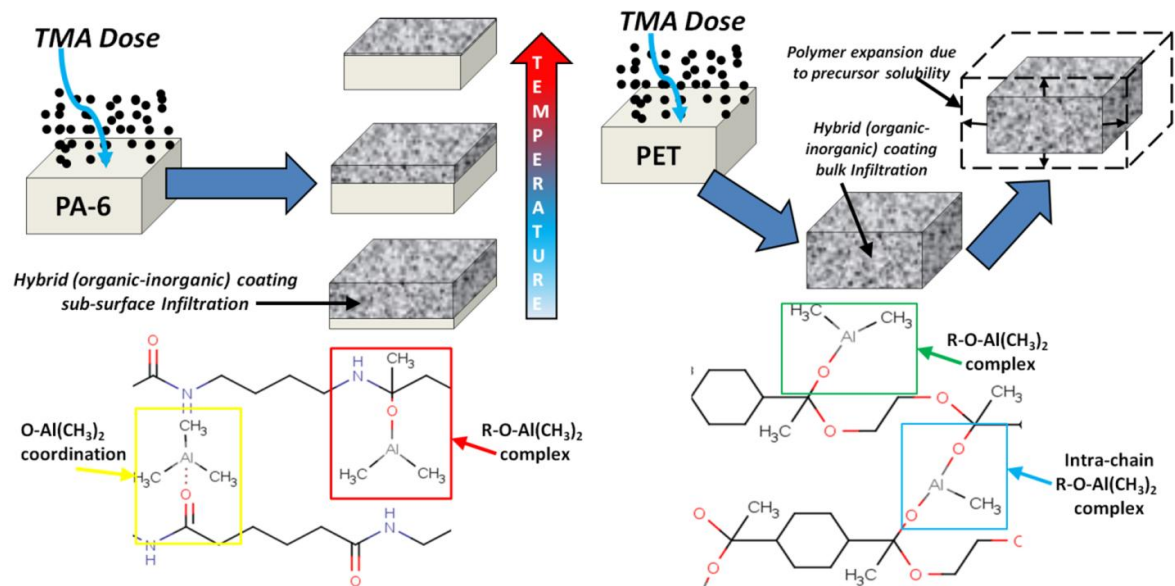


Figure 3.9 Schematic diagram describing the sub-surface nucleation behavior of TMA in PA-6 and PET based on observations from in-situ QCM analysis as shown in this. The Figures indicate possible reaction modes between TMA and functional groups along the backbone of PA-6 and PET polymer chains.

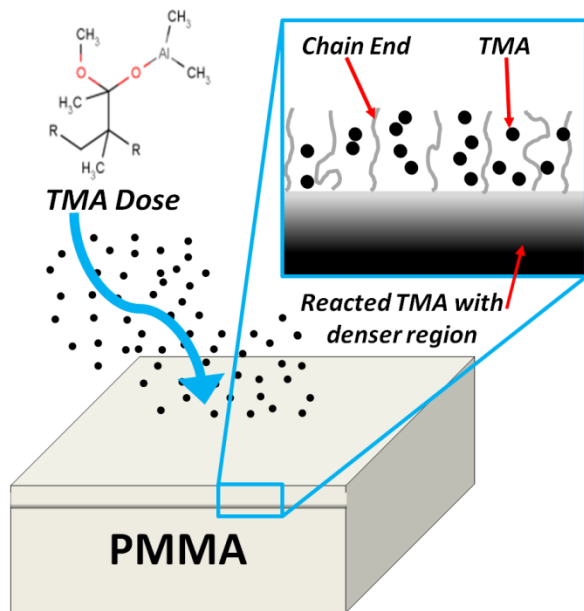


Figure 3.10. Schematic diagram representing the sub-surface infiltration of TMA in PMMA using observations from in-situ QCM analysis shown in Figures 5 and 6. The weak interaction between the interfaces of the gold plated quartz crystal and PMMA polymer film corresponds to a lower T_g at the free surface. This promotes the absorption of TMA into the sub-surface of the polymer where reactions take place with functional groups within denser regions of the polymer film.

Chapter 3 References:

1. Guo, R. H.; Jiang, S. X.; Yuen, C. W. M.; Ng, M. C. F.; Lan, J. W., Metallized textile design through electroless plating and tie-dyeing technique. *Journal of the Textile Institute* **2013**, 104, (10), 1049-1055.
2. Kwong, C. H.; Ng, S. P.; Kan, C. W.; Molina, R., Parametric Study of CF₄-plasma on the Hydrophobicity of Polyester Synthetic Leather. *Fibers and Polymers* **2013**, 14, (10), 1608-1613.
3. Wong, W. Y.; Lam, J. K. C.; Kan, C. W.; Postle, R., Influence of knitted fabric construction on the ultraviolet protection factor of greige and bleached cotton fabrics. *Textile Research Journal* **2013**, 83, (7), 683-699.
4. Bang, G.; Kim, S. W., Biodegradable poly(lactic acid)-based hybrid coating materials for food packaging films with gas barrier properties. *Journal of Industrial and Engineering Chemistry* **2012**, 18, (3), 1063-1068.
5. Jin, T.; Zhang, H., Biodegradable polylactic acid polymer with nisin for use in antimicrobial food packaging. *Journal of Food Science* **2008**, 73, (3), M127-M134.
6. Mangaraj, S.; Goswami, T. K.; Mahajan, P. V., Applications of Plastic Films for Modified Atmosphere Packaging of Fruits and Vegetables: A Review. *Food Engineering Reviews* **2009**, 1, (2), 133-158.
7. Mills, A.; Doyle, G.; Peiro, A. M.; Durrant, J., Demonstration of a novel, flexible, photocatalytic oxygen-scavenging polymer film. *Journal of Photochemistry and Photobiology a-Chemistry* **2006**, 177, (2-3), 328-331.
8. Siracusa, V.; Rocculi, P.; Romani, S.; Dalla Rosa, M., Biodegradable polymers for food packaging: a review. *Trends in Food Science & Technology* **2008**, 19, (12), 634-643.
9. Amin, M., Methods For Preparation of Nano-composites For Outdoor Insulation applications. *Reviews on Advanced Materials Science* **2013**, 34, (2), 173-184.
10. Zhi, C. Y.; Bando, Y.; Terao, T.; Tang, C. C.; Kuwahara, H.; Golberg, D., Towards Thermoconductive, Electrically Insulating Polymeric Composites with Boron Nitride Nanotubes as Fillers. *Advanced Functional Materials* **2009**, 19, (12), 1857-1862.
11. Boateng, J. S.; Matthews, K. H.; Stevens, H. N. E.; Eccleston, G. M., Wound healing dressings and drug delivery systems: A review. *Journal of Pharmaceutical Sciences* **2008**, 97, (8), 2892-2923.

12. Kokabi, M.; Sirousazar, M.; Hassan, Z. M., PVA-clay nanocomposite hydrogels for wound dressing. *European Polymer Journal* **2007**, 43, (3), 773-781.
13. Madsen, J.; Armes, S. P.; Bertal, K.; Lomas, H.; MacNeil, S.; Lewis, A. L., Biocompatible wound dressings based on chemically degradable triblock copolymer hydrogels. *Biomacromolecules* **2008**, 9, (8), 2265-2275.
14. Ong, S. Y.; Wu, J.; Moochhala, S. M.; Tan, M. H.; Lu, J., Development of a chitosan-based wound dressing with improved hemostatic and antimicrobial properties. *Biomaterials* **2008**, 29, (32), 4323-4332.
15. Feng, J. Y.; Zhang, J. C., Oil filtration performance of a hemp/cotton spunlaced nonwoven. *Textile Research Journal* **2013**, 83, (20), 2191-2203.
16. Ren, X.; Shon, H. K.; Jang, N.; Lee, Y. G.; Bae, M.; Lee, J.; Cho, K.; Kim, I. S., Novel membrane bioreactor (MBR) coupled with a nonwoven fabric filter for household wastewater treatment. *Water Research* **2010**, 44, (3), 751-760.
17. Payen, J.; Vroman, P.; Lewandowski, M.; Perwuelz, A.; Calle-Chazelet, S.; Thomas, D., Influence of fiber diameter, fiber combinations and solid volume fraction on air filtration properties in nonwovens. *Textile Research Journal* **2012**, 82, (19), 1948-1959.
18. Duran, K.; Bahtiyari, I.; Atav, R., Protective nonwoven technical textiles. *Tekstil Ve Konfeksiyon* **2007**, 17, (3), 174-177.
19. Chen, J. Y.; Tucker, P. A.; Cuculo, J. A., High-performance PET fibers via liquid isothermal bath high-speed spinning: Fiber properties and structure resulting from threadline modification and posttreatment. *Journal of Applied Polymer Science* **1997**, 66, (13), 2441-2455.
20. Alan E. Tonelli, M. S., *Polymers From the Inside Out: An Introduction to Macromolecules*. In Wiley: 2001.
21. Gawish, S. M.; El-Ola, S. M. A.; Ramadan, A. M.; Abou El-Kheir, A. A., Citric Acid Used as a Crosslinking Agent for the Grafting of Chitosan onto Woolen Fabric. *Journal of Applied Polymer Science* **2012**, 123, (6), 3345-3353.
22. Ibrahim, N. A.; El-Zairy, W. M.; El-Zairy, M. R.; Eid, B. M.; Ghazal, H. A., A smart approach for enhancing dyeing and functional finishing properties of cotton cellulose/polyamide-6 fabric blend. *Carbohydrate Polymers* **2011**, 83, (3), 1068-1074.
23. Klemencic, D.; Tomsic, B.; Kovac, F.; Simoncic, B., Antimicrobial cotton fibres prepared by in situ synthesis of AgCl into a silica matrix. *Cellulose* **2012**, 19, (5), 1715-1729.

24. Ojstrsek, A.; Kleinschek, K. S.; Fakin, D., Characterization of nano-sized TiO₂ suspensions for functional modification of polyester fabric. *Surface & Coatings Technology* **2013**, 226, 68-74.
25. Sherrill, J.; Michielsen, S.; Stojiljkovic, I., Grafting of light-activated antimicrobial materials to nylon films. *Journal of Polymer Science Part a-Polymer Chemistry* **2003**, 41, (1), 41-47.
26. Noeske, M.; Degenhardt, J.; Strudthoff, S.; Lommatzsch, U., Plasma jet treatment of five polymers at atmospheric pressure: surface modifications and the relevance for adhesion. *International Journal of Adhesion and Adhesives* **2004**, 24, (2), 171-177.
27. Liu, L.; Pan, S. Q., Preparation and Properties of SWNTs/PU Conductive Nonwovens with High SWNTs Loadings. *Integrated Ferroelectrics* **2012**, 136, 118-126.
28. Kalanyan, B.; Oldham, C. J.; Sweet, W. J.; Parsons, G. N., Highly Conductive and Flexible Nylon-6 Nonwoven Fiber Mats Formed using Tungsten Atomic Layer Deposition. *Acs Applied Materials & Interfaces* **2013**, 5, (11), 5253-5259.
29. Mao, Q. H.; Fell, C. J.; Scully, A. D., Self-assembled nano-phase particles for enhanced oxygen barrier coatings on polymeric materials. *Progress in Organic Coatings* **2013**, 76, (1), 51-59.
30. Malato, S.; Fernandez-Ibanez, P.; Maldonado, M. I.; Blanco, J.; Gernjak, W., Decontamination and disinfection of water by solar photocatalysis: Recent overview and trends. *Catalysis Today* **2009**, 147, (1), 1-59.
31. Jena, K. K.; Rout, T. K.; Narayan, R.; Raju, K., Novel organic-inorganic hybrid coatings prepared by the sol-gel process: corrosion and mechanical properties. *Polymer International* **2012**, 61, (7), 1101-1106.
32. Xu, Y. X.; Wen, Y. Q.; Wu, Y. N.; Lin, C. X.; Li, G. T., Hybrid nanofibrous mats with remarkable solvent and temperature resistance produced by electrospinning technique. *Materials Letters* **2012**, 78, 139-142.
33. Alongi, J.; Malucelli, G., State of the art and perspectives on sol-gel derived hybrid architectures for flame retardancy of textiles. *Journal of Materials Chemistry* **2012**, 22, (41), 21805-21809.
34. Mahltig, B.; Haufe, H.; Bottcher, H., Functionalisation of textiles by inorganic sol-gel coatings. *Journal of Materials Chemistry* **2005**, 15, (41), 4385-4398.

35. Pandey, S.; Mishra, S. B., Sol-gel derived organic-inorganic hybrid materials: synthesis, characterizations and applications. *Journal of Sol-Gel Science and Technology* **2011**, 59, (1), 73-94.
36. Schottner, G., Hybrid sol-gel-derived polymers: Applications of multifunctional materials. *Chemistry of Materials* **2001**, 13, (10), 3422-3435.
37. Lee, S. M.; Pippel, E.; Knez, M., Metal Infiltration into Biomaterials by ALD and CVD: A Comparative Study. *Chemphyschem* **2011**, 12, (4), 791-798.
38. Leskela, M.; Ritala, M., Atomic layer deposition (ALD): from precursors to thin film structures. *Thin Solid Films* **2002**, 409, (1), 138-146.
39. Parsons, G. N.; George, S. M.; Knez, M., Progress and future directions for atomic layer deposition and ALD-based chemistry. *Mrs Bulletin* **2011**, 36, (11), 865-871.
40. Spagnola, J. C.; Gong, B.; Arvidson, S. A.; Jur, J. S.; Khan, S. A.; Parsons, G. N., Surface and sub-surface reactions during low temperature aluminium oxide atomic layer deposition on fiber-forming polymers. *Journal of Materials Chemistry* **2010**, 20, (20), 4213-4222.
41. Halbur, J. C.; Padbury, R. P.; Jur, J. S., Induced wetting of polytetrafluoroethylene by atomic layer deposition for application of aqueous-based nanoparticle inks. *Materials Letters* **2013**, 101, 25-28.
42. Jur, J. S.; Sweet, W. J.; Oldham, C. J.; Parsons, G. N., Atomic Layer Deposition of Conductive Coatings on Cotton, Paper, and Synthetic Fibers: Conductivity Analysis and Functional Chemical Sensing Using "All-Fiber" Capacitors. *Advanced Functional Materials* **2011**, 21, (11), 1993-2002.
43. Jur, J. S.; Spagnola, J. C.; Lee, K.; Gong, B.; Peng, Q.; Parsons, G. N., Temperature-Dependent Subsurface Growth during Atomic Layer Deposition on Polypropylene and Cellulose Fibers. *Langmuir* **2010**, 26, (11), 8239-8244.
44. Wilson, C. A.; Grubbs, R. K.; George, S. M., Nucleation and growth during Al₂O₃ atomic layer deposition on polymers. *Chemistry of Materials* **2005**, 17, (23), 5625-5634.
45. Gong, B.; Peng, Q.; Jur, J. S.; Devine, C. K.; Lee, K.; Parsons, G. N., Sequential Vapor Infiltration of Metal Oxides into Sacrificial Polyester Fibers: Shape Replication and Controlled Porosity of Microporous/Mesoporous Oxide Monoliths. *Chemistry of Materials* **2011**, 23, (15), 3476-3485.

46. Gong, B.; Parsons, G. N., Quantitative in situ infrared analysis of reactions between trimethylaluminum and polymers during Al₂O₃ atomic layer deposition. *Journal of Materials Chemistry* **2012**, 22, (31), 15672-15682.
47. Brandrup, J.; Immergut, E. H.; Grulke, E. A.; Abe, A.; Bloch, D. R., Handbook of Polymers. In John Wiley & Sons: 2005.
48. Elam, J. W.; Groner, M. D.; George, S. M., Viscous flow reactor with quartz crystal microbalance for thin film growth by atomic layer deposition. *Review of Scientific Instruments* **2002**, 73, (8), 2981-2987.
49. Rocklein, M. N.; George, S. M., Temperature-induced apparent mass changes observed during quartz crystal microbalance measurements of atomic layer deposition. *Analytical Chemistry* **2003**, 75, (19), 4975-4982.
50. P. Neogi, *Diffusion in Polymers*. In New York : Marcel Dekker: 1996.
51. Cohen, M. H.; Turnbull, D., Molecular Transport In Liquids and Glasses. *Journal of Chemical Physics* **1959**, 31, (5), 1164-1169.
52. Sun, Y. J.; Padbury, R. P.; Akyildiz, H. I.; Goertz, M. P.; Palmer, J. A.; Jur, J. S., Influence of Subsurface Hybrid Material Growth on the Mechanical Properties of Atomic Layer Deposited Thin Films on Polymers. *Chemical Vapor Deposition* **2013**, 19, (4-6), 134-141.
53. Vasanthan, N.; Kotek, R.; Jung, D. W.; Salem, D.; Tonelli, A.; Shin, I. D., Lewis acid-base complexation of polyamide 66 as a means to control hydrogen bonding to form high strength fibers and films. *Abstracts of Papers of the American Chemical Society* **2004**, 227, U462-U462.
54. Vasanthan, N.; Kotek, R.; Jung, D. W.; Shin, D.; Tonelli, A. E.; Salem, D. R., Lewis acid-base complexation of polyamide 66 to control hydrogen bonding, extensibility and crystallinity. *Polymer* **2004**, 45, (12), 4077-4085.
55. Francis A. Carey, R. J. S., *Advanced Organic Chemistry: Part A: Structure and Mechanisms*. 4th ed.; Springer: 2007.
56. Johnson, A., The theory of coloration of textiles. In Second ed.; The Society of Dyers and Colorists: 1989.
57. Keddie, J. L.; Jones, R. A. L.; Cory, R. A., Interface and Surface Effects on the Glass-Transition Temperature in Thin Polymer-Films. *Faraday Discussions* **1994**, 98, 219-230.

58. Xia, W. J.; Mishra, S.; Keten, S., Substrate vs. free surface: Competing effects on the glass transition of polymer thin films. *Polymer* **2013**, 54, (21), 5942-5951.
59. Akyildiz, H. I.; Padbury, R. P.; Parsons, G. N.; Jur, J. S., Temperature and Exposure Dependence of Hybrid Organic-Inorganic Layer Formation by Sequential Vapor Infiltration into Polymer Fibers. *Langmuir* **2012**, 28, (44), 15697-15704.
60. Gong, B.; Spagnola, J. C.; Parsons, G. N., Hydrophilic mechanical buffer layers and stable hydrophilic finishes on polydimethylsiloxane using combined sequential vapor infiltration and atomic/molecular layer deposition. *Journal of Vacuum Science & Technology A* **2012**, 30, (1).

CHAPTER 4

AN *IN-SITU* COMPARISON OF PRECURSOR INFILTRATION INTO POLYMER THIN FILMS VIA ATOMIC LAYER DEPOSITION AND SEQUENTIAL VAPOR INFILTRATION

4.1. Introduction:

Atomic Layer deposition (ALD) is an effective technique of forming nanoscale inorganic coatings on a surface by sequential exposures of an organometallic precursor and a co-reacting vapor species such as water.¹ The saturation and self-limiting behavior of the chemical reactions on the surface of a substrate afford the opportunity to deposit inorganic coatings on a broad range of surfaces.²⁻⁸ Various ALD chemistries, such as trimethylaluminum (TMA) and water to form aluminum oxide, can take place at relatively low temperatures. Subsequently, ALD has been explored on polymer substrates such as thin films and fibers.⁹⁻¹⁵ While multiple ALD cycles can produce nanoscale inorganic coatings on a broad range of polymers, the coating morphology depends strongly on the chemistry of the polymer repeat unit and the reaction mechanism between the polymer and ALD precursors.^{12,15,16} In a broad sense, two types of nanoscale inorganic coating morphology that can be formed on polymers are uniform, conformal coatings with an abrupt interface between the inorganic and polymer surface, and hybrid organic-inorganic coatings. The latter has been predominantly observed in polymers such as polyamides and polyesters that contain carbonyl functional groups.^{16,17}

During an ALD process, previous research has shown that hybrid organic-inorganic coatings are dependent on the diffusion of precursors into the polymer sub-surface and the subsequent chemical reactions with the functional groups of the polymer.^{15,16,17} This has inspired the investigation of various adaptations to the ALD process for example, sequential vapor infiltration (SVI)^{18,19,20}, sequential infiltration synthesis (SIS)²¹ and multiple pulse infiltration (MPI)^{22,23,24}, which promote the hybrid material formation reaction with the polymer. While there are subtle differences between each technique, the general objective is extending the precursor exposure to promote the diffusion of organometallic precursors into the polymer sub-surface. Both ALD and infiltration processes have demonstrated the ability to introduce highly desirable properties to various polymer substrates. For example, controlled wetting transitions on polypropylene and cotton²⁵, enhanced mechanical strength of natural fibers²² and conductive coatings on inherently insulating polymers.¹⁴

During an SVI process, the increased precursor exposure is introduced by a ‘hold’ step after each precursor dose which immerses the polymer substrate for an extended period of time.^{18,19} A major difference between ALD and SVI is that successive cycling of the precursor and reactant is not employed in SVI. That is, the organometallic precursor exposure can be repeated multiple times to vary the extent of reaction. In reality, the SVI process allows for growth of the hybrid coating within the polymer sub-surface in a single exposure cycle.¹⁸ This provides an exciting opportunity to decrease the processing time necessary to achieve a given modification under “ALD-like” processing that takes advantage of the reactivity of the precursor and organic species on a polymer surface to form the hybrid modification.

For the first-time, we describe an SVI process using *in-situ* techniques to highlight the characteristic infiltration behavior and subsequent mass uptake of organometallic precursor and its co-reactant. Specifically, the infiltration and mass uptake of TMA into polyamide-6 (PA6) and polybutylene terephthalate (PBT) thin films are analyzed by *in-situ* quartz crystal microgravimetry (QCM). The key mechanisms of the SVI process are emphasized and studied in more detail by comparing the mass uptake behavior of TMA multidoses with and without a precursor hold step. The TMA multidosing scheme is achieved by using a typical ALD cycle sequence with an eliminated water dose. The hold step is introduced to the sequence by programming the reactor to shut off the vacuum pump for a certain period of time after the precursor dose which is followed by a standard N₂ purge.

4.2. Materials and Methods:

Preparation of polymer solutions. To compare the infiltration behavior and diffusion of organometallic precursors into polymers via SVI and ALD, *in-situ* QCM is utilized by spin casting polymer thin films of nanoscale thickness on to quartz crystals and exposing them to TMA and water half exposure cycles. Initially, PA-6 and PBT polymer solutions were prepared by dissolving 3 wt. % PA-6 pellets (Ultramid®) and PBT pellets (BASF®) in 95 % purity Formic Acid (reagent grade, Sigma Aldrich Inc.) and 99% purity trifluoroacetic acid (reagent grade, Sigma Aldrich Inc.), respectively. The polymer solutions were allowed to mix via magnetic stirring for approximately 12 hours at room temperature prior to spincoating.

Spin coating procedure and QCM assembly. Polymer thin films of PA-6, PBT, and PET were formed by spin coating (Laurell Technologies) a sufficient quantity of each polymer

solution at 3000 rpm for 1 minute onto unpolished, gold plated quartz crystals (resonant frequency 6 MHz) obtained from Inficon and used as received. After spin coating, the polymer coated crystals were baked at 90 °C for 1 minute to ensure all of the residual solvent was removed from the polymer films. Ellipsometry measurements of PA-6 and PBT films spun on to silicon wafers confirmed film thicknesses of 340 nm and 834 nm, respectively. A polymer coated quartz crystal was placed inside a crystal drawer (Inficon) and secured with conductive silver epoxy which was cured at room temperature for 24 hours. The crystal drawer was mounted to a sensor head that was vacuum sealed inside the main chamber of the viscous flow reactor. The change in frequency of the quartz crystal before, during and after the precursor doses was monitored at a rate of 4 Hz. the QCM was allowed to stabilize for several hours to the designated reaction chamber temperature. The temperature stabilization is important for reducing the magnitude of temperature induced mass transients in the mass uptake data. The experiments were not conducted until the change in frequency of the quartz crystal was $\leq \pm 0.2$ Hz/min. After stabilization, the Z-factor of the QCM was calculated to check that the change in frequency caused by the polymer thin film was within 2% of the uncoated quartz crystal frequency. Under this condition the Sauerbrey relationship is used to convert the change in frequency to a change in mass.

QCM analysis of TMA multidoses with & without a hold step. The infiltration of TMA into the sub surface of PA-6, and PBT polymer films via TMA multidoses with and without a hold step was performed at a fixed temperature of 60°C. A fresh coated quartz crystal was used for each experiment. The pressure of the viscous flow reactor was kept constant at 1 Torr with a nitrogen gas flow rate of ~300 sccm. To investigate the infiltration of TMA into

the polymer thin films with a hold step, a half exposure cycle sequence of TMA Dose/Hold/Purge = 0.2/30/90 sec was repeated for 10 cycles followed by a water half exposure cycle sequence of H₂O Dose/Hold/Purge = 0.2/30/90 for 5 cycles. A purge time of 90 secs was chosen to remove unreacted TMA from the reaction chamber. The infiltration of TMA into the polymer thin films via TMA multidoses without a hold step was investigated using a cycle sequence of TMA/Purge/H₂O/Purge = 0.2/60/0/60 sec. The above sequence was repeated for 10 cycles which corresponded to 10 consecutive exposure cycles (i.e. multidoses) of TMA with an eliminated water dose. A total purge time of 120 secs was selected to allow easy comparison with the QCM data obtained from the SVI process.

ToF-SIMS analysis of PBT and PA-6 polymer films. Depth profiles of TMA exposed to PBT and PA-6 polymer films were obtained via ToF-SIMS (ION TOF TOF-SIMS 5) using a Cs⁺ ion source. The depth profiles were obtained from PBT and PA6 films with thicknesses ~270nm and 834nm produced by spin coating 3 wt. % polymer solutions onto Si wafers at 3000 rpm. The PBT and PA-6 polymer films were exposed to a half exposure cycle sequence of TMA Dose/Hold/Purge = 0.2/30/90 sec repeated for 10 cycles followed by a water half exposure cycle sequence of H₂O Dose/Hold/Purge = 0.2/30/90 for 5 cycles. The TMA infiltrated films required no surface treatments prior to ToF-SIMS analysis.

4.3. Results and Discussion

In-situ analysis of SVI processing on PBT. An example of the *in-situ* QCM analysis of SVI processing on a PBT film at 60°C is provided in Figure 4.1. A temperature of 60°C was chosen to demonstrate the feasibility of the SVI mechanism at low reactor temperatures.²⁶ Prior to the half exposure cycle of TMA; the reaction chamber was purged for approximately

300 seconds with nitrogen gas which produces an inert atmosphere within the reaction chamber. After an initial purge (120 seconds), the PBT film was introduced to the first TMA dose at $t = 120$ seconds. During the SVI process TMA was held inside the reaction chamber for a hold period of 30 seconds after each successive dose. The mass uptake of TMA after the first dose and hold step is approximately 9800 ng/cm^2 as shown in Figure 4.1. Following the hold step, a 90 second purge was employed to remove any unreacted TMA in the chamber, including that in polymer. As demonstrated in Figure 4.1, there is significant desorption of TMA from the polymer during the first purge step (~as 7000 ng/cm^2). The SVI process described above is repeated a total of 10 times from $t = 120$ to $t = 1200$ seconds. The absorption of TMA per dose decreases with each successive TMA dose and hold step as the sub-surface of the PBT film becomes saturated with TMA and the number of accessible reactive sites decreases. At $t = 1200$ seconds, the reaction chamber is purged with N_2 gas at 1 Torr for 300 seconds prior to a exposure cycles of water. The length of the final purge before the water exposure cycle is strategically lengthened to reduce potential reaction with unreacted TMA that might still be diffusing out of polymer, which would result in preferential CVD growth of aluminium oxide. After the 300 sec purge, a set of 5 dose and hold steps of H_2O is introduced to the PBT film from $t = 1500$ to $t = 2160$ seconds. *In-situ* FT-IR analysis of PBT polymer films has previously indicated the removal of C=O and C-O-C units of the polymer backbone and an increase in Al-CH₃ stretching modes after TMA exposure. As such, TMA molecules react with nucleophilic carbonyl or ether groups of the PBT backbone forming C-O-Al(CH₃)₂ units.¹⁷ During the half exposure cycle of water, the chemical reaction proceeds through a ligand exchange mechanism between the CH₃ groups

of TMA covalently bonded to the backbone of the PBT polymer chain and the hydroxyl group of the water molecules forming C-O-Al-O units.¹⁷ The overall mass gain of alumina in the PBT specimen after the half exposure cycle of water is $\sim 10000 \text{ ng/cm}^2$. From the absorption and desorption of TMA during the first half exposure cycle, it is clear that overwhelming majority of the reaction occurs in this stage.

For comparison, Figure 4.1 also shows the mass uptake behaviour of alumina ALD on a PBT polymer film using an ALD cycle sequence of TMA/N₂/H₂O/N₂ = 0.2/30/0.2/45 seconds. Between $t = 120$ seconds and $t = 480$ seconds a nucleation period is observed in which TMA infiltrates the sub-surface of the polymer film. This is indicated by the large initial absorption and desorption of TMA during the first 4 cycles between $t = 120$ seconds and $t = 480$ seconds. After the 4th ALD cycle, the absorption of TMA reduces as the sub-surface alumina coating progresses towards the near surface of the polymer film. This is followed by typical ALD growth as indicated by the constant mass uptake between $t = 480$ seconds and $t = 2400$ seconds. In comparison to the alumina SVI process, the initial absorption and reaction of TMA at $t = 120$ seconds and the final mass uptake of alumina at $t = 2400$ seconds during the ALD process are significantly less (2660 ng/cm^2 and 4000 ng/cm^2 respectively).

At this point, it is important to quantify the total exposure, defined as the amount of precursor delivered to a growth surface during the dose time, i.e. the precursor vapour pressure vs. time.^{18 27} The unit of exposure is the Langmuir (L) which is expressed as $10^6 \text{ Torr}\cdot\text{sec}$. In an ALD processing sequence, the exposure is quantified by the dose time and

vacuum pump throughput. In the apparatus used for these experiments, and assuming a TMA partial pressure of 0.3 Torr, a 0.2 sec dose corresponds to an exposure of $\sim 6 \times 10^5$ L, which is much greater than the exposure required to saturate growth on a planar hydroxide-terminated surface with TMA exposure. For growth on polymers, one needs to consider the added consequence of diffusion and the nucleation period of the subsurface reaction which adds an additional processing variable. As shown in Figure 4.1, ALD processing on polymers show a nucleation period prior to surface saturation.

Of interest is the consideration of the gas flow characteristics of TMA through the reaction chamber and the effect that this has on the mass uptake of precursor within the polymer film. With a reaction chamber diameter of 20 cm and a length of 90 cm, the subsequent gas residence time for the 0.2 second TMA dose at 1 Torr (~ 300 sccm) is 0.04 sec. As the 0.2 second dose of precursor travels through the reaction chamber parallel to the growth surface, only a fraction of the reactant exposure diffuses into the polymer subsurface. Furthermore, if a typical sample size is 1x1 cm, the 0.2 second dose of precursor is in contact with the sample surface for approx 0.4 millisecond. In contrast, the hold step of the SVI process suspends the influence of diffusive and convective flow by holding the precursor within the reaction chamber for an extended period of time. This provides more time to build-up the concentration of precursor at the polymer surface and promotes the diffusion of precursor into the sub surface of the polymer.

It is clear from the prior analysis that the extent of the subsurface growth can be manipulated based on the processing parameters such as dose and the hold time. To explore

the processing scheme in more detail, the following section explores the exposure extremes of TMA in two polymers, PA6 and PBT.

Effect of Hold Time and Dose. Figure 4.2 Panel (a) and (b) compare half exposure cycles of TMA in PBT and PA6 polymer films respectively for two sequences: the first following that of the SVI process in which a hold time is employed, and second for a pulse of TMA followed immediately by an inert purge (i.e. an ALD sequence with no H₂O half cycle, herein referred to as ‘multidosing’). First, it is important to note the comparisons of the SVI process between PBT and PA6. In comparison to PBT, the first dose and hold step of TMA in PA-6 achieves an absorbed mass gain of 2550 ng/cm². As such, the PA6 polymer film saturates after the first TMA dose and hold step as indicated by the zero net increase in mass uptake with successive dose and hold steps. This results in a final mass uptake of TMA in PA-6 of approximately 2400 ng/cm². Consequently, PA6 achieves a lower final mass uptake of TMA compared with PBT (13000 ng/cm²).

We next compare the mass uptake behavior of dose and hold steps in PBT and PA-6 with TMA multidosing. As demonstrated in Figure 4.2 Panel (a), PA-6 possesses a high initial absorption of TMA (approx. 2625 ng/cm²). However, desorption of TMA occurs from approximately $t = 0$ to $t = 600$ seconds between the 1st and 6th TMA dose which is preceded by a zero net mass gain of TMA. The initial absorption of TMA in PBT via the multidosing scheme is approximately 2660 ng/cm² and the final mass uptake of TMA after 10 multidoses is approximately 1900 ng/cm², much lower than the absorbed mass uptake

observed in the SVI hold step sequence. No evidence in saturation in the 10 multidoses is observed.

The comparison of these results presents a number of interesting observations that provides insight into the infiltration behavior. Perhaps the most obvious observation is that in both the SVI and multidose sequence, the extent of reaction in PA6 saturates in an overall less total exposure as compared to the PBT. We propose that the extent of reaction between TMA and PA-6 creates a dense sub-surface precursor layer as reaction sites are consumed throughout the diffusion length of TMA in PA-6. This shields available reaction sites within the bulk of the polymer film and prevents the absorption of successive precursor doses resulting in a lower mass uptake of TMA. In addition, presence of the hold step during the TMA exposure to PA6 provides extra time for the initial reaction to occur, albeit a slight increase in comparison to the same sequence alteration for PBT. As such, although the reaction between TMA and PA6 appears to be more favorable, PBT achieves a greater mass gain of TMA after multiple dose and hold steps. We expect that this is attributed to a lower extent of reaction that maintains access to reactive sites and promotes the diffusion of successive precursor exposures. Due to this lower affinity for reaction, materials such as PBT possess the potential to form a more complete hybrid organic-inorganic interface within the bulk of the polymer film.¹⁹

To demonstrate the bulk infiltration behavior of TMA into PBT, the polymer film was exposed to 10 TMA half exposure cycles of the SVI process and analyzed by ToF-SIMS. For comparison PA-6 was also analyzed using the same SVI parameters. Figure 4.3 shows ToF-

SIMS depth profiles of PA-6 and PBT indicating C^+ , $CsAl^+$ and Si^+ markers attributed to the polymer films, alumina and Si substrate, respectively. The data in Figure 4.3 shows the natural logarithm of the ion intensity from each marker corresponding to the ion yield during the Cs sputtering process. The gradual increase in intensity of the Si^+ marker between at 560nm for PA-6 PBT as shown in Figure 4.3 (a) is due to the uneven surface of the polymer film causing parts of the film to sputter at different rates. The ion intensities of the C^+ , $CsAl^+$ and Si^+ markers intersect at a depth of ~ 820 nm indicating that TMA has infiltrated the entire thickness of the polymer film. In comparison, the ion intensity of the $CsAl^+$ marker in PA-6 drops off at a depth of ~ 110 nm and intersects the C^+ marker intensity indicating the PA-6/Alumina interface. The C^+ intensity continues until it intersects the Si^+ marker at a depth of ~ 250 nm indicating the presence of the PA-6/Si interface.

It is evident that the introduction of the hold step to PBT allows a long diffusion time for the TMA to infiltrate into the polymer, resulting in the higher mass gain after the 10 cycles. To demonstrate the influence of the hold step more clearly, Figure 4.4 overlays the mass uptake of TMA attributed to one dose and hold step of the SVI half exposure cycle. As the mass uptake is followed, the hold step allows for the continuation of diffusion and reaction into the bulk of the PBT, driven by the concentration gradient of TMA outside and inside the polymer. The concentration gradient is reversed with the initiation of the inert purge. In comparison, the higher extent of reaction in PA-6 forms a thinner hybrid organic-inorganic coating within the subsurface of the polymer film in comparison to the bulk infiltration of TMA in PBT. This has been shown in other studies via cross section TEM

analysis and explains the low mass uptake of TMA from the QCM analysis utilized in this work.^{10 16}

In Figure 4.5, the hold time and the dose time are evaluated to explore the ability to control the overall hybrid material formation. Panel (a) shows time segments from one dose and hold step of TMA in PBT as the hold time increases from 0 to 60 sec. Within this range, the absorption of TMA within the polymer film increases from 2660 ng/cm² at 0 sec, to 12000 ng/cm² at 60 sec, a 450% increase. Within that time frame, the saturation is nearly completed within the 30 sec hold as a 375% increase is observed.

Figure 4.5 Panel (b) provides the effect of increasing dose time on the absorption of TMA into PBT in one SVI half exposure cycle in which the hold time remains constant at 60 seconds. The absorption of TMA increases from 12000 ng/cm² with a 0.2 seconds dose to approximately 14200 ng/cm² and 15500 ng/cm² with 1 second and 2 second doses, respectively. Despite a 5 fold increase in dose time from 0.2 seconds to 1 second and a 10 fold increase in dose time from 0.2 sec to 2 sec, the corresponding increase in absorption is only 18% and 29%, respectively. The increase in absorption of TMA from a 1 sec dose to a 2 second dose is only 9% (approx. 1300 ng/cm²). As would be expected, the dose time is less significant on the amount of TMA absorption as compared to the hold time. However, the dose time can influence the required hold time needed to obtain a given absorption. To exemplify this behavior, Figure 4.6 shows the absorption of TMA as both the dose and hold times of TMA in PBT are varied. As dose time increases from 0.2 sec to 1 sec with a 30 second hold, there is not a significant increase in absorbed TMA. When the hold time

increases from 30 seconds to 60 seconds for a 1 sec dose, the absorption of TMA increases by ~30%. A similar mass gain relationship between the dose time and hold time exists as the dose and hold time are increased. As the dose of TMA into the PBT film is given time to diffuse into the polymer film via the hold step, the precursor molecules are also given time to react with carbonyl functional groups along the back-bone of the polymer.

We hypothesize that the reaction of TMA with the PBT polymer film using a TMA dose time of 0.2 seconds and a hold time of 30 seconds is already sufficient to cause significant saturation of the polymer film. We anticipate that this consumes reactive sites and causes structural changes within the polymer film such as density changes that restricts the diffusion and absorption of further TMA exposures. This accounts for the fact that as dose time increases, the absorption of more TMA is not observed unless there is a sufficient increase in the hold time. A longer hold time gives the TMA molecules more time to diffuse into the polymer film and react with any available reaction sites.

4.4. Conclusion:

For the first time we demonstrate the mass uptake behavior of the SVI process using in-situ QCM analysis. In addition, this work highlights the fundamental differences in mass uptake behavior between ALD and SVI processes. The QCM analysis of TMA SVI in PBT indicates that the hold step of the SVI process promotes the diffusion of TMA corresponding to a larger mass uptake of TMA compared with ALD. The absorption of TMA is followed by significant desorption indicating that the reaction kinetics between TMA and the carbonyl group of PBT are slow. In comparison, the rapid saturation of the PA-6 film sub-surface

indicates that there is a faster reaction between TMA and the carbonyl of the amine group creating a dense precursor layer that limits the diffusion of successive precursor. Therefore, it is clear that diffusion of TMA plays an important role in TMA mass uptake. Despite the slower reaction kinetics between TMA and the carbonyl group of PBT, the polymer film achieves a larger mass gain compared with PA6. This is due to the lower extent of reaction that maintains access to reactive sites and promoting diffusion of successive precursor exposures. In order to control the nucleation behavior of precursor exposure to polymers, this work demonstrates the importance of considering the infiltration of precursor and resultant chemical reaction on the formation of a hybrid interface. Finally, the reactor design and gas transport behavior inside the reactor are also critical for the delivery and hence, the exposure characteristics.

Chapter 4 Figures:

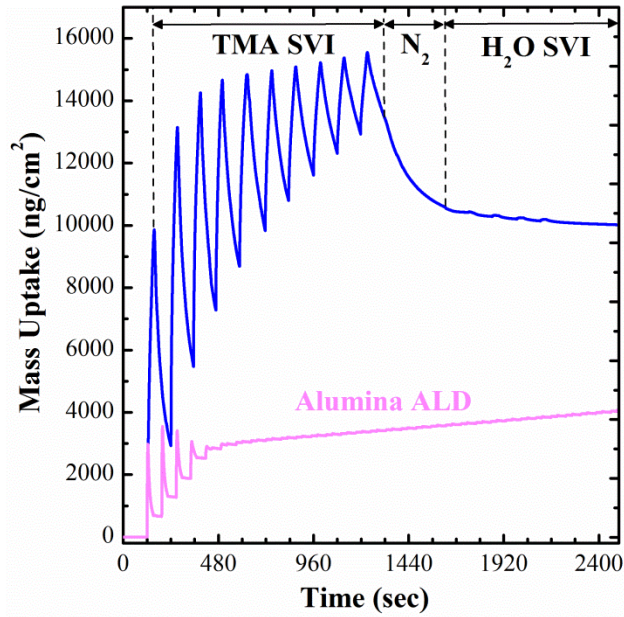


Figure 4.1 *In-Situ* QCM analysis of a complete SVI process in a PBT polymer thin film at 60°C. The figure indicates the mass gain associated with the TMA and water exposure cycles separated by an inert gas purge step. The mass uptake behavior of TMA in PBT via the SVI technique is compared to the mass uptake behavior of an alumina ALD process at 60°C.

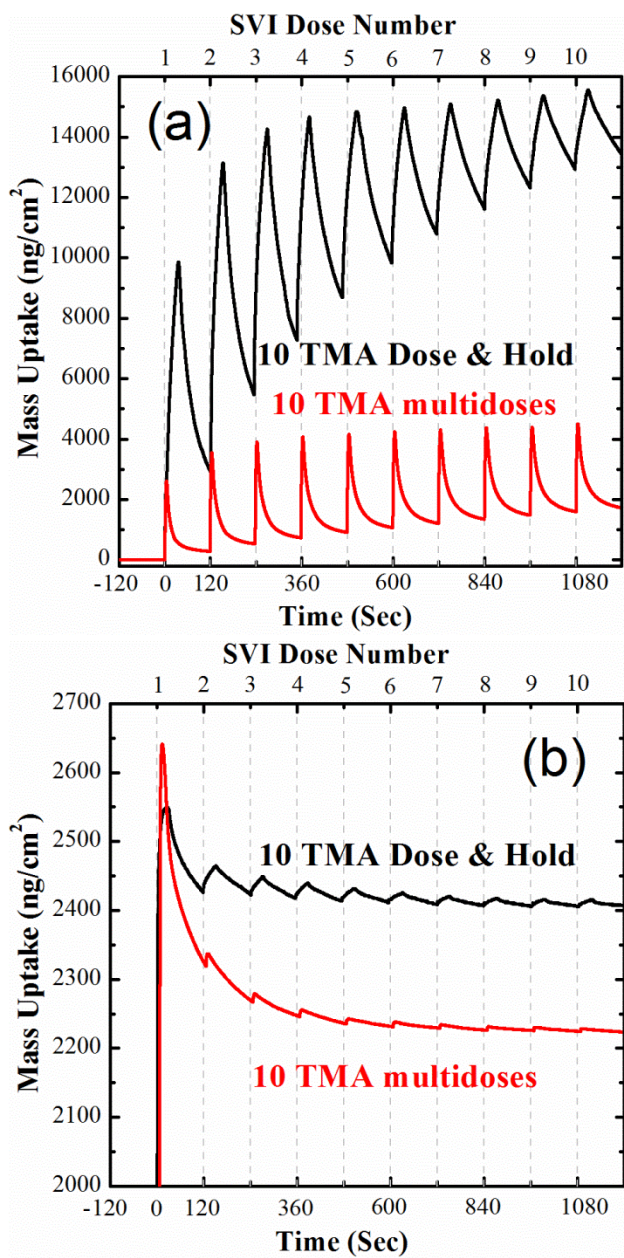


Figure 4.2. *In-situ* QCM analysis comparing the mass uptake of ten consecutive TMA exposure steps to PBT and PA6 films at 60°C. Panel (a) and Panel (b) compare the mass uptake of TMA dose and hold steps in PBT and PA-6, respectively using a half exposure cycle of TMA Dose/Hold/Purge = 0.2/30/90 seconds. The mass uptake behaviour of dose and hold steps in PBT and PA-6 are compared with TMA multidoses using an ALD cycle sequence of TMA/N₂/H₂O/N₂ = 0.2/60/0/60 second

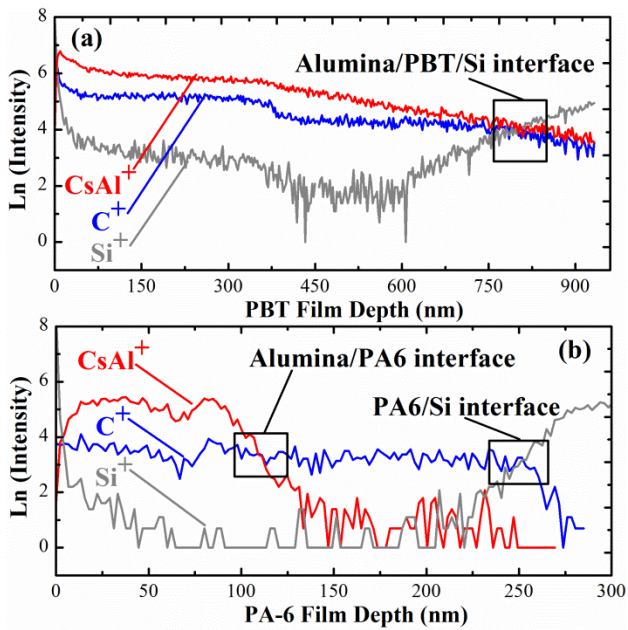


Figure 4.3. ToF-SIMS depth profiles are used to demonstrate the bulk infiltration of TMA in PBT and PA-6 at 60°C after exposure to 10 TMA half exposure cycles of the SVI process. The $CsAl^+$, Si^+ and C^+ markers represent alumina, Si wafer support and polymer films, respectively

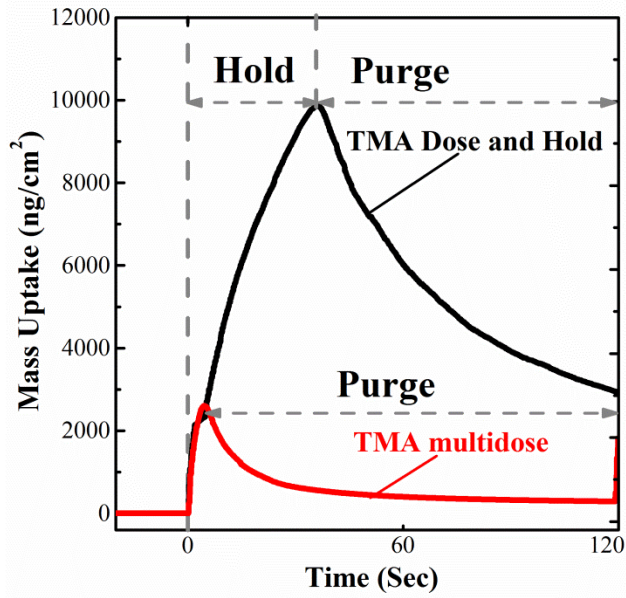


Figure 4.4. For clarification, the figure indicates the absorption of TMA within PBT attributed to the hold step of the SVI technique in comparison to the absorption of TMA via an ALD multidosing scheme.

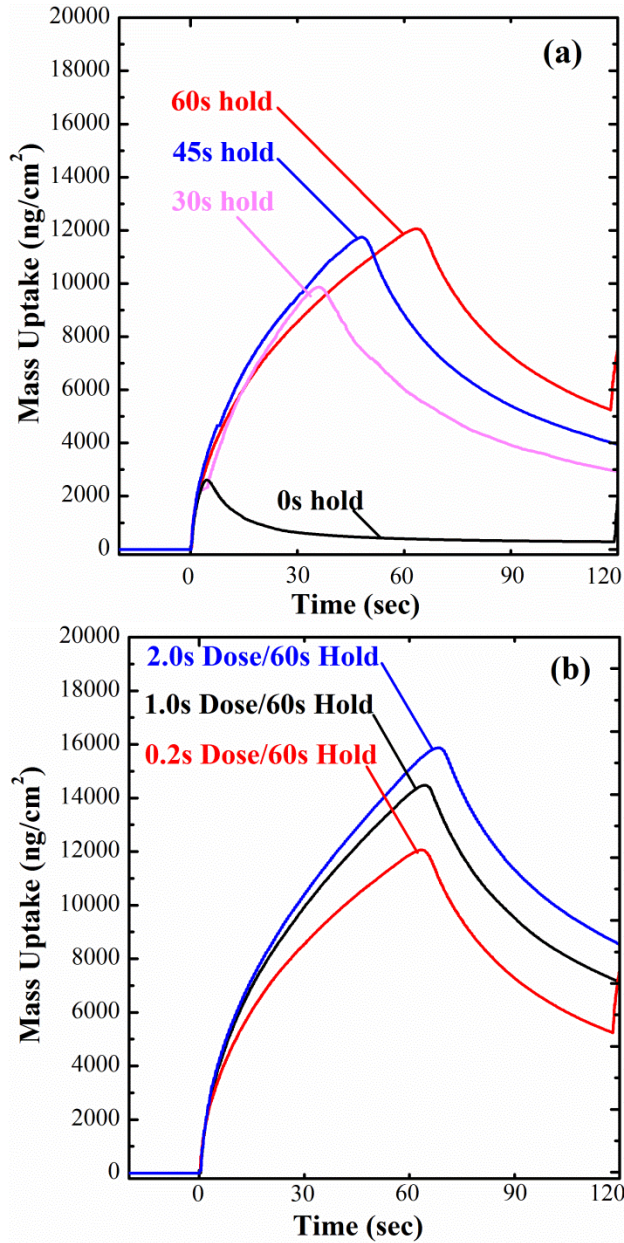


Figure 4.5 Panel (a). Time segment comparing the first dose and hold step of the SVI process highlighting the characteristic mass uptake behavior of TMA in PBT at 60°C with a cycle sequence of TMA Dose/Hold/Purge = 0.2/X/90 seconds, in which X = 0, 30, 45 and 60 second hold steps. **Panel (b).** Time segment comparing the effect of dose time on the characteristic mass uptake behavior of TMA in PBT at 60°C with a constant hold time of 60 sec.

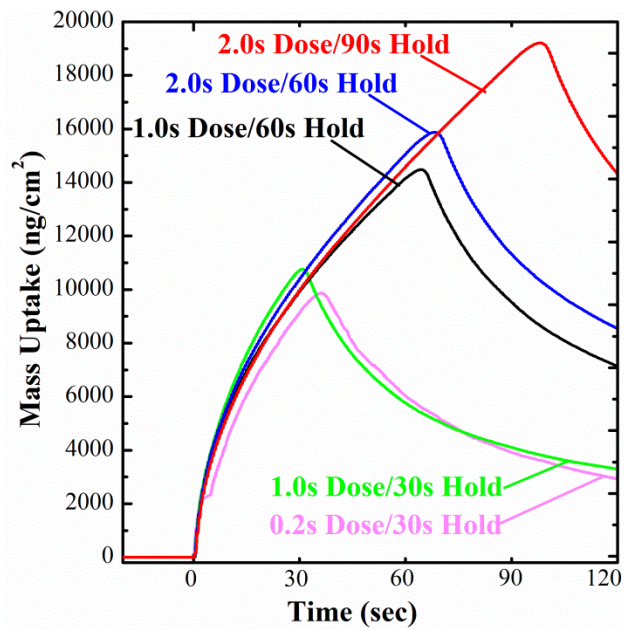


Figure 4.6. Time segment comparing variations in both dose time and hold tie of the SVI process highlighting the characteristic mass uptake behavior of TMA in PBT at 60°C.

Chapter 4 References:

1. Parsons, G. N.; George, S. M.; Knez, M., Progress and future directions for atomic layer deposition and ALD-based chemistry. *Mrs Bulletin* **2011**, *36* (11), 865-871.
2. Tai, K.; Hirano, T.; Yamaguchi, S.; Ando, T.; Hiyama, S.; Wang, J.; Nagahama, Y.; Kato, T.; Yamanaka, M.; Terauchi, S.; Kanda, S.; Yamamoto, R.; Tateshita, Y.; Tagawa, Y.; Iwamoto, H.; Saito, M.; Nagashima, N.; Kadomura, S., High performance pMOSFET with ALD-TiN/HfO₂ gate stack on (110) substrate by low temperature process. In *ESSDERC 2006: Proceedings of the 36th European Solid-State Device Research Conference*, Ionescu, A. M.; Declercq, M.; Leblebici, Y., Eds. 2006; pp 121-124.
3. Niinisto, L.; Paivasaari, J.; Niinisto, J.; Putkonen, M.; Nieminen, M., Advanced electronic and optoelectronic materials by Atomic Layer Deposition: An overview with special emphasis on recent progress in processing of high-k dielectrics and other oxide materials. *Physica Status Solidi a-Applied Research* **2004**, *201* (7), 1443-1452.
4. Hyde, G. K.; Park, K. J.; Stewart, S. M.; Hinstroza, J. P.; Parsons, G. N., Atomic layer deposition of Conformal inorganic nanoscale coatings on three-dimensional natural fiber systems: Effect of surface topology on film growth characteristics. *Langmuir* **2007**, *23* (19), 9844-9849.
5. Roth, K. M.; Roberts, K. G.; Hyde, G. K., Effect of Weave Geometry on Surface Energy Modification of Textile Materials via Atomic Layer Deposition. *Textile Research Journal* **2010**, *80* (18), 1970-1981.
6. Gluch, J.; Rossler, T.; Schmidt, D.; Menzel, S. B.; Albert, M.; Eckert, J., TEM characterization of ALD layers in deep trenches using a dedicated FIB lamellae preparation method. *Thin Solid Films* **2010**, *518* (16), 4553-4555.
7. Devine, C. K.; Oldham, C. J.; Jur, J. S.; Gong, B.; Parsons, G. N., Fiber Containment for Improved Laboratory Handling and Uniform Nanocoating of Milligram Quantities of Carbon Nanotubes by Atomic Layer Deposition. *Langmuir* **2011**, *27* (23), 14497-14507.
8. Kim, J. Y.; Ahn, J. H.; Kang, S. W.; Kim, J. H., Step coverage modeling of thin films in atomic layer deposition. *Journal of Applied Physics* **2007**, *101* (7).
9. Halbur, J. C.; Padbury, R. P.; Jur, J. S., Induced wetting of polytetrafluoroethylene by atomic layer deposition for application of aqueous-based nanoparticle inks. *Materials Letters* **2013**, *101*, 25-28.
10. Sun, Y. J.; Padbury, R. P.; Akyildiz, H. I.; Goertz, M. P.; Palmer, J. A.; Jur, J. S., Influence of Subsurface Hybrid Material Growth on the Mechanical Properties of Atomic

Layer Deposited Thin Films on Polymers. *Chemical Vapor Deposition* **2013**, *19* (4-6), 134-141.

11. Choi, D.-w.; Kim, S.-J.; Lee, J. H.; Chung, K.-B.; Park, J.-S., A study of thin film encapsulation on polymer substrate using low temperature hybrid ZnO/Al₂O₃ layers atomic layer deposition. *Current Applied Physics* **2012**, *12*, S19-S23.

12. Jur, J. S.; Spagnola, J. C.; Lee, K.; Gong, B.; Peng, Q.; Parsons, G. N., Temperature-Dependent Subsurface Growth during Atomic Layer Deposition on Polypropylene and Cellulose Fibers. *Langmuir* **2010**, *26* (11), 8239-8244.

13. Ferguson, J. D.; Weimer, A. W.; George, S. M., Atomic layer deposition of Al₂O₃ films on polyethylene particles. *Chemistry of Materials* **2004**, *16* (26), 5602-5609.

14. Jur, J. S.; Sweet, W. J.; Oldham, C. J.; Parsons, G. N., Atomic Layer Deposition of Conductive Coatings on Cotton, Paper, and Synthetic Fibers: Conductivity Analysis and Functional Chemical Sensing Using "All-Fiber" Capacitors. *Advanced Functional Materials* **2011**, *21* (11), 1993-2002.

15. Wilson, C. A.; Grubbs, R. K.; George, S. M., Nucleation and growth during Al₂O₃ atomic layer deposition on polymers. *Chemistry of Materials* **2005**, *17* (23), 5625-5634.

16. Spagnola, J. C.; Gong, B.; Arvidson, S. A.; Jur, J. S.; Khan, S. A.; Parsons, G. N., Surface and sub-surface reactions during low temperature aluminium oxide atomic layer deposition on fiber-forming polymers. *Journal of Materials Chemistry* **2010**, *20* (20), 4213-4222.

17. Gong, B.; Parsons, G. N., Quantitative in situ infrared analysis of reactions between trimethylaluminum and polymers during Al₂O₃ atomic layer deposition. *Journal of Materials Chemistry* **2012**, *22* (31), 15672-15682.

18. Akyildiz, H. I.; Padbury, R. P.; Parsons, G. N.; Jur, J. S., Temperature and Exposure Dependence of Hybrid Organic-Inorganic Layer Formation by Sequential Vapor Infiltration into Polymer Fibers. *Langmuir* **2012**, *28* (44), 15697-15704.

19. Gong, B.; Peng, Q.; Jur, J. S.; Devine, C. K.; Lee, K.; Parsons, G. N., Sequential Vapor Infiltration of Metal Oxides into Sacrificial Polyester Fibers: Shape Replication and Controlled Porosity of Microporous/Mesoporous Oxide Monoliths. *Chemistry of Materials* **2011**, *23* (15), 3476-3485.

20. Gong, B.; Spagnola, J. C.; Parsons, G. N., Hydrophilic mechanical buffer layers and stable hydrophilic finishes on polydimethylsiloxane using combined sequential vapor

infiltration and atomic/molecular layer deposition. *Journal of Vacuum Science & Technology A* **2012**, *30* (1).

21. Peng, Q.; Tseng, Y. C.; Darling, S. B.; Elam, J. W., A Route to Nanoscopic Materials via Sequential Infiltration Synthesis on Block Copolymer Templates. *Acs Nano* **2011**, *5* (6), 4600-4606.

22. Lee, S. M.; Pippel, E.; Gosele, U.; Dresbach, C.; Qin, Y.; Chandran, C. V.; Brauniger, T.; Hause, G.; Knez, M., Greatly Increased Toughness of Infiltrated Spider Silk. *Science* **2009**, *324* (5926), 488-492.

23. Lee, S. M.; Pippel, E.; Knez, M., Metal Infiltration into Biomaterials by ALD and CVD: A Comparative Study. *Chemphyschem* **2011**, *12* (4), 791-798.

24. Lee, S. M.; Ischenko, V.; Pippel, E.; Masic, A.; Moutanabbir, O.; Fratzl, P.; Knez, M., An Alternative Route Towards Metal-Polymer Hybrid Materials Prepared by Vapor-Phase Processing. *Advanced Functional Materials* **2011**, *21* (16), 3047-3055.

25. Hyde, G. K.; Scarel, G.; Spagnola, J. C.; Peng, Q.; Lee, K.; Gong, B.; Roberts, K. G.; Roth, K. M.; Hanson, C. A.; Devine, C. K.; Stewart, S. M.; Hojo, D.; Na, J. S.; Jur, J. S.; Parsons, G. N., Atomic Layer Deposition and Abrupt Wetting Transitions on Nonwoven Polypropylene and Woven Cotton Fabrics. *Langmuir* **2010**, *26* (4), 2550-2558.

26. Groner, M. D.; Fabreguette, F. H.; Elam, J. W.; George, S. M., Low-temperature Al₂O₃ atomic layer deposition. *Chemistry of Materials* **2004**, *16* (4), 639-645.

27. Jur, J. S.; Parsons, G. N., Atomic Layer Deposition of Al₂O₃ and ZnO at Atmospheric Pressure in a Flow Tube Reactor. *Acs Applied Materials & Interfaces* **2011**, *3* (2), 299-308.

CHAPTER 5

MECHANICAL MODIFICATION OF FIBER FORMING POLYMERS BY HYBRID ORGANIC-INORGANIC BUFFERS CREATED IN THE VAPOR PHASE

5.1. Introduction

Hybrid organic-inorganics are an exciting class of material that incorporates both organic and inorganic components mixed together at the molecular scale. Consequently, a unique feature is the formation of a material that is neither purely organic nor inorganic due to increased homogeneity between the mixed components.¹⁻³ Therefore, a key benefit of hybrid organic-inorganic materials is the development of multifunctional materials tailored for specific applications by unifying inorganic material properties such as: thermal stability, high dielectric constants, low permeability's, photocatalytic behavior and chemical resistance, without compromise to the attractive properties of organic materials such as flexibility and ease of form.⁴⁻⁸

Atomic Layer Deposition (ALD) has proven to be an effect technique of forming a hybrid organic-inorganic interface in the vapor phase by exposing polymeric substrates to sequential exposures of organometallic precursors and a suitable co-reactant.⁹⁻¹² The formation of a hybrid-organic inorganic coating is predominantly observed in polymers that contain functional C=O functionality, such as polyamides and polyesters.^{13,12} Research has shown that organometallic precursors penetrate the sub-surface of the polymer and react with functional groups along the backbone of the polymer producing coatings with a graded

finish.¹⁴ Further studies have revealed that under certain conditions, precursors can infiltrate the bulk of fiber forming polymers resulting in a hybrid modification that templates the porous internal structure of the polymer fiber.¹⁵ The infiltration of precursors into the sub-surface and bulk of polymers and the formation of a hybrid material has inspired adaptations to the ALD process by such as sequential vapor infiltration (SVI),^{15 16} sequential infiltration synthesis (SIS)¹⁷ and multiple pulse infiltration.^{18 19} The infiltration of precursors is promoted by increasing the exposure conditions using either hold steps or larger precursor doses.

This work explores the infiltration of trimethyl aluminum (TMA) into polyethylene Terephthalate (PET) films and fibers and reports on the process-structure-property relationships after modification using the SVI technique. To truly satisfy the requirement for multifunctional polymers without compromise to their intrinsic properties, the infiltration of organometallic precursors must either maintain or enhance the properties of the material. Therefore, this work explores the mechanical properties of meltspun PET fibers modified by sequential exposures of TMA using the SVI technique. The effect of polymer structure on the infiltration mechanism is explored and used to understand changes in mechanical properties of the fibers.

5.2. Materials and Methods

Spin coating procedure and polymer film preparation. Initially, a PET polymer solution was prepared by dissolving 3 wt. % PET pellets (Eastman) in 99% purity trifluoroacetic acid (reagent grade, Sigma Aldrich Inc.). The polymer solution was mixed via magnetic stirring

for approximately 12 hours at room temperature. Polymer thin films of PET were formed by spin coating (Laurell Technologies) a sufficient quantity of polymer solution at 3000 rpm for 1 minute onto unpolished, gold plated quartz crystals (Inficon, resonant frequency 6 MHz) and silicon (Si) wafers (1 inch x 1 inch). After spin coating, the polymer coated crystals and silicon wafers were baked at 100 °C for 1 minute to ensure all of the residual solvent was removed from the polymer films. Ellipsometry measurements of a PET film spun on to a silicon wafer confirmed the film thicknesses were approximately 500 nm.

The crystallinity of PET films on both quartz crystals and Si wafers was varied by annealing specimens to different temperatures above T_g (60°C – 80°C)²⁰ on a hot plate to promote the motion of polymer chain segments. The specimens were annealed at 150°C and 200°C for 30 minutes to give the PET polymer films time to come in thermal equilibrium with the hot plate and then slow quenched to room temperature to promote the growth of crystals within the polymer film. Annealed PET films on Si wafers and quartz crystals were used for XRD analysis and *in-situ* QCM analysis, respectively.

QCM assembly A polymer coated quartz crystal was placed inside a crystal drawer (Inficon) and secured with conductive silver epoxy which was cured at room temperature for 24 hours. The crystal drawer was mounted to a sensor head that was vacuum sealed inside the main chamber of the viscous flow reactor. The change in frequency of the quartz crystal before, during and after the precursor doses was monitored at a rate of 4 Hz. The QCM was allowed to stabilize for several hours to the designated reaction chamber temperature. The temperature stabilization is important for reducing the magnitude of temperature induced mass transients in the mass uptake data.²¹ The experiments were not conducted until the

change in frequency of the quartz crystal was $\leq \pm 0.2$ Hz/min. After stabilization, the Z-factor of the QCM was calculated to check that the change in frequency caused by the polymer thin film was within 2% of the uncoated quartz crystal frequency. Under this condition the Sauerbrey relationship is used to convert the change in frequency to a change in mass.^{22 23}

QCM analysis of TMA multidoses. The infiltration of TMA into the sub surface of PET polymer films with varied crystallinities was performed at a fixed temperature of 100°C. A fresh coated quartz crystal was used for each experiment. The pressure of the viscous flow reactor was kept constant at 1 Torr with a nitrogen gas flow rate of ~300 sccm. The infiltration of TMA into the polymer thin films via TMA multi doses was investigated using a cycle sequence of TMA/Purge/H₂O/Purge = 0.2/60/0/60 sec. The above sequence was repeated for 10 cycles which corresponded to 10 consecutive exposure cycles (i.e. multi-doses) of TMA with an eliminated water dose.

X-ray diffraction measurements of PET polymer films. The crystallinity of the PET polymer films was obtained using low angle X-ray diffraction with a Rigaku Bragg-Brentano XRD instrument. The X-ray beam was incident on the sample at a fixed glancing angle to avoid interference from the silicon substrate. The detector collected X-ray intensities by moving around the sample through 2 θ values between 12 and 45°. Crystallinity values were obtained by fitting the XRD data to an amorphous PET sample with an amorphous peak at 2 θ = 21.3°.

Meltspun PET fibers. PET fibers were melt spun using a Hills Inc. melt spinning line at NC State's College of Textiles. To prevent hydrolytic degradation of the polymer during melt spinning, the same PET pellets (Eastman) used for QCM studies were dried in air at 120°C

for 4hrs to remove pre-absorbed water. The PET polymer was melted in a hopper and fed through a single screw extruder to a 69 hole count spinneret. The emerging polymer melt was passed through a quench zone and carefully collected on a bob pin at a take up speed of 500 m/min. Finally, the PET bundle was wound onto a draw roller followed by a storage roller that winds the bundles onto a cardboard package. To increase the crystallinity and orientation of PET fibers, different specimens were wound onto the draw roller at higher velocities ranging from 1000 mpm to 1600 mpm. This draws the fiber which orients adjacent polymer chains within the fiber and promotes crystallization. The difference in velocity between the take up roller and draw roller is called the draw ratio. A draw ratio of 1:2 is achieved for example, by rotating the take up roller at 500 mpm and the draw roller at 1000 mpm. The pump speed of the extruder was varied accordingly to maintain a constant denier of 2 denier per filament.

DSC measurements of PET fibers. Glass transition temperatures and heats of fusion of the PET fiber specimens were measured with a Perkin-Elmer differential scanning calorimeter (DSC). The weight of each specimen used in the analysis was approx. 3-5mg. Each thermogram was obtained from the temperature range 25 to 280°C at a heating rate of 20 °C/min. The heat of fusion for 100% crystalline PET was taken from the literature to be 140.1 J/g. The crystallinity of each sample was calculated using the following relationship: $(\Delta H_{\text{Melt}} - \Delta H_{\text{Cry}} / \Delta H_{\text{Melt}}) \times 100$.

SVI modification of PET meltspun fibers. Meltspun PET fiber specimens with varied crystallinities were sequentially washed in methanol and de-ionized water to remove surface impurities and lubricants applied to the fibers during the melt spinning process. After

cleaning, the PET fibers were dried in air for 12 hours at 50°C. After drying, the specimens were loosely wrapped around and secured to a porous aluminum cyclinder. A detailed description of the SVI process is provided elsewhere.¹⁶ The cyclinder was placed inside a viscous flow reactor at a temperature of 50°C and a pressure of 1 Torr using a nitrogen gas flow rate of 300 sccm. Experiments were conducted at 50°C to prevent the fibers from shrinking at temperatures above the glass transition temperature of the polymer fibers (approx. 80°C). Prior to SVI exposure cycles, the reaction chamber was purged for 600 seconds to provide an inert environment to prevent unwanted reactions with the fiber specimens. The fibers were modified via SVI using a TMA half exposure sequence of TMA/Hold/Purge = 0.5/30/30 seconds. After the TMA half exposure cycle, the process was completed with the second half exposure of water using a sequence of H₂O/Hold/Purge = 0.2/30/30 seconds. The effect of TMA exposure on the mechanical properties of PET fibers with varied crystallinities, was investigated with 30, 50 and 100 cycles of the TMA half exposure sequence.

Tensile testing of PET fibers. An instron tensile tester with a 250lb load cell was used for investigating the mechanical properties of modified and unmodified PET bundles with 1” gauge lengths. Fiber specimens were mounted to a cardboard support with a 1” notch and secured using a suitable adhesive. Before testing, the fibers were equilibrated to the laboratory conditions of 21.1°C and 65% RH for 24 hrs. The cardboard support was placed within the grips of the tensile tester and fixed firmly with a grip pressure of 70 psi. The notch of the cardboard support was cut to free the fiber specimen. Each specimen was tested with a

constant rate of elongation (CRE) of 15mm/min. Each sample was tested 10 times using different fiber specimens.

5.3. Results and Discussion

Crystallinity of annealed PET polymer films. As shown in Table 5.1, polymer film specimens on Si wafers were annealed at different temperatures to vary crystallinity. The control specimen was an as spun PET polymer film on a Si wafer support and annealed for one minute at 100°C to remove residual solvent. The 150SQ and 200SQ samples were also annealed for one minute at 100°C to remove residual solvent after the spin coating process however; these films were subjected to additional heat treatments to change their crystallinity. The 150SQ and 200SQ samples were annealed at 150°C and 200°C, respectively for 30 minutes and slow quenched to room temperature. The annealing temperatures were above the glass transition temperature of PET (60-80°C)²⁰ to promote the mobility of polymer chains allowing them to attain their equilibrium conformation. Quenching the annealed polymer films to room temperature slowly promotes crystal growth.

Figure 5.1 shows the XRD scan of each PET polymer film annealed at different temperatures. In general, the XRD diffractogram of semi-crystalline polymers, like PET, are made up of crystalline peaks superimposed on a broad amorphous halo. For the control sample and specimen annealed at 150°C, Figure 5.1 shows the formation of crystalline peaks characteristic of the crystallographic planes (010), (1 $\bar{1}$ 0), and (100) for scattering angles $2\theta = 17.5, 22.5$ and 25.5° , respectively.²⁴ The weak intensity of the peaks and broad widths

suggest that the diffractogram is dominated by the amorphous halo and the crystal sizes are relatively small. In comparison, the intensity of the (010) peak significantly increases as the PET film is annealed at 200°C and the formation of an additional peak at $2\theta = 16.0$ is clearly observed. This is attributed to the crystalline reflection of the $(0\bar{1}0)$ plane. The narrow peak widths of the (010) and $(0\bar{1}0)$ planes for the 200°C specimen suggests that the crystal size is larger compared with the other samples. In general, preferential orientation and uniform distribution of crystals in the (010) plane is observed in the specimen annealed at 200°C while random distribution of crystals in additional planes is observed in the other specimens. As shown in Table 5.1, the % crystallinity of the samples increases as annealing temperature increases. Higher annealing temperatures promote the mobility of polymer chains allowing them to attain their equilibrium conformation. Once in their equilibrium conformation, the polymer chains pack together into a crystal lattice. The polymer chains are arranged parallel to each other in the crystal lattice with a high degree of orientation. The longer time required to quench to room temperature from 200°C promotes the growth of crystals in the form of three dimensional structures called spherulites resulting in higher % crystallinity and larger crystals.

Effect of crystallinity on precursor infiltration. Figure 5.2 shows the corresponding mass uptake behavior of TMA in PET polymer films with different crystallinities. *In-situ* QCM was used to monitor the mass uptake of 10 consecutive multidoses of TMA in PET at 100°C using an ALD cycle sequence with an eliminated water dose. Figure 5.2 shows that as crystallinity increases, the total mass uptake of TMA after 10 consecutive doses decreases

from 3750 ng/cm² for the control as spun specimen to approx. 1000 ng/cm² for the PET polymer film with the highest crystallinity. The reduction in TMA mass uptake is attributed to the effect of crystallinity on the diffusion and reaction of precursor within the polymer film.

Typically, crystalline regions prevent the high mass transfer of solute molecules through polymers since the chains are densely packed into a crystal lattice and lack segmental chain motion. It is much harder to separate the polymer chains in a crystal and the lamellae structure lacks critical free-volume voids large enough to accommodate diffusing molecules. Therefore, when a solute molecule reaches a crystalline boundary, it is forced to diffuse around the crystal as shown in Figure 5.3. Hence, the diffusion coefficient becomes a function of direction (*i.e a tortuous path through the polymer*) which means that the measured diffusion coefficient within the polymer film is averaged over the diffusion coefficients in the x, y and z principal directions. In contrast, the enhanced free volume and network of interconnect free volume voids within the amorphous region of a polymer promotes diffusion through the polymer. Therefore, we propose that the reduced mass uptake of TMA in the more crystalline polymer film is in part caused by a slower diffusion coefficient resulting in a reduction of absorbed TMA in comparison to the more amorphous control sample. In addition, we speculate that the mass uptake of TMA may also be a function of crystallinity as the TMA molecules primarily react with accessible functional groups within the amorphous region of the polymer as demonstrated in Figure 5.3. Therefore, the reduced mass uptake of TMA in the more crystalline samples is further attributed to the higher crystalline content. As crystallinity increases, the amount of amorphous regions within

the polymer decreases which consequently reduces the number of accessible reactive functional groups within the polymer resulting in a lower mass uptake of TMA.

Crystallinity of PET fibers produced with different draw ratios. Table 5.2 summarizes the specimens used for investigations of the mechanical properties of SVI modified PET fibers with different crystallinities. The crystallinity of the PET fibers was achieved by increasing the draw speed relative to the take up speed of the fibers during the melt spinning process. The drawing of the fibers causes the polymer chains to align inducing crystallization and increasing the orientation of the fiber. As shown in Table 5.2, the samples are labeled 1:1, 1:2 and 1:4 in relation to the draw ratio used to increase the orientation and crystallinity of the fibers.

Figure 4 shows the thermogram of each PET fiber sample used in the investigation. A crystallization peak and melting peak is clearly observed at 130°C and 250°C, respectively. The peak height of the heat of crystallization varies significantly between each sample with a larger peak observed for the PET fiber produced with a 1:1 draw ratio and no evidence of a peak for the fiber produced with a 1:4 ratio. The heat of crystallization is negative or exothermic while crystals form and the polymer structure assumes a lower energy state as the chains orient and pack into a crystal lattice. The heat of melting is endothermic as energy is required to break up the crystalline regions resulting in an unoriented polymer melt. The heat of melting and crystallization can be used to estimate the crystallinity of the PET fibers as shown in Table 2 using the following expression: $(\Delta H_{\text{Melt}} - \Delta H_{\text{Cry}} / \Delta H_{\text{Melt}}) \times 100$. It is clear that as the draw ratio increases, the crystallinity of the PET fibers also increases. The low %

crystallinity of the 1:1 sample indicates that the fibers are mostly amorphous. This provides insight into the height of the heat of crystallization peaks shown in Figure 5.4. The larger heat of crystallization peak of the 1:1 sample is attributed to the mostly amorphous structure of the fibers. Therefore, as the 1:1 sample is heated through 130°C at 20°C/min, the polymer chains assume their equilibrium conformation and crystallization occurs. In comparison, the 1:4 sample has a higher % crystallinity due to the drawing process (approx.38%) therefore, as the fibers are heated through 130°C at 20°C/min, additional crystallization does not occur. The lack of a heat of crystallization peak for the 1:4 fibers suggests that the crystallinity of the fibers has already reached an upper limit. This is typical of semi-crystalline polymers since molecular weight and polymer chain entanglements prevent segmental motion of the polymer chains limiting their re-orientation and packing into a crystal lattice. Therefore, it is uncommon for certain semi-crystalline polymers to attain 100% crystalline structures even if given sufficient time.

Mechanical properties of PET fibers. During tensile testing, the 250lb load cell applied a force to the fiber specimens causing an elongation at a constant cross-head speed of 15mm/min at 21°C and 65% RH. As the load cell applies force to the fibers causing an extension, the amorphous chains uncoil and begin to elongate. At the yield point, which is determined by the point at which the initial slope of the curve meets the slope of the plastic region, the fibers undergo plastic deformation. As the fiber is forced in the plastic region, crystalline domains begin to tilt in the direction of extension. As the load cell continues to increase the force on the fiber, the amorphous chains extend and adjacent crystalline and amorphous regions begin to align, this is called cold drawing. The amorphous chains

experience some permanent deformation however, if the load is released within the plastic region, the amorphous chains are able to elastically recover some of the strain. Eventually, the load imposed on the fiber is sufficient to cause permanent deformation on the fiber. At this point, the amorphous chains are fully extended and unable to elastically recover resulting in the strain hardening of the material. Finally, the force causes crystalline segments to break up into smaller domains and the fiber fails when the amorphous chains between crystals begin to break as they are unable to support the increasing load.

Figure 5.5 shows the peak load-elongation curve of the control specimens (*i.e. unmodified specimens*) for the 1:1, 1:2 and 1:4 PET fiber samples. One can see that there is a compromise between high strength with low elongation at break and large elongation at break with low strength as shown for the 1:4 and 1:1 PET fiber samples, respectively. The 1:4 PET fiber sample with the higher % crystallinity possesses a greater peak load of approx. 275 gf at an elongation of 6mm while the more amorphous 1:1 PET fibers possess a greater elongation at break of 58mm with a peak load of 48 gf. The 1:2 PET fiber sample falls between the former samples with a peak load of approx. 230 gf at an elongation of 18mm. The higher strength of the 1:2 and 1:4 samples is attributed to their higher crystallinity in comparison to the 1:1 sample because more force is required to break up the crystalline regions and the amorphous chains are more aligned. In comparison to the 1:2 sample, the polymer chains in the amorphous region are unfolded and extended due to the larger draw ratio. Therefore, the properties become highly anisotropic in the direction of extension and the fibers behave more elastically under force resulting in higher strength but lower elongation at break than the 1:2 fiber samples. The polymer chains in the more amorphous

1:1 PET fibers are randomly coiled and entangled therefore, under force the randomly coiled chains are able to unfold, disentangle and glide past each other. This results in a larger elongation at break with lower strength as the load is dissipated by polymer chain disentanglements and viscous flow of adjacent chains. With an original gauge length of 25.4mm the strain to failure of the 1:1, 1:2 and 1:4 fibers are 228% 71% and 23%, respectively. Each sample shows evidence of a yield point therefore, the 1:2 and 1:4 fiber samples can be characterized by plastic deformation with the 1:4 fiber being closer to a brittle transition while the 1:1 sample is more ductile as the polymer chains unfold and flow under force.

Mechanical properties of SVI modified PET fibers. Previous research has shown that the exposure of certain polymers to organometallic precursors forms hybrid organic-inorganic interfaces as the precursor molecules diffuse into the sub-surface of the polymer. It has also been shown that precursors such as TMA can diffuse into the bulk of PET polymer fibers. The SVI technique exploits the diffusion of organometallic precursors into polymers by introducing a hold step that soaks the polymer and promotes infiltration. Studies indicate that infiltrated TMA in PET reacts with carbonyl functional groups along the backbone of the polymer resulting in R-O-Al-O complexes with the potential of forming R-O-Al-O-R intra-chain complexes. The formation of an intra-chain complex within the bulk of polymer fibers is of particular interest for the effect that the structure has on the mechanical properties of the polymer.

Figure 5.6 shows the peak load-elongation curve of PET fibers modified by sequential infiltrations of TMA at 50°C. The mechanical properties of modified and control fibers are compared to elucidate the process-structure-property relationships of the PET fibers. The effect of TMA infiltrations on the mechanical properties of the PET fiber samples was investigated by varying the number of TMA half exposure cycles from 30 to 100. For the 1:1 PET fiber sample, there is a significant decrease in the elongation at break as the number of TMA cycles increases. Despite the reduction in elongation, there is a slight increase in peak load for 30 TMA infiltrations however, the peak load decreases as the number of TMA cycles increase to 50 and 100. As the number of TMA cycles increases in the 1:2 control sample, both peak load and elongation at break decrease dramatically. In comparison, it is interesting to observe that both the peak load and elongation of the 1:4 sample increases with 30 and 50 cycles of TMA. Specifically, there is an 18 % increase in peak load (325 gf) and 7 % increase in peak load (298 gf) for 30 TMA and 50 TMA cycles, respectively. For 30 TMA cycles the elongation at break increases by 150 % from 6 mm to 15 mm while the elongation at break increases by approx 50% from 6mm to 9mm for 50 cycles of TMA. Finally, the strength and elongation of the 1:4 PET fibers drastically reduces with 100 TM cycles.

Both an increase in strength and elongation is typically not observed in synthetic polymer fibers. In general, the observations shown in Figure 5.5 are characteristic of their intrinsic mechanical properties which are either: (i) high strength-low elongation, (ii) high elongation-low strength. An increase in both strength and elongation has only been observed inherently in biological fibers such as spider silk. In general, semi-crystalline polymers such as PET are represented by two phase models consisting of an amorphous region of randomly

coiled polymer chains and a crystalline region made up of densely packed folded chains. When synthetic polymers are drawn during the meltspinning process the amorphous chains uncoil and extend causing orientation in the direction of drawing. However, amorphous polymer chains are not all the same length and extend at different rates therefore, oriented amorphous chains form as shown in Figure 5.7. These chains act as defect sites within the polymer fiber since they are more likely to fail under the applied force prior to the unfolding of adjacent coiled chains. Herein, we propose that the infiltration of TMA into the bulk of the PET fibers forms intra-chain R-O-Al-O-R complexes that act as a mechanical buffer within the amorphous region of the fiber by preserving the structure and reinforcing the orientated amorphous chains as shown in Figure 5.7. Therefore, the increased strength of the 1:4 fiber specimen with 30 TMA cycles is attributed to the reinforcement of the oriented amorphous chains which resist failure under force allowing the fiber to extend to a greater elongation prior to failure. Figure 5.6 clearly indicates the balance between the number of TMA cycles and the crystallinity of the PET fibers. In general, as the number of TMA cycles increases, the strength and elongation of the fibers decreases. We attribute this to an increase in density of the mechanical buffer as more TMA infiltrates and reacts with functional groups within the amorphous region of the fibers. This causes a transition to more brittle fibers resulting in reduced strength and elongation at break. The effect of increasing TMA cycles is more dramatic as the crystallinity of the fibers decreases. This observation is supported by the in-situ QCM analysis of TMA exposure to PET films with varied crystallinities. It is clear from Figure 5.2 that more TMA infiltrates the less crystalline specimens. This supports the fact that the mechanical buffer within the amorphous 1:1 fiber and moderately crystalline 1:2

fiber is denser in comparison to the more crystalline 1:4 fiber. Although there is a slight increase in strength of the 1:1 fiber infiltrated with 30 cycles of TMA due the formation of R-O-Al-O-R complexes that hold the structure, the elongation at break is still reduced. This is due to the restriction of the mechanical buffer on the contraction and flow of polymer chains at the yield point resulting in more brittle fibers.

5.4. Conclusion

This work explores the infiltration of organometallic precursors into PET polymer films and fibers and explores the resulting structure-process-property relationships. In-situ quartz crystal microgravimetry was employed to investigate the infiltration of TMA into PET polymer films. Specifically, the effect of crystallinity on the infiltration of TMA in PET with varied crystallinities was explored. The crystallinity of the polymer films was varied by increasing the annealing temperature above the glass transition temperature of PET for 30 minutes relative to a control sample annealed at 100°C for 1 min. XRD shows that the control sample had the lowest crystallinity which increased for samples annealed at higher temperatures. In-situ QCM analysis demonstrates that there is lower mass uptake of TMA in the more crystalline films compared to the amorphous control sample. This was attributed to a reduction in the diffusion coefficient due to the tortuous path created by crystal boundaries and the crystalline content reducing the number of available reactive sites within the polymer film. Finally, the effect of exposure to TMA/H₂O SVI on the mechanical behavior of PET fibers produced by meltspinning was explored. Three fiber samples were explored in the study, each possessing a different % crystallinity resulting in varied tensile behaviors. With

infiltrations of TMA, the tensile results indicate that the peak load and elongation of the PET fibers increase with exposure to TMA. However, the increase in strength and elongation is dependent on the intrinsic crystallinity of the fiber and the number of TMA infiltrations. This work has exciting implications for low basis weight, high impact materials as well as the introduction of inorganic material properties to flexible polymer systems.

Chapter 5 Figures:

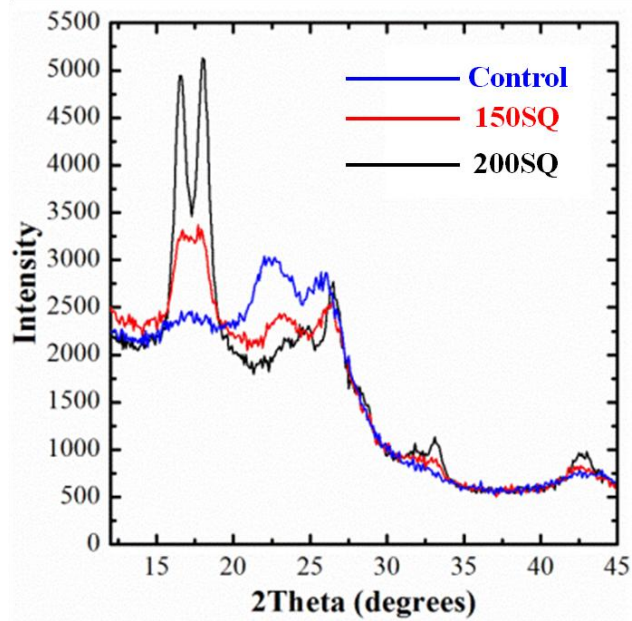


Figure 5.1. XRD Diffractogram of PET specimens annealed under different heating conditions to vary crystallinity. The diffractogram shows the formation of crystalline peaks characteristic of the crystallographic planes (010), ($1\bar{1}0$), and (100) for scattering angles $2\theta = 17.5, 22.5$ and 25.5° , respectively.²⁴

Table 5.1. Summary of PET specimens used in this study. Each film was heat treated under different conditions to vary % crystallinity.

PET Film	Heat Treatment	% Crystallinity (XRD)
Control	100 °C / 1 min	10
150SQ	150 °C / 30 min	48
200SQ	200 °C / 30 min	63

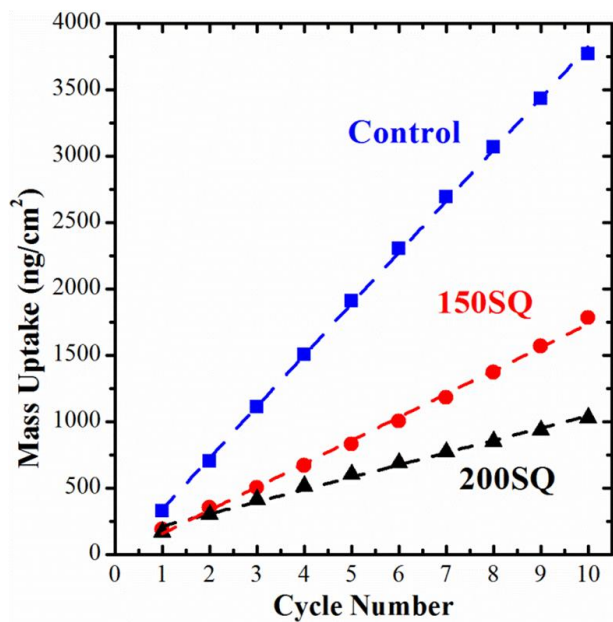


Figure 5.2. Mass uptake behavior of TMA in PET polymer films with different crystallinities. *In-situ* QCM was used to monitor the mass uptake of 10 consecutive multidoses of TMA in PET at 100°C using an ALD cycle sequence with an eliminated water dose.

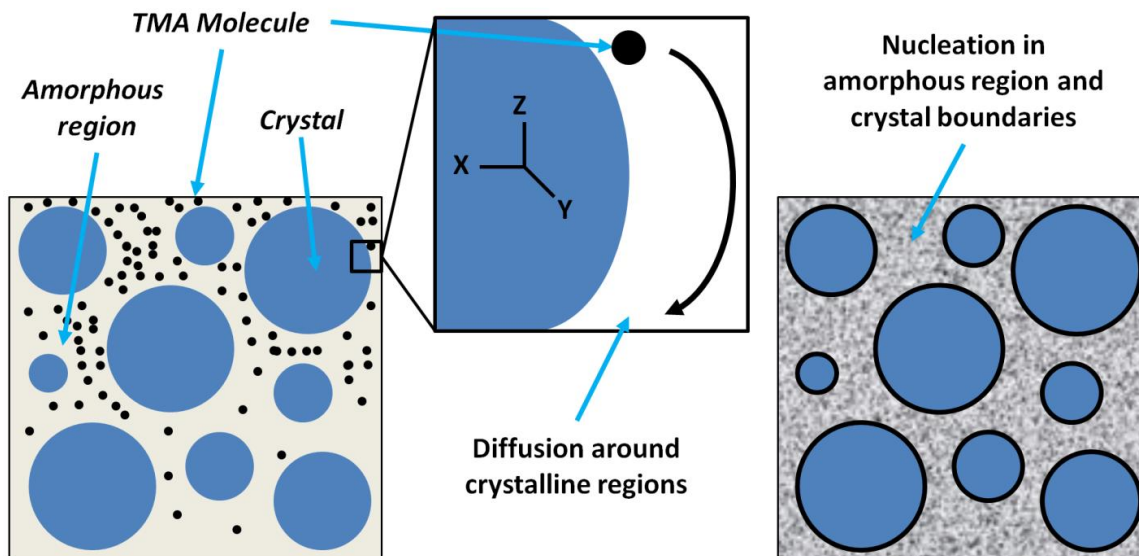


Figure 5.3. Diagrammatic representation of the effect of crystallites on the diffusion of precursor vapor and the corresponding mass uptake as measured by in-situ QCM analysis.

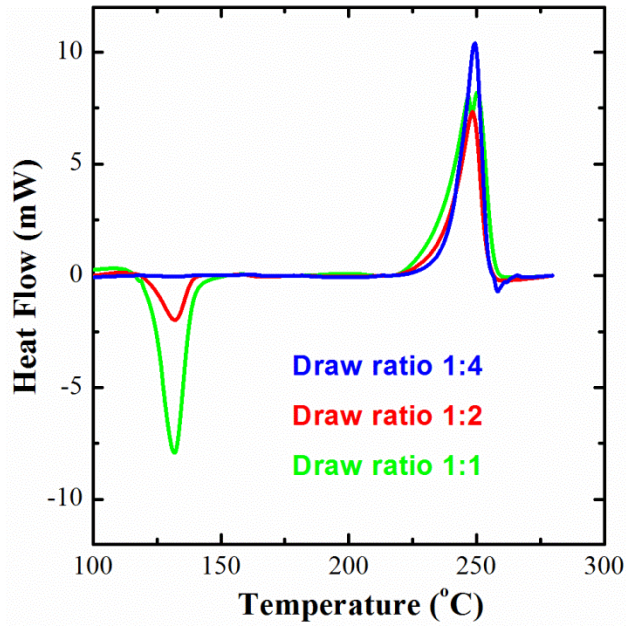


Figure 5.4. DSC thermogram of PET fiber specimens explored in this study. The thermograms were obtained using a heat rate of 20°C/min.

Table 5.2. Fiber specimens used for investigations of the mechanical properties of SVI modified PET fibers with different crystallinities.

PET Fiber Sample	Take-up Speed/Draw Speed (m/min)	ΔH Crystallization (J/g)	ΔH Melt (J/g)	% Crystallinity (DSC)
1:1	500-500	25.6	39.9	10
1:2	500-1000	7.01	40.7	24
1:4	400-1600	N/A	53.1	38

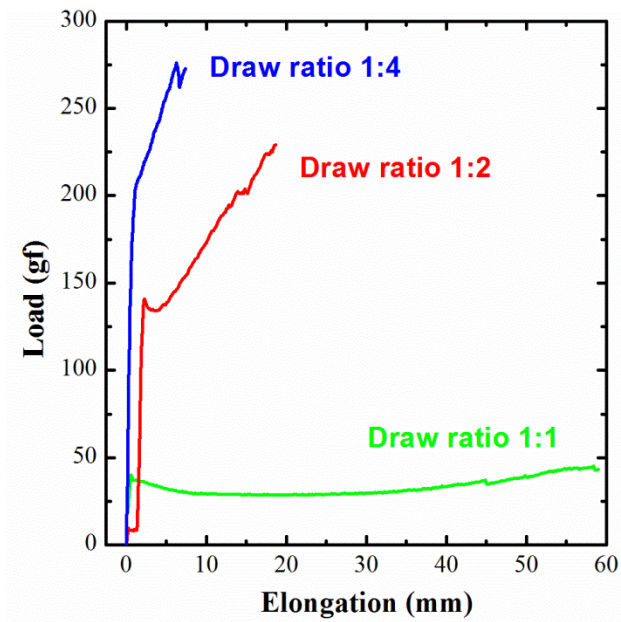


Figure 5.5. Peak load-elongation curve of the control specimens (*i.e. unmodified specimens*) for the 1:1, 1:2 and 1:4 PET fiber samples. The data was obtained using a 250lb load cell and a crosshead speed of 15 mm/min in a conditioned laboratory at 21°C and 65% RH.

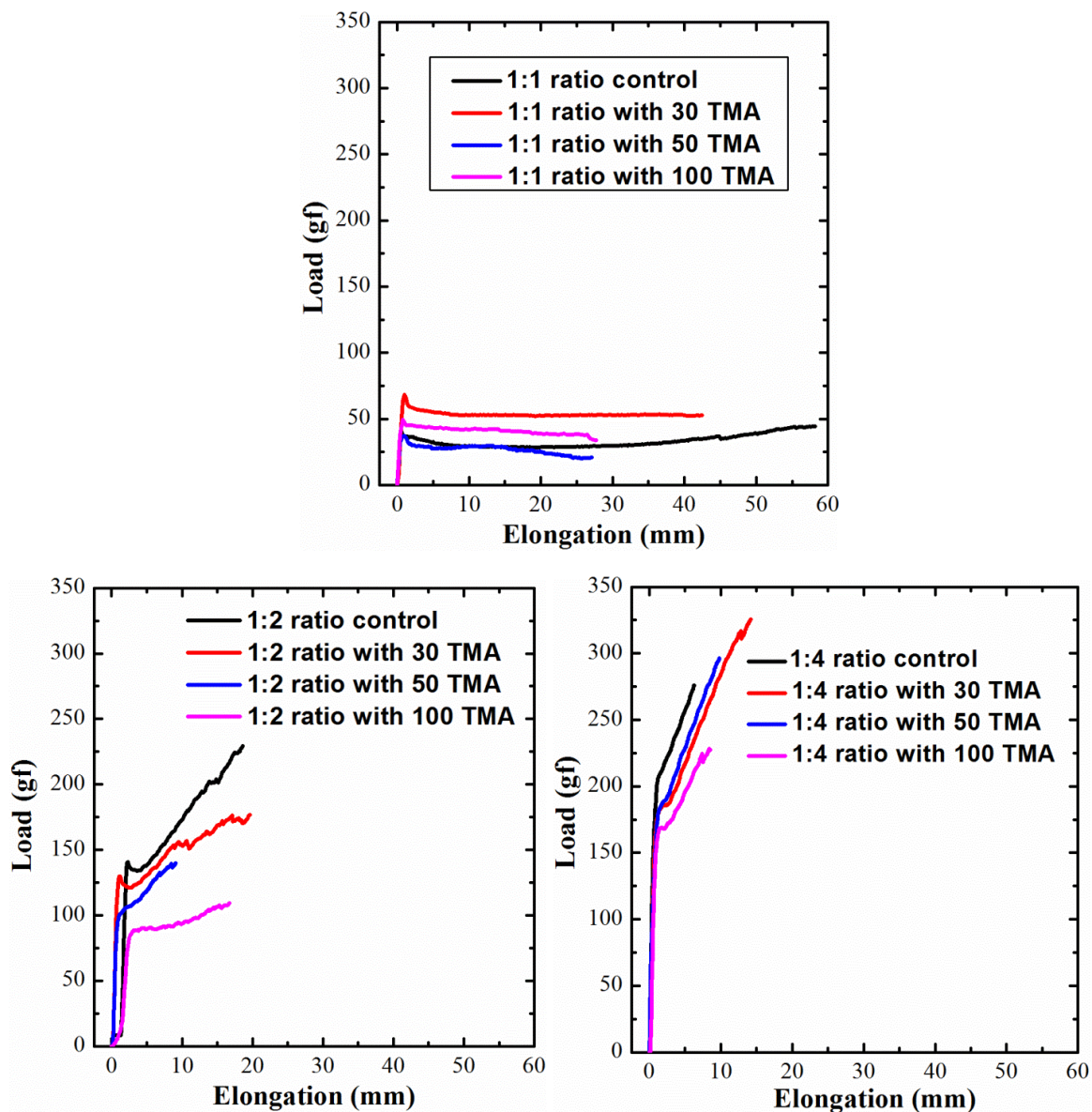


Figure 5.6. Peak load-elongation curve of PET fibers modified by sequential infiltrations of TMA at 50°C. The mechanical properties of modified and control fibers are compared to elucidate the process-structure-property relationships of the PET fibers. The data was obtained using a 250lb load cell and a crosshead speed of 15mm/min.

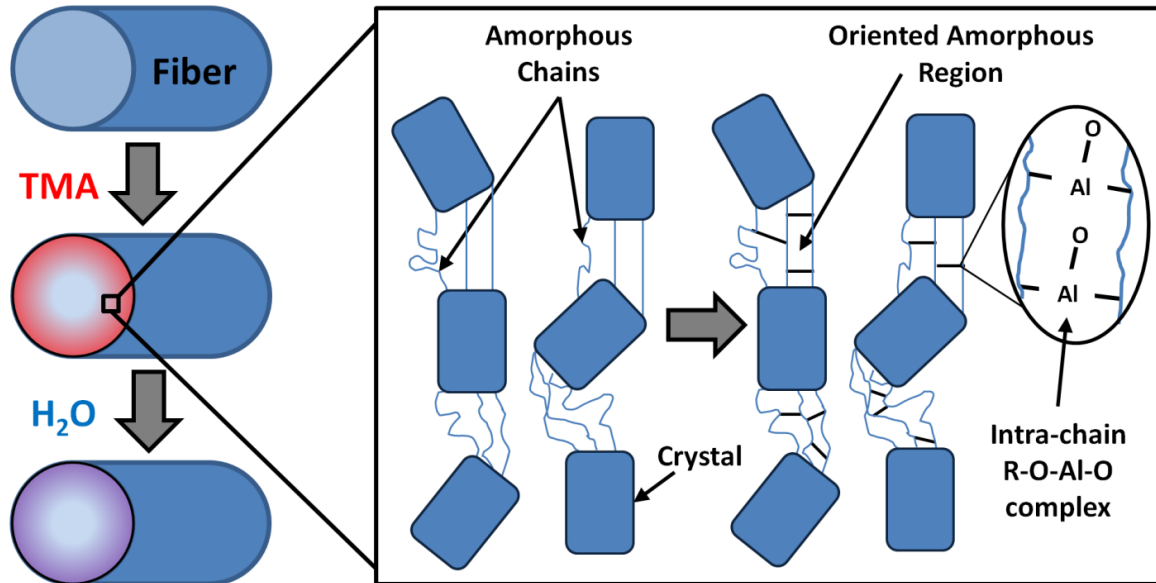


Figure 5.7. Diagrammatic representation of the infiltration of TMA into the bulk of the PET fibers forming intra-chain R-O-Al-O-R complexes. These act as a mechanical buffer within the amorphous region of the fiber by preserving the structure and reinforcing the orientated amorphous chains.

Chapter 6 References:

1. Kickelbick, G., Hybrid materials : synthesis, characterization, and applications. Wiley: 2007.
2. Pedro Gómez-Romero, C. S., *Functional Hybrid Materials*. Weinheim : Wiley-VCH,: 2004.
3. Judeinstein, P.; Sanchez, C., Hybrid organic-inorganic materials: A land of multi-disciplinarity. *Journal of Materials Chemistry* 1996, 6 (4), 511-525.
4. Bang, G.; Kim, S. W., Biodegradable poly(lactic acid)-based hybrid coating materials for food packaging films with gas barrier properties. *Journal of Industrial and Engineering Chemistry* 2012, 18 (3), 1063-1068.
5. Ishchuk, S.; Taffa, D. H.; Hazut, O.; Kaynan, N.; Yerushalmi, R., Transformation of Organic-Inorganic Hybrid Films Obtained by Molecular Layer Deposition to Photocatalytic Layers with Enhanced Activity. *Acs Nano* 2012, 6 (8), 7263-7269.
6. Jena, K. K.; Rout, T. K.; Narayan, R.; Raju, K., Novel organic-inorganic hybrid coatings prepared by the sol-gel process: corrosion and mechanical properties. *Polymer International* 2012, 61 (7), 1101-1106.
7. Xu, Y. X.; Wen, Y. Q.; Wu, Y. N.; Lin, C. X.; Li, G. T., Hybrid nanofibrous mats with remarkable solvent and temperature resistance produced by electrospinning technique. *Materials Letters* 2012, 78, 139-142.
8. Yu, Q. J.; Xu, J. M.; Liu, J.; Li, B. X.; Liu, Y. J.; Han, Y. Y., Synthesis and properties of PANI/SiO₂ organic-inorganic hybrid films. *Applied Surface Science* 2012, 263, 532-535.
9. Parsons, G. N.; George, S. M.; Knez, M., Progress and future directions for atomic layer deposition and ALD-based chemistry. *Mrs Bulletin* 2011, 36 (11), 865-871.
10. George, S. M.; Lee, B. H.; Yoon, B.; Abdulagatov, A. I.; Hall, R. A., Metalcones: Hybrid Organic-Inorganic Films Fabricated Using Atomic and Molecular Layer Deposition Techniques. *Journal of Nanoscience and Nanotechnology* 2011, 11 (9), 7948-7955.
11. Sun, Y. J.; Padbury, R. P.; Akyildiz, H. I.; Goertz, M. P.; Palmer, J. A.; Jur, J. S., Influence of Subsurface Hybrid Material Growth on the Mechanical Properties of Atomic Layer Deposited Thin Films on Polymers. *Chemical Vapor Deposition* 2013, 19 (4-6), 134-141.

12. Gong, B.; Parsons, G. N., Quantitative in situ infrared analysis of reactions between trimethylaluminum and polymers during Al₂O₃ atomic layer deposition. *Journal of Materials Chemistry* 2012, 22 (31), 15672-15682.
13. Spagnola, J. C.; Gong, B.; Arvidson, S. A.; Jur, J. S.; Khan, S. A.; Parsons, G. N., Surface and sub-surface reactions during low temperature aluminium oxide atomic layer deposition on fiber-forming polymers. *Journal of Materials Chemistry* 2010, 20 (20), 4213-4222.
14. Jur, J. S.; Spagnola, J. C.; Lee, K.; Gong, B.; Peng, Q.; Parsons, G. N., Temperature-Dependent Subsurface Growth during Atomic Layer Deposition on Polypropylene and Cellulose Fibers. *Langmuir* 2010, 26 (11), 8239-8244.
15. Gong, B.; Peng, Q.; Jur, J. S.; Devine, C. K.; Lee, K.; Parsons, G. N., Sequential Vapor Infiltration of Metal Oxides into Sacrificial Polyester Fibers: Shape Replication and Controlled Porosity of Microporous/Mesoporous Oxide Monoliths. *Chemistry of Materials* 2011, 23 (15), 3476-3485.
16. Akyildiz, H. I.; Padbury, R. P.; Parsons, G. N.; Jur, J. S., Temperature and Exposure Dependence of Hybrid Organic-Inorganic Layer Formation by Sequential Vapor Infiltration into Polymer Fibers. *Langmuir* 2012, 28 (44), 15697-15704.
17. Peng, Q.; Tseng, Y. C.; Darling, S. B.; Elam, J. W., A Route to Nanoscopic Materials via Sequential Infiltration Synthesis on Block Copolymer Templates. *Acs Nano* 2011, 5 (6), 4600-4606.
18. Lee, S. M.; Pippel, E.; Gosele, U.; Dresbach, C.; Qin, Y.; Chandran, C. V.; Brauniger, T.; Hause, G.; Knez, M., Greatly Increased Toughness of Infiltrated Spider Silk. *Science* 2009, 324 (5926), 488-492.
19. Lee, S. M.; Pippel, E.; Knez, M., Metal Infiltration into Biomaterials by ALD and CVD: A Comparative Study. *Chemphyschem* 2011, 12 (4), 791-798.
20. Brandrup, J.; Immergut, E. H.; Grulke, E. A.; Abe, A.; Bloch, D. R., Handbook of Polymers. John Wiley & Sons: 2005.
21. Rocklein, M. N.; George, S. M., Temperature-induced apparent mass changes observed during quartz crystal microbalance measurements of atomic layer deposition. *Analytical Chemistry* 2003, 75 (19), 4975-4982.
22. Elam, J. W.; Groner, M. D.; George, S. M., Viscous flow reactor with quartz crystal microbalance for thin film growth by atomic layer deposition. *Review of Scientific Instruments* 2002, 73 (8), 2981-2987.

23. Wilson, C. A.; Grubbs, R. K.; George, S. M., Nucleation and growth during Al₂O₃ atomic layer deposition on polymers. *Chemistry of Materials* 2005, 17 (23), 5625-5634.

24. Nunes, R. A. X.; Costa, V. C.; Calado, V. M. D.; Branco, J. R. T., Wear, Friction, and Microhardness of a Thermal Sprayed PET - Poly (Ethylene Terephthalate) Coating. *Materials Research-Ibero-American Journal of Materials* 2009, 12 (2), 121-125.

FUTURE PROSPECTS

This study investigated the effect of polymer microstructure on the nucleation behavior of alumina during a typical ALD process via exposure to a series of polyesters and poly-n-methacrylates. The data indicates that T_g , as influenced by variations in microstructure, has a significant impact on the absorption of TMA. As shown in this work, polymers that possess lower T_g 's absorb larger quantities of TMA due to a larger free volume. On the other hand, polymers with higher T_g 's absorb less TMA due to a reduced free volume. This was further demonstrated in Chapter 3 by exploring the infiltration of TMA into the sub-surface of PA-6, PAA, PET and acrylic thin films via *in-situ* QCM analysis at varying reactor temperatures. The data indicates that TMA absorption is promoted as temperature increases, which is attributed to an increase in free volume promoting the infiltration of precursor. The analysis of polymer films also shows that the mass uptake of TMA decreases at lower reactor temperatures below the T_g of the respective polymer. An explanation for this phenomenon is presented that suggests that the diffusion is inhibited below the glass transition temperature of the polymer due to the corresponding reduction in free volume. Finally, the effect of TMA infiltration on the mechanical behavior of fibrous materials was investigated in Chapter 4. In particular this work highlights the structure-process-property relationships between modified and unmodified PET fibers infiltrated with TMA. The results indicate that the peak load and elongation of the PET fibers increase with exposure to TMA. Therefore, this work has exciting implications for low basis weight, high impact materials using inexpensive, flexible polymer substrates. Furthermore, this work has important implications on the introduction of hybrid material properties to polymer films and

fibrous systems which is of increasing interest due to the ability to develop flexible materials with unique mechanical, electrical, and optical behaviors.

Future work should focus on the modification of the ALD process so that it is attuned to the influence of polymer microstructure which, in some cases, causes significant infiltration of precursor resulting in the bulk modification of the polymer properties and homogenous nucleation behavior. As shown in Chapter 2, the absorption of TMA influences the desorption time required to remove unreacted TMA from the polymer film prior to the water dose. This has a dramatic impact on the nucleation behavior of alumina using a typical ALD cycle sequences that has been optimized for ‘ideal’ ALD processing. Therefore, this work shows that the influence of polymer microstructure on the absorption and desorption characteristics of organometallic precursors must be considered and the ALD process parameters adjusted accordingly to promote the formation of desirable inorganic material interfaces.

As shown in Chapters 4 and 5, the SVI process holds promise for the modification of polymers with novel hybrid interfaces by promoting the infiltration mechanism using a simple hold step that increases precursor exposure. Future work should focus on the control over the formation of a hybrid interface using single half exposure cycles of precursor to decrease modification time and increase overall throughput. This can be aided by using the detailed understanding of the temperature dependant infiltration behavior of precursor shown in this study to develop accurate physical models that can describe the complex reaction-diffusion process.

The methodology used in this work to explore the infiltration and nucleation behavior of precursor in a series of polymers, provides an interesting opportunity to understand and predict the infiltration behavior of precursor in a broad range of polymers. Group contribution methods have been utilized in the field of polymer science to predict the behavior of polymers based on substitution effects of individual functional groups or main chain substituent's. This work clearly shows how a subtle change in polymer microstructure can significantly change the response of a polymer to an external stimulus such as temperature, which has a corresponding influence on processes such as gas permeation. The author strongly believes that the group contribution method can be applied to further understand the influence of polymer microstructure on the nucleation behavior of organometallic precursors by extending the technique to a broader range of precursors and temperature ranges. Finally, a comprehensive understanding of the reaction mechanism between organometallic precursors and polymer functional groups is still an area that requires more attention. Therefore, the group contribution method, along with residual gas analysis, may be an effective way to pin-point the precise reaction mechanisms by analyzing polymers that have functional groups with standardized reactivities as well as analyzing reaction by-products, respectively.